博士論文

Kinetic and Membrane Reactor Studies of Steam Methane Reforming on Ni-Based Catalysts

（ニッケル触媒を用いたメタン水蒸気改質の速度論解析と

膜反応器に関する研究）

Naoki Kageyama

影山　直樹

Kinetic and Membrane Reactor Studies of Steam Methane Reforming on Ni-Based Catalysts

（ニッケル触媒を用いたメタン水蒸気改質の速度論解析と膜反応器に関する研究）

The University of Tokyo, School of Engineering,
Department of Chemical System Engineering,
Ph. D thesis 2018　37-127119 Naoki Kageyama

東京大学大学院工学系研究科
化学システム工学専攻　2018年度博士論文
37-127119　影山直樹

Contents

Chapter 1. General Introduction

1.1 Background

Hydrogen is an important feedstock for the synthesis of various chemicals, the refining of petroleum and the generation of electricity. Currently, the majority of hydrogen for industrial use is produced by the reforming of fossil fuels [1], especially by the reforming reactions of methane, the principal component of natural gas [2]. Steam methane reforming (SMR), $CH_4 + H_2O \rightarrow CO + 3H_2$ is the most basic reforming reaction of methane with strong endothermicity. This reaction is generally accompanied by the moderately exothermic water-gas shift reaction, $CO + H_2O \rightarrow CO_2 + H_2$. The SMR requires considerable amounts of heat to sustain the reaction temperature (800-1000 ^oC) resulting in high energy consumption with large CO_2 emissions. There have been numerous studies seeking a more effective operation of SMR such as sorption enhanced reforming [3], chemical looping reforming [4], or membrane enhanced reforming [5], which will be discussed in Chapter 2. Recently, some studies have reported the operation of SMR at low temperatures such as 400-650 ^oC [6,7].

Hydrogen purification is also indispensable for many practical applications. For example, in the usage of hydrogen in fuel cells, slight amounts of impurities might cause unexpected reactions like catalyst poisoning or competitive adsorption leading to smaller amount of energy production and shorter lifetime of the catalyst [8]. Today, pressure swing adsorption, cryogenic distillation and membrane separation are significant hydrogen purification processes. Membrane reactors are based on the idea that in addition to the hydrogen separation process, selective extraction of specific products can shift the equilibria to the product side and enhance the reaction. The application of hydrogen permselective membranes to hydrogen generation reactions improves the hydrogen yield by the selective extraction of hydrogen. The membrane works as a reaction accelerator and a hydrogen separator and produces highly pure hydrogen with smaller process units. In practical applications, several membranes are used in parallel to increase the area of the membrane for gas permeation in the limited volume of the reactor [9] and the arrangement of those membranes is a principal factor in membrane reactor design since it affects the reactor performance significantly [10].

Membrane reactors can be applied for various reactions depending on the durability or permselectivity of the membranes. Metallic membranes, especially alloyed palladium membranes [11], show high permselectivity and are considered as one of the most attractive candidates for hydrogen separation membranes despite the rarity and cost of palladium. Ceramic membranes composed of zeolites [12] and amorphous silica [13] also show excellent permselectivity for hydrogen and are attracting much attention because of their low cost. Other materials such as polymers [14], graphine [15], metal organic frameworks such as ZIF-8 [16] are being studied and some attractive features such as hydrogen storage capacity, high specific surface area, or controllability of structure which can possibly expand the variety of applications have been revealed. However, they have also non-negligible drawbacks such as difficulty of mass production, lifetime, costs, and sensibility towards heat or chemicals and, therefore, need additional improvements before they can be applied widely.

Some of those membranes have micropores even gas molecules cannot pass through depending on their size and act like sieves. Some are able to ‘dissolve’ hydrogen like palladium [17] or amorphous silica [18]. Still others have functional units on their surface with high affinity for certain gas species such as carbon dioxide [19]. Silica membranes have advantages in the variety of different structural arrangements they possess. By changing the precursors or fabrication conditions the membrane can have functional surfaces [20], controlled pore sizes [21], or hydrothermal stability [13].

In order to maximize the benefits of the above research, understanding how methane turns to hydrogen, carbon monoxide or carbon dioxide in the reactor is valuable. There have been a number of studies about methane reforming including kinetic analysis of the catalytic reaction [22], 1-D modeling for membrane reactors [23] or autothermal reforming of methane in fluidized bed membrane reactors [24].

1.2 Contents of this Thesis

In this thesis, Chapter 1 describes the background of this thesis and introduces the following chapters. Attention is placed on membranes and the steam methane reforming reaction.

Chapter 2 covers a kinetic analysis of SMR in a packed-bed reactor at moderate conditions for the application of the membranes in membrane reactors. A simple kinetic model was employed which explained the trends in the experimental result well with such simplicity.

Chapter 3 discusses three models to express SMR in catalytic tubular plug flow reactor with varying inlet flow composition. The competitive adsorption to the catalyst surface has the critical contribution for the reaction but the adsorption of the product was not essential to explain SMR trends in the experimental data set.

Chapter 4 presents the operation and the analysis of SMR in membrane reactor with a silica-alumina composite membrane. Silica-based membranes show high hydrogen permselectivity so are promising materials for hydrogen separation due to their advantage on costs and chemical durability. The membrane reactor was analyzed by a kinetic model to see the contribution of the membrane in the reactor.

Chapter 5 describes the semi-batch operation of a membrane reactor, a novel mode of operation for such reactors. A reaction with mole increase in a reactor with throttled exit can utilize the pressure due to the stoichiometry of the reaction and use it as the driving force for the membrane separation. A semi-batch reactor, with closed exit is a limiting mode of operation. The hydrogen permeate flow and pressure drop on the shell side were measured during the operation and analyzed with a model considering diffusion from the ex-upstream side or ex-downstream side of the reactor. This information contributes to the further application of hydrogen permselective membranes.

Chapter 6 concludes the thesis. The study about amorphous silica based hydrogen permselective membranes and its application for hydrogen producing reactor system, membrane reactor and semi-batch reactor helps to respond to the growing demand for hydrogen.

Chapter 2 Simple Kinetic Analysis of the Catalytic Steam Methane Reforming on a Ni/MgO-SiO_2 Catalyst

The steam methane reforming (SMR) reaction was studied on a Ni/MgO-SiO_2 catalyst at 650°C (923 K) and 0.40 MPa in a tubular packed-bed reactor. The partial pressures of CH_4 and H_2O were varied and the data were fit to a kinetic model using integral analysis. Measurements were carried out at high space velocity (48000 h^{-1}) to avoid transport limitations, and this was verified by calculation of the Weisz-Prater criterion for mass transfer and the Mears criterion for heat transfer. A rate expression based on the simplest possible set of steps to describe the SMR reaction and the water-gas shift reaction was derived which give good fit to the data. Generally, the CH_4 conversion increased with increase of the inlet partial pressure of each reactant, but at low CH_4 partial pressure conditions (40 kPa) the conversion passed through a maximum. Calculations of coverage with the kinetic model gave good agreement between the product of the CH_4 and H_2O coverages and the conversion.

2.1 Introduction

This chapter describes an in-depth study of the kinetics of the steam methane reforming. The kinetics of a reaction provide valuable information that can be used for reaction design and scale-up of a process [25] as well as to understand deactivation [26]. It can also be used to understand the function of a catalyst so as to permit its improvement. This last is the subject of the current study, which consists of a simple analysis of reaction steps. The catalyst employed in this research is based on Ni, which is the most commonly used metal, but uses a $MgO-SiO_2$ support that has not been studied widely.

Hydrogen plays an important role in today's chemical industry, especially in the refining of petroleum and the synthesis of chemical products. Recently hydrogen has received attention as a potential energy source for fuel cells because of their high energy conversion efficiency [27]. Currently, the majority of hydrogen is produced by reforming of fossil fuels [28], especially by the steam reforming of natural gas, whose main component is methane. Steam methane reforming (SMR) is a strongly endothermic reaction (Eq. 2.1) which is generally accompanied by the moderately exothermic water-gas shift reaction (Eq. 2.2).

$$CH_4 + H_2O \rightarrow CO + 3H_2,\ \Delta H^o_{298} = +206\ \text{kJ/mol} \qquad \text{Eq. 2.1}$$

$$CO + H_2O \rightarrow CO_2 + H_2,\ \Delta H^o_{298} = -41\ \text{kJ/mol} \qquad \text{Eq. 2.2}$$

The SMR process is operated at high temperature (600-1000^{o}C) and requires considerable amounts of heat, commonly supplied by the combustion of extra methane, resulting in high energy consumption with large CO_2 emissions. The simultaneous water-gas shift reaction [29] produces additional H_2, though this reaction also produces CO_2. There have been many attempts to improve the process efficiency. In a study by Zheng et al. the heat required for the endothermic reforming was supplied using solar energy as a renewable energy source [30]. In another investigation by Hafizi et al. chemical looping was employed by cycling fine metal powders between oxidation and reduction vessels for hydrogen production from methane [31]. In addition to these attempts, efforts have been made to develop new catalysts.

In this research a series of steam methane reforming measurements were conducted varying the ratio of the inlet gas components, methane and water vapor as reactants and nitrogen as inert dilution gas at an intermediate pressure of 0.40 MPa.

2.2 Experimental

The gases used in this study were CH_4 (99% Toatsu Yamazaki Co., Ltd.), H_2 (99.99% Showa Denko Gas Products Co., Ltd.), N_2 (99.99% Toatsu Yamazaki Co., Ltd.).

A conventional Ni/MgO-SiO_2 catalyst (JGC Catalysts and Chemicals Ltd.) had a composition of 53.0-58.0 wt% NiO, 8.1-11.1 wt% MgO, 24.2-28.2 wt% SiO_2 (supplier information). The BET area was determined by N_2 adsorption at -196^{o}C (liquid nitrogen) using a volumetric apparatus (BELSORP-mini, Microtrac BEL Corp.). The H_2 chemisorption uptake was measured using a pulse flow instrument (CHEMBET-3000, Quantachrome Instruments) at 40 ^{o}C after 12 h reduction at 650 ^{o}C in 5% H_2/Ar.

Steam methane reforming was studied in a vertical concentric tubular reactor of a geometry suitable for future membrane reactors studies. The reactor consisted of an inner dense alumina tube, a quartz sleeve and an outer stainless steel shell and was heated by an external electric furnace. A quantity of 0.1 g of Ni/MgO-SiO_2 catalyst diluted with 3.9 g SiO_2 particles (Wako Pure Chemical Industries Ltd.) formed a catalyst bed of volume 3.0 cm^3. For best heat transfer, the catalyst bed was placed in the outer annular region between the quartz tube and the dense alumina tube. It was held in the middle of the reactor by extra SiO_2 particles filling the lower half of the reactor (Fig. 2.1). The outer tubular stainless steel tube covered the quartz tube for mechanical strength and rigid sealing, but an opening allowed pressure equalization between the inside and outside of the quartz sleeve. The pressure of the reactor was controlled by a backpressure regulator connected at the reactor exit and the temperature of the reactor was monitored by a thermocouple placed at the bottom of the catalyst bed. A pressure of 0.40 MPa and a temperature of 923 K was used for the measurements. The catalyst particles were sieved to 400-630 μm in diameter and the SiO_2 particles used for dilution of the catalyst to 600-850 μm.

In the upstream portion of the reactor, CH_4 and N_2 were mixed and introduced to a vaporizer heated at 473 K. Liquid water was fed using a pump (Hitachi L-7100) to the vaporizer and immediately vaporized and mixed with the N_2/CH_4 flow. The mixed gas flowed to the reactor in a heated tube to prevent condensation of water vapor in the lines. The inlet gas composition was varied systematically, keeping the same total flow rate at 270 μmol/s (400 cm^3 (NTP)/min), corresponding to a constant gas-hourly space velocity of 2000 h^{-1}. Considering the CH_4 the weight-hourly space velocity was 12000-72000 Ncm^3 $gcat^{-1}$ h^{-1}. The concentration of component in the inlet gas was varied in the range of 5-35 vol% for CH_4 and 20-70 vol% for H_2O, with N_2 as the balance. The outlet gas flow was analyzed by a gas chromatograph (GC-8A, Shimadzu Co.) equipped with a thermal conductivity detector (TCD) using a combination of Porapak-Q, Shinncarbon and Molecular sieve 5A columns. However, it was difficult to detect the precise amount of H_2O in the TCD, especially since its amount was large and because of the affinity between H_2O and the columns in the gas chromatograph. Thus, the amount of H_2O was calculated from the average of the mass-balances of hydrogen and oxygen individually.

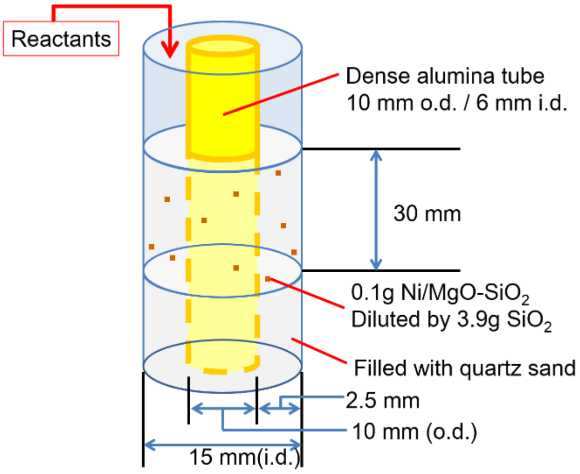

Fig. 2.1. Reactor used in the steam methane reforming studies

The kinetic data in this work was analyzed by regression with a software (μ-Kinetic Engine, μKE) developed in the Laboratory for Chemical Technology at Ghent University [32], with statistical evaluation by F-tests.

2.3 Results and Discussion

Recent developments in the area of catalytic steam methane reforming were described in a 2013 review [33]. Here, recent catalysis studies since then are summarized. Using conventional SMR reactors [34], most of the papers report Ni as the principal component but use different supports like CaO-$Ca_5Al_6O_{14}$ [35], γ-Al_2O_3[36], $K_2Ti_xO_y$-Al_2O_3[37], α-Al_2O_3[38], $NiAl_2O_4$[39], TiO_2[40], SiO_2[41], ZrO_2 [42], Al_2O_3 (Ca was co-loaded as Ca-Ni/Al_2O_3) [43], SBA-15 [44]. In addition to its activity on SMR reaction, for other reactions Ni has been reported to change the distribution of certain co-loaded metals and improve their catalytic activity [45]. The performances of those catalysts are summarized in Table 1 at reaction conditions that are similar to those used in the present investigation. As can be seen, some of the experimental results are at or close to equilibrium. The present studies are carried out away from equilibrium in order to obtain data in the kinetic regime.

Table 2.1 Summary of Recent Results in Steam Methane Reforming

Catalyst	Example	T °C	P MPa	H_2O/CH_4	WHSV $Ncm^3_{CH4}/h\ g_{cat}$	X_{CH4} %	Equil.X_{CH4} %	CO_2/CO	Stability	Ref.
$Ni/CaO-Ca_5Al_6O_{14}$	15wt% Ni	650	0.10	4	230	95	95	0.48	NR	35
$Ni/\gamma-Al_2O_3$	20wt% Ni	655	0.10	3	15000	88	98	NR	NR	36
$Ni/K_2Ti_xO_y-Al_2O_3$	11wt% Ni	700	0.10	2.5	15000	86	96	NR	>100 h	37
$Ni/\alpha-Al_2O_3$	20wt% Ni	700	0.10	3	35000	84	97	1.6	NR	38
$NiAl_2O_4$ (spinel structure)	33wt% Ni	650	0.10	3	38000	80	96	0.70	NR	39
Ni/TiO_2	10wt% Ni	500	0.10	1	6000	27	29	2.4	> 96 h	40
Ni/SiO_2	10wt% NiO	700	0.10	0.5	12000	20	83	NR	NR	41
Ni/ZrO_2	15wt% Ni	600	0.10	1	39000	20	71	1.2	4 h	42
$Ca-Ni/Al_2O_3$	64wt% NiO	600	0.10	4	NR	85	95	0.36	NR	43
Ni/SBA-15	25wt% Ni	550	0.10	2	NR	21	48	NR	NR	44
$Ni/MgO-SiO_2$	56wt% NiO	650	0.40	2	48000	40	61	2.1	> 200 h	*

NR: Not reported, *: This work

In the present work several experimental conditions were used, but repeats were made of feeds with CH_4 20%, H_2O 40%, N_2 40% and the results are reported in Table 2.1. The relationship between the conversion of methane and weight-hourly space velocity (WHSV) is plotted in Fig. 2.2 for the studies in Table 2.1. As can be seen, the data fell in two regions with downward sloping trend lines. The measurements with a ratio of H_2O/CH_4 > 2 resulted in higher CH_4 conversion and those with a ratio of

$H_2O/CH_4 < 2$ gave lower CH_4 conversion. The close agreement of the points to the trend lines is somewhat coincidental as there is some variation in temperature and H_2O/CH_4 ratio, even though the reported studies all used a pressure of 0.10 MPa. The result of this study obtained with ratio of $H_2O/CH_4 = 2$ and with a higher pressure of 0.40 MPa fell in the middle of the two curves. The filled square shows a simulated result, which will be discussed later.

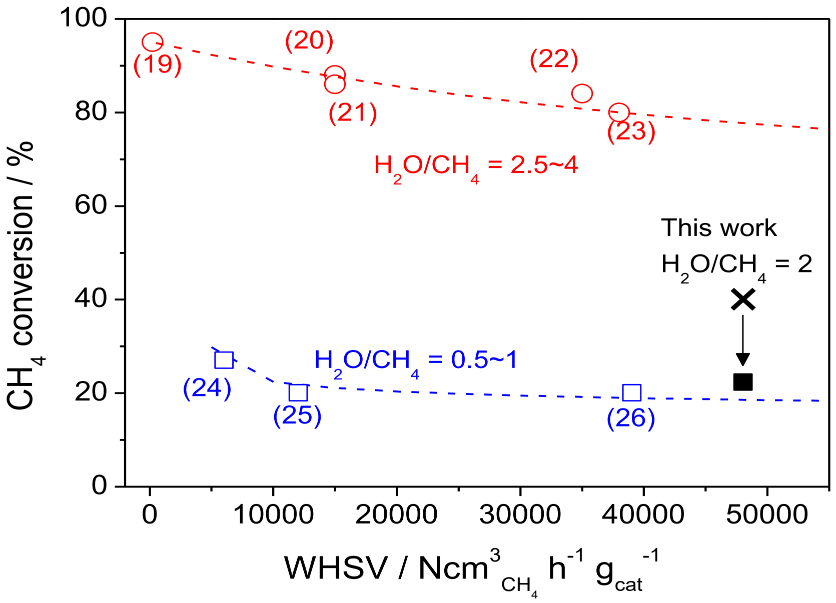

Fig.2.2. Relationship between the conversion of methane and WHSV in recent studies on steam methane reforming with Ni-based catalysts. Reference numbers are indicated by each point.
○: $H_2O/CH_4 > 2$, □: $H_2O/CH_4 < 2$, ×: This work ($H_2O/CH_4 = 2$, 0.4 MPa), ■:simulated result ($H_2O/CH_4 = 2$, 0.10 MPa)

Prior to carrying out the kinetic analysis, the Mears criterion and the Weisz-Prater criterion were calculated to verify if the reactions were mass and heat transfer limited [46]. The Mears criterion, $\left|\frac{-\Delta H r d}{hT}\cdot\frac{E}{RT}\right| < 0.15$ was calculated as 0.012 at the reaction condition which gave the highest CH_4 conversion 58% and the Weisz-Prater criterion, $\frac{-r'_{A(obs)}\,\rho_c R^2}{D_e C_{As}} < 0.3$ was calculated at the same condition as 0.032. It can be concluded that there were no internal nor external heat or mass transfer limitations in the present studies.

$$CH_4 + [\ ] \underset{k_{1-}}{\overset{k_{1+}}{\rightleftarrows}} [CH_4] \qquad \text{Reaction (1)}$$

$$H_2O + [\ ] \underset{k_{2-}}{\overset{k_{2+}}{\rightleftarrows}} [H_2O] \qquad \text{Reaction (2)}$$

$$[CH_4] + [H_2O] \xrightarrow{k_3} CO + 3H_2 + 2[\ ] \qquad \text{Reaction (3)}$$

$$CO + [H_2O] \xrightarrow{k_4} CO_2 + H_2 + [\ ] \qquad \text{Reaction (4)}$$

In this study, steam methane reforming is described with four steps which depict (1) CH_4 adsorption on the catalyst surface, (2) H_2O adsorption on the catalyst surface, (3)

CH_4 and H_2O reaction to produce CO and H_2 on the catalyst surface, and (4) CO and H_2O reaction to produce CO_2 and H_2. The quantities in brackets are adsorbed species or empty sites. In this minimal description of the reactions only the reactants CH_4 and H_2O are considered to be adsorbed, and desorption is assumed to be irreversible. It is realized that the scheme is a gross approximation, with the molecular adsorption of the species being particularly unlikely at the conditions of reaction. However, the steps are considered to simply depict the essentials of the individual process. If, for example, the adsorption of methane occurred by a more complicated sequence such as $CH_4 \rightarrow [CH_3] + [H] \rightarrow [CH_2] + 2[H] \rightarrow [CH] + 3[H] \rightarrow [C] + 4[H]$, and if the first step were slow, as it is believed to be [ ], the process would be first-order in CH_4 and each of $[CH_i]$ could be related to an adsorbed methane species through equilibrium relations.

The equilibrium coefficients for reactions Reaction (1) and (2) are defined by Eq. 2.3 and Eq. 2.4.

$$K_1 = \frac{k_{1+}}{k_{1-}} \qquad \text{Eq. 2.3}$$

$$K_2 = \frac{k_{2+}}{k_{2-}} \qquad \text{Eq. 2.4}$$

The net reaction rate of reaction (3) and (4) is calculated according to Eq. 2.9 and Eq. 2.10 respectively, with k_3 and k_4 the corresponding rate coefficients. In this hybrid scheme, CH_4 and H_2O react in the adsorbed state and, hence, the rate equations are expressed in terms of the surface concentrations of the adsorbed species.

$$r_3 = k_3 C_{[CH_4]} C^{*}_{[H_2O]} \qquad \text{Eq. 2.5}$$

$$r_4 = k_4 p_{CO} C_{[H_2O]} \qquad \text{Eq. 2.6}$$

When several active sites or surface species are involved in a reaction step, it is important to have both sites adjacent to each other for the reaction to take place [47]. This dual site character should be properly accounted for in the rate expression of the corresponding reaction step. In step (3), adsorbed CH_4 and H_2O can only react when they are adsorbed on adjacent adsorption sites. The proper driving force for step (3) is based on the adsorbed concentration of H_2O that is *adjacent* to the adsorbed CH_4, indicated as $C^*_{[H_2O]}$ in Eq. 2.5 [48]. The latter concentration is calculated as the product of the number of adjacent neighbors z and the probability of H$_2$O being adsorbed, see Eq. 2.7, with C_{tot} the total concentration of active sites. Subsequently, the probability of H$_2$O being adsorbed can be substituted by the surface coverage of H$_2$O, $\theta_{[H_2O]}$ in Eq. 2.7. The new rate expressions r_3 and r_4, shown in Eq. 2.2.8 and Eq. 2.9, are obtained by substituting Eq. 2.7 in Eq. 2.5 and rewriting the concentration of the surface species in terms of the surface coverage.

$$C^*_{[H_2O]} = z\frac{C_{[H_2O]}}{C_{tot}} = z\theta_{[H_2O]} \qquad \text{Eq. 2.7}$$

$$r_3 = k_3 z C_{[CH_4]}\theta_{[H_2O]} = k_3 z C_{tot}\theta_{[CH_4]}\theta_{[H_2O]} \qquad \text{Eq. 2.8}$$

$$r_4 = k_4 p_{CO} C_{tot}\theta_{[H_2O]} \qquad \text{Eq. 2.9}$$

When properly accounting for the dual site requirement in the rate expression of the surface reaction step, the reaction rate varies linearly with the total concentration of active sites, and not quadratically.

The final expression for the reaction rate equations is obtained by replacing the surface coverages with observable quantities, namely, the partial pressures of the components. Based on the site balance (see Eq. 2.10) and the quasi equilibrium of step Reaction (1) and (2) (see Eq. 2.11 and Eq. 2.12), the rate expressions for r_3 and r_4 are formulated in terms of the partial pressure of CH_4, H_2O and CO (see Eq. 2.13 and Eq. 2.14).

$$1 = \theta_{[\ ]} + \theta_{[CH_4]} + \theta_{[H_2O]} \qquad \text{Eq. 2.10}$$

$$\theta_{[CH_4]} = \frac{k_{1+}}{k_{1-}} p_{CH_4} \theta_{[\ ]} = K_1 p_{CH_4} \theta_{[\ ]} \qquad \text{Eq. 2.11}$$

$$\theta_{[H_2O]} = \frac{k_{2+}}{k_{2-}} p_{H_2O} \theta_{[\ ]} = K_2 p_{H_2O} \theta_{[\ ]} \qquad \text{Eq. 2.12}$$

$$r_3 = \frac{k_3 K_1 K_2 z C_{tot} p_{CH_4} p_{H_2O}}{\left(1 + K_1 p_{CH_4} + K_2 p_{H_2O}\right)^2} = \frac{k_3^{'} K_1 K_2 p_{CH_4} p_{H_2O}}{\left(1 + K_1 p_{CH_4} + K_2 p_{H_2O}\right)^2} \qquad \text{Eq. 2.13}$$

$$r_4 = \frac{k_4 K_2 C_{tot} p_{CO} p_{H_2O}}{1 + K_1 p_{CH_4} + K_2 p_{H_2O}} = \frac{k_4^{'} K_2 p_{CO} p_{H_2O}}{1 + K_1 p_{CH_4} + K_2 p_{H_2O}} \qquad \text{Eq. 2.14}$$

The reaction rates are subsequently used to determine the net rates of formation R_i for every component (Eq. 2.15 to Eq. 2.19), needed to solve the plug flow reactor equations.

$$R_{CH_4} = -r_3 \qquad \text{Eq. 2.15}$$

$$R_{H_2O} = -r_3 - r_4 \qquad \text{Eq. 2.16}$$

$$R_{CO} = r_3 - r_4 \qquad \text{Eq. 2.17}$$

$$R_{CO_2} = r_4 \qquad \text{Eq. 2.18}$$

$$R_{H_2} = 3r_3 + r_4 \qquad \text{Eq. 2.19}$$

For the optimization minimization of the sum of the square of the errors, the ordinary least squares criterion, is often employed. However, when the variance of error of the samples is not constant the contributions of samples with small errors are likely to be underestimated. In those cases, generalized least squares (GLS) minimization which minimizes the error considering the variance-covariance matrix of the samples is preferable. In practice, to obtain the variance-covariance matrix requires large numbers of experiments, then homoscedasticity is assumed for every samples. In this case the procedure is called a weighted least squares (WLS) minimization. In this study, this variance-covariance matrix is determined by µKE.

Some of the experimental conditions were repeated several times in order to verify the stability of the catalyst. In handling this repetition, the contribution of the repeated data would be larger in the weighted regression, or equivalent to the other points in the unweighted regression. In this study the experiments are discussed with unweighted and weighted regression procedures for comparison.

Evaluation of the models developed in this study employs F statistics to determine the closeness of fit between experimental and calculated results. The F test is a typically used to determine if a regression is so-called globally significant [49]. The value of F, which represents the difference in the variance between observed data and regressed data, is calculated by a prescribed equation and is compared to a tabulated F value. The latter is defined from the degrees of freedom of the dataset and the required confidence level (95% or 99% is often employed).

Fig. 2.3 shows the CH_4 conversion as a function of H_2O inlet partial pressure when the inlet partial pressure of CH_4 was 40 kPa, 80 kPa, or 120 kPa and lines obtained by the hybrid reaction model with unweighted (solid line) and weighted regression (dashed line). As expected, the conversion of CH_4 was higher when its partial pressure was lower. As also expected, the conversion of CH_4 also increased with increase of the partial pressure of H_2O, although at high H_2O inlet partial pressure the CH_4 conversion declined. This behavior can be explained by the inhibition of CH_4 adsorption on the catalyst by adsorbed H_2O.

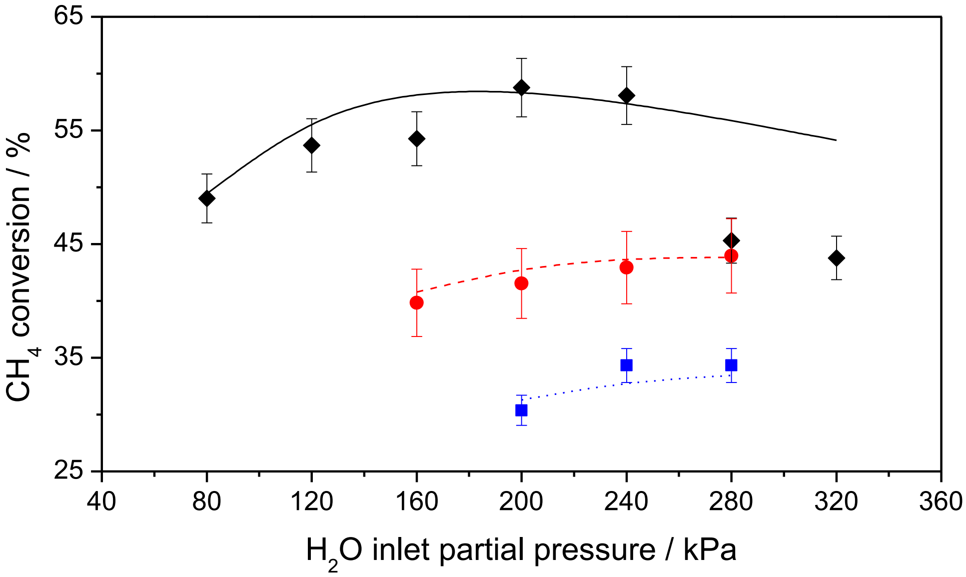

Fig. 2.3 CH_4 conversion as a function of the H_2O inlet pressure with the hybrid reaction model for reactions at a total pressure of 0.40 MPa, a temperature of 923 K, and a catalyst mass of 0.1 g. Black = 40 kPa CH_4 inlet partial pressure ($p_{CH4,in}$), red = 80 kPa $p_{CH4,in}$, blue = 120 kPa $p_{CH4,in}$.

Fig. 2.4 shows the selectivity to CO and CO_2 as a function of the inlet partial pressure of H_2O for an inlet partial pressure of CH_4 of 80 kPa. The selectivity plots were calculated from weighted and unweighted regressions and the results are also shown in Fig. 2.4. Increase in the inlet H_2O partial pressure enhanced the water-gas shift reaction (4) and increased selectivity to CO_2. It can be seen in Fig. 2.4 that the weighted regression (dashed line) give a better overall fit than the unweighted regression (solid line).

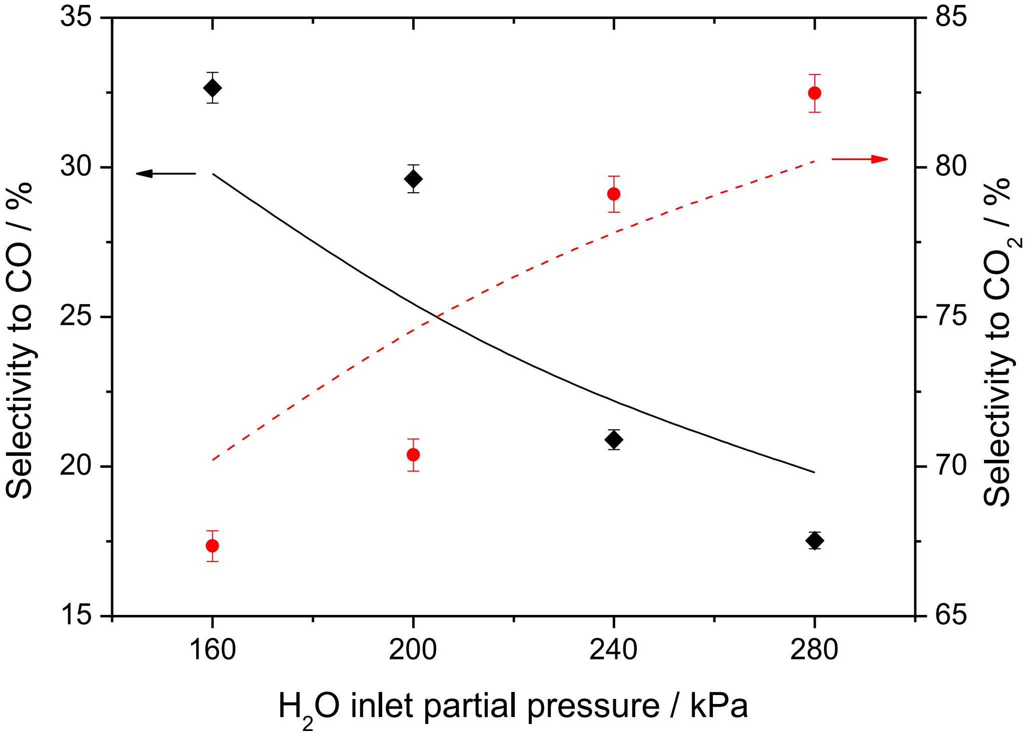

Fig. 2.4. Selectivity to CO and CO_2 as a function of the inlet partial pressure of H_2O for the hybrid scheme. Pressure 0.40 MPa, temperature 650°C, catalyst mass 0.1 g, inlet partial pressure of CH_4 80 kPa Black = selectivity to CO, red = selectivity to CO_2.

Fig. 2.5 shows the CO and CO_2 selectivity as a function of CH_4 conversion with the partial pressure of H_2O fixed at 160 kPa. Most of the data show a weak dependence of the selectivities with CH_4 conversion. There are two points that do not follow the trend lines and are considered outliers. They were obtained with a CH_4 inlet partial pressure of 20 or 40 kPa which were the lowest pressures used, so produced the lowest amounts of CO and CO_2. As mentioned in the experimental section, each gas composition was measured by TCD and the detector sensitivity for CO was the smallest. For these two points, the peak of CO was close to the detection limit hence there might be a larger error in the measurement. Therefore, these points were retained in this figure, but omitted in the regression analysis.

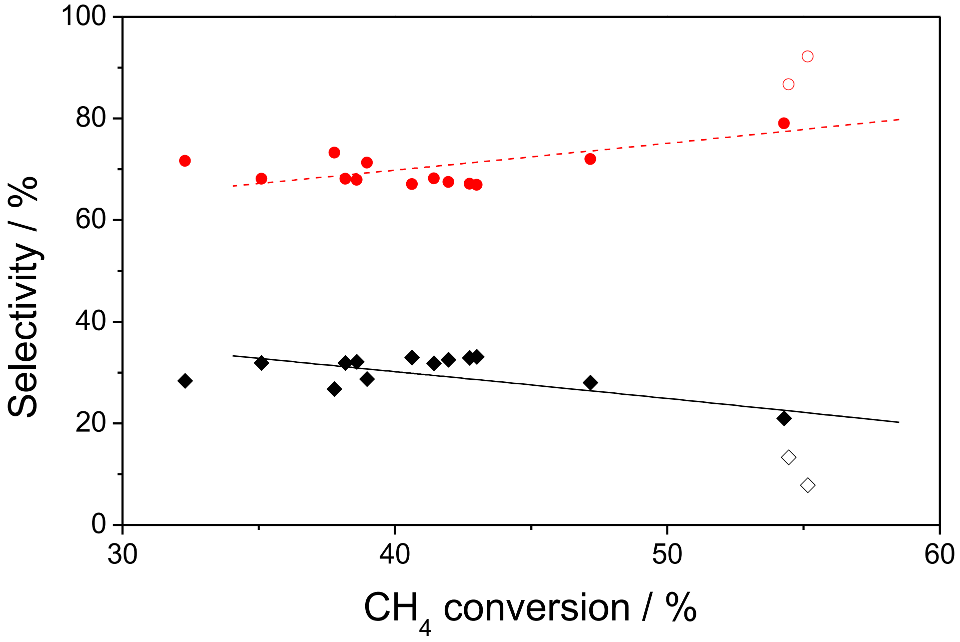

Fig. 2.5. Selectivity to CO and CO_2 as a function of the conversion for the hybrid scheme Pressure 0.40 MPa, temperature 650°C, catalyst mass 0.1 g, H_2O inlet partial pressure of 160 kPa and a CH_4 inlet partial pressure between 20 and 100 kPa. Black = selectivity to CO, red = selectivity to CO_2.

Fig. 2.6 shows a parity diagram comparing ordinal unweighted least square minimization and weighted least squares minimization. The weighted regression shows excellent agreement between calculated and measured values for CH_4, good agreement for H_2O, CO, and CO_2, and moderate agreement for H_2. It systematically ends on the low side for H_2 and slightly on the high side for H_2O, while showing scatter for CO and CO_2. The unweighted regression shows systematic deviations for all species except for H_2O. Table 2.2 shows each fitted variable; K_1 for CH_4 adsorption, K_2 for H_2O adsorption, k_3' for steam methane reforming, k_4' for the water-gas shift reaction. In Table 2.2, both k_3' and k_4' were slightly larger in the weighted regression. This accounts for the differences in the trends between the weighted and unweighted regressions.

Table 2.3 shows calculations of F statistics for model adequacy (F_a) and global significance (F_c) used to evaluate the weighted and unweighted regressions. For the results of this paper, the tabular F_a value for model adequacy is 1.54. The F_a value of the unweighted regression is 2.37 while that of the weighted regression is 1.23. Thus, only the weighted regression provides an adequate fit.

The tabular F value for global significance is 2.4. The F_s values of both the weighted and unweighted regressions greatly exceeded this value so can be deemed globally significant.

Table 2.2. Calculated model parameters of the hybrid scheme for the (un)weighted

regressions with 95 % confidence interval

	Unweighted	Weighted	Unit
K_1	3.33 ± 0.35	3.40 ± 0.06	$10^{-5} Pa^{-1}$
K_2	1.70 ± 0.18	1.72 ± 0.03	$10^{-5} Pa^{-1}$
$k_3^{'} = k_3 z C_{tot}$	2.08 ± 0.08	1.81 ± 0.02	$mol \cdot s^{-1} \cdot kg_{cat}^{-1}$
$k_4^{'} = k_4 C_{tot}$	8.46 ± 0.21	7.73 ± 0.14	$10^{-5} mol \cdot Pa^{-1} \cdot s^{-1} \cdot kg_{cat}^{-1}$

Table 2.3. Calculated F values for model adequacy (F_a) and global significance of the regression (F_s) of the hybrid scheme

	Unweighted	Weighted
F_a	2.37	1.23
F_s	2.62 10^4	2.00 10^4

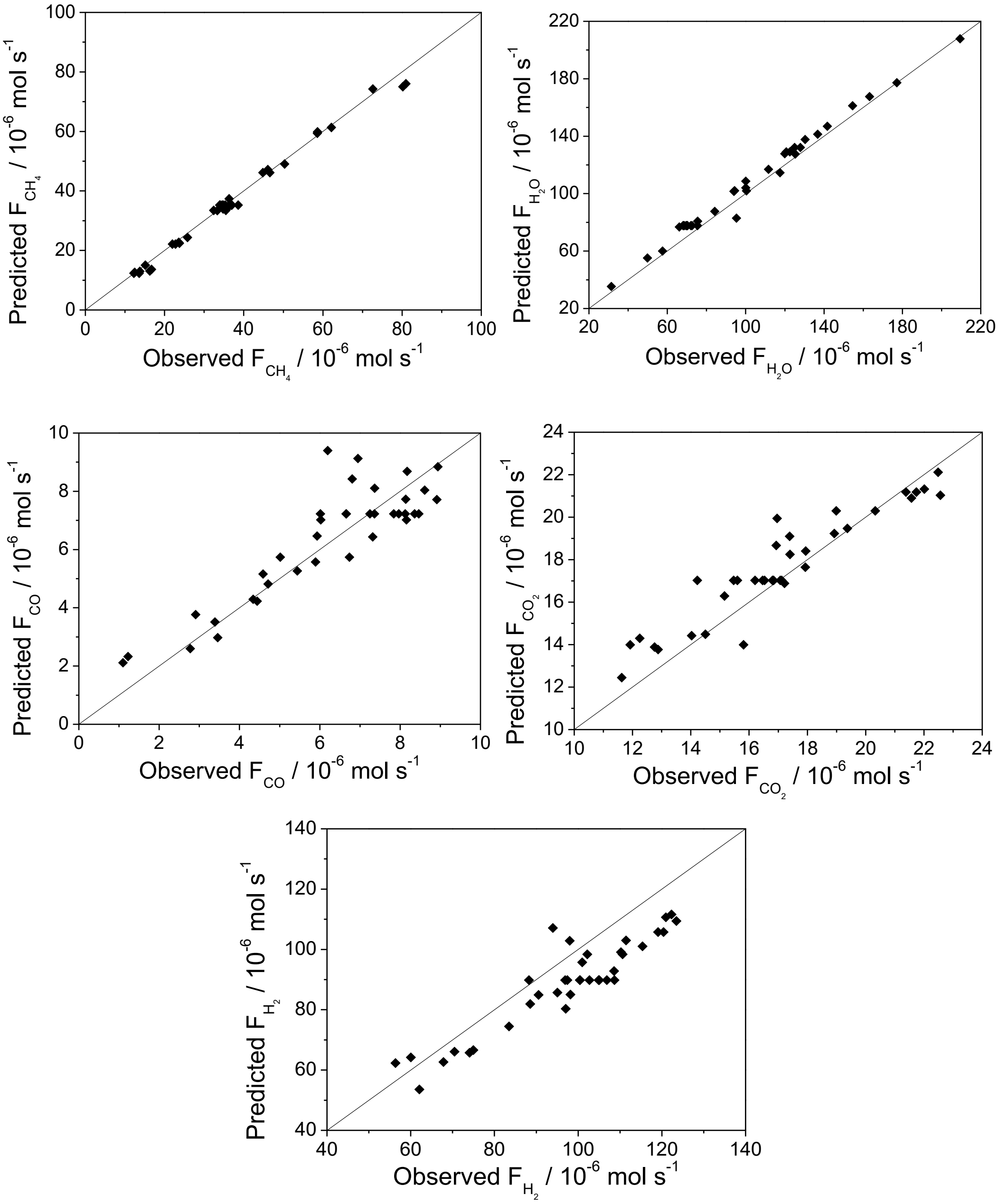

Fig. 2.6. Parity diagram of the molar outlet flow rate F_{CH4}, F_{H2O}, F_{CO}, F_{CO2} and F_{H2} for the weighted regression at a temperature of 923 K and a total pressure of 0.4 MPa. The estimated rate and equilibrium coefficients are shown in Table 2.2.

Fig. 2.7 shows the calculated coverages of the catalyst surface by CH_4 ($\theta_{[CH4]}$), H_2O ($\theta_{[H2O]}$), and empty sites ($\theta_{[\,]}$), as well as the product of $\theta_{[CH4]}$ and $\theta_{[H2O]}$ as a function of partial pressure of H_2O. These were obtained under fixed partial pressure of CH_4 at 80 kPa, and calculated from K_3 and K_4 obtained from the weighted regression (Table 2.2) and Eq. 2.10-12. With increase of the partial pressure of H_2O, the catalyst surface coverage by CH_4 decreased, as the coverage by H_2O increased. This mirrors the behavior of the conversion versus H_2O partial pressure (Fig. 2.3). Indeed Eq. 8 shows that the consumption rate of CH_4 in SMR (r_3) is proportional to the product of the coverage of CH_4 and H_2O. Therefore, both the weighted and unweighted regression follow this trend, with the unweighted regression overestimating the experimental values (Fig. 2.3).

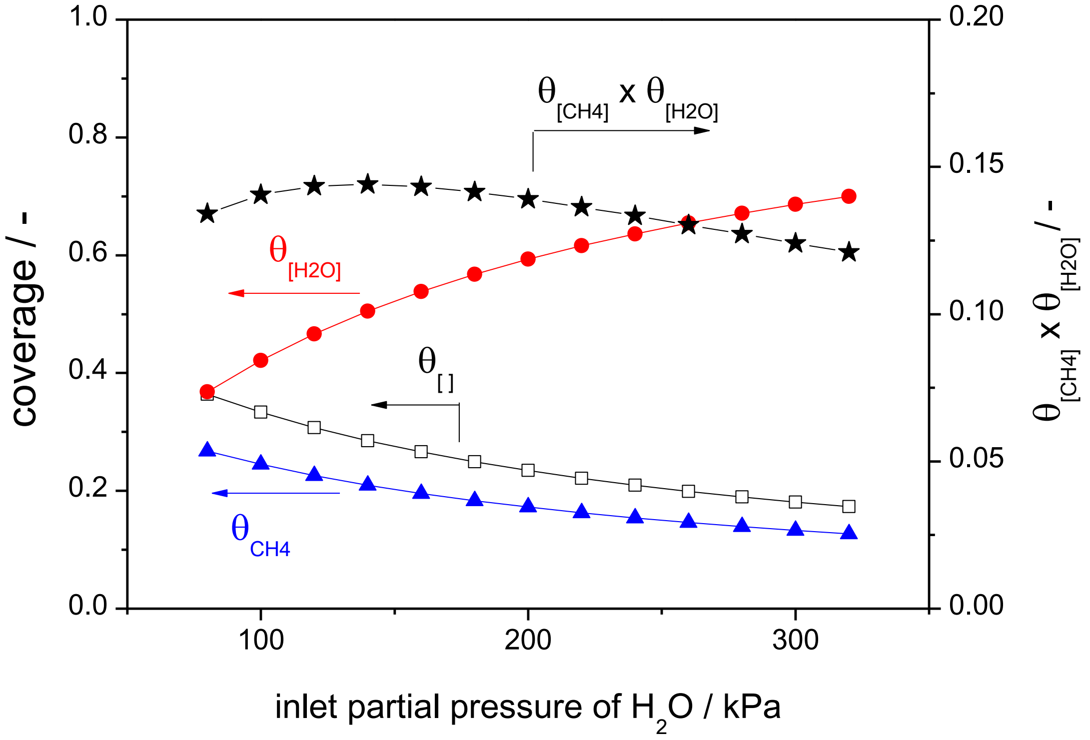

Fig. 2.7. Calculated coverage of catalyst surface by H_2O ($\theta_{[H2O]}$), CH_4 ($\theta_{[CH4]}$), empty sites ($\theta_{[\,]}$) and the product of $\theta_{[H2O]}$ and $\theta_{[H2O]}$ versus the inlet partial pressure of H_2O. Inlet partial pressure of CH_4: 80 kPa, Temperature: 650°C, Total pressure: 0.40 MPa, WHSV: 48000 $Ncm^3_{CH4}\ h^{-1}\ g_{cat}^{-1}$

As seen in Table 2.1, compared to the works reported in other studies, which were carried out at 0.10 MPa, the present study was conducted at 0.40 MPa, making the comparison difficult. However, substitution of the results of the regression (Table 2) into Eq. 13 and Eq. 14 can be used to calculate reaction rates for specific reaction conditions. The filled square in Fig. 2.2 shows the result of such a calculation at the same conditions as the point shown by the cross in Fig. 2.2 but at 0.10 MPa as with the rest of the points, not 0.40 MPa. The comparison shows that the conversion of CH_4

decreases with decreasing pressure as shown by the red arrow. This is an interesting result, as the equilibrium conversion decreases with increasing pressure due to the stoichiometry of the SMR reaction (increase in moles, Eq. 2.1). The increase in conversion with pressure is due to enhanced kinetics, with rates increasing with higher coverages of reactants as given by Eq. 8 and 9. This will be discussed subsequently.

Fig. 2.8 illustrates the effect of pressure with results of a simulation varying the total pressure with fixed reactant composition. It shows that higher pressure leads to higher reaction rate, as long as the reaction is not close to equilibrium. Those results rationalize why SMR is practiced industrially at high pressure, despite the unfavorable equilibrium.

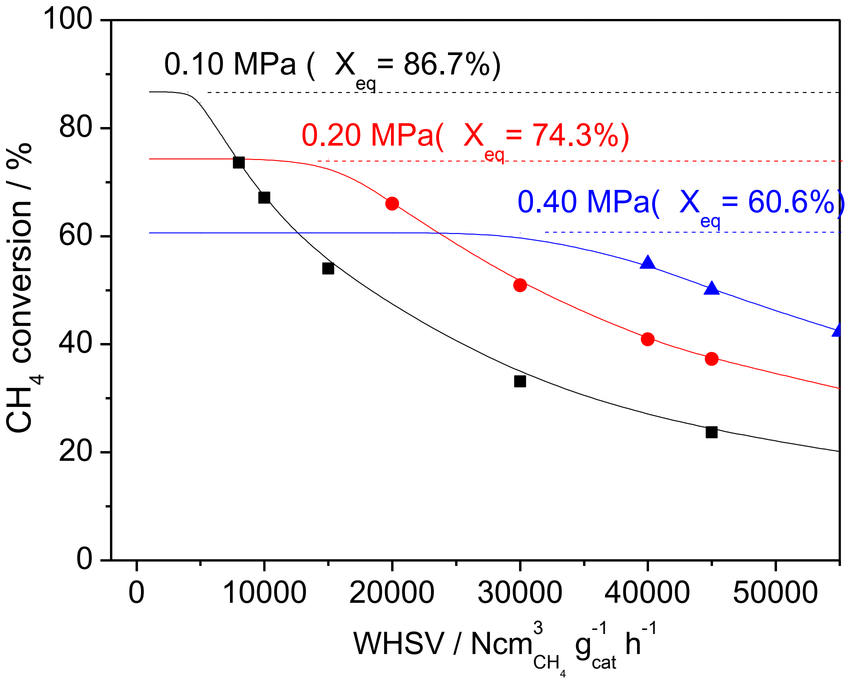

Fig. 2.8. Simulation result of CH_4 conversion change versus the WHSV of CH_4 at various pressures. The points are the result of the calculation with Eq. 13 and Eq. 14 and the lines are drawn by B-spline through the points including the equilibrium points, Temperature: 650 °C, Inlet gas composition; H_2O: CH_4: N_2 = 2:1:2. Dashed line shows the equilibrium CH_4 conversion for each reaction condition.

Fig. 2.9 shows the effect of H_2O/CH_4 ratio in simulation results for CH_4 conversion as a function of CH_4 WHSV. The CH_4 conversion is higher for higher H_2O/CH_4 ratios and decreases with increasing WHSV. These trends are similar to those seen in Fig. 2 for both higher and lower H_2O/CH_4 ratio. Thus, the simple model is able to describe general trends found from analysis of literature data.

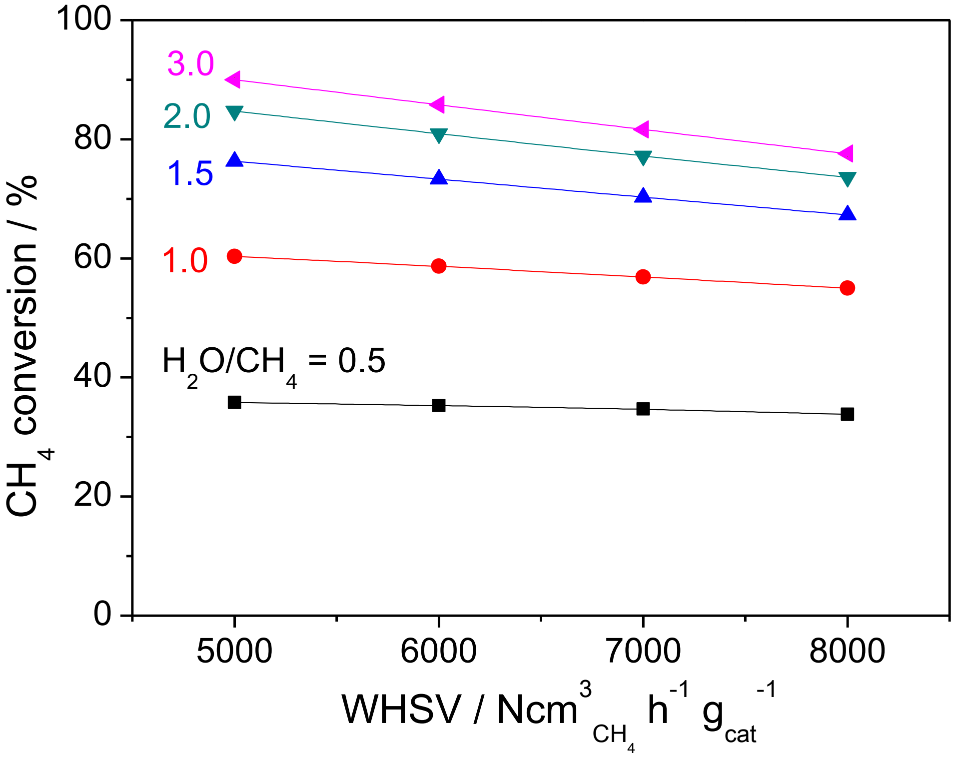

Fig. 2.9. Comparison of simulated CH_4 conversions as a function of WHSV of CH_4 varying H_2O/CH_4 ratios at 923 K, 0.10 MPa. The lines are drawn by B-spline through each points.

2.4 Conclusions

A $Ni/MgO\text{-}SiO_2$ catalyst was used to study the catalytic steam methane reforming in a tubular reactor at 0.40 MPa and 650°C. Measurements of the effect of the partial pressures of CH_4 and H_2O were made and the data were analyzed by a simple reaction model considering just adsorption of the reactants. The rate expression for methane consumption in steam methane reforming was $r = \frac{k_3' p_{\mathrm{CH_4}} p_{\mathrm{H_2O}}}{(1+K_1 p_{\mathrm{CH_4}}+K_2 p_{\mathrm{H_2O}})}$. The rate parameters were obtained by integral regression and estimates of the effect of pressure and H_2O/CH_4 ratio gave good agreement with experimental results and literature findings. The reaction model was used to develop simulations that showed agreement with general trends observed in steam methane reforming such as the decrease of CH_4 conversion with weight-hourly space velocity of CH_4 and total pressure of the reactor. The agreement of the experimental results in the present study obtained at a higher pressure (0.40 MPa) with those of recent studies conducted at lower pressure (0.10 MPa), indicates that the simple kinetic model analysis developed in this study captures the essential elements of the steam methane reaction.

Chapter 3. Verification and Evaluation of Kinetic Analysis Variants of the Steam Methane Reforming on a Ni/MgO-SiO$_2$ Catalyst

3.1 Introduction

Steam reforming of hydrocarbons, especially methane, plays an important role in industrial hydrogen production. This chapter will discuss the kinetics of the reaction, a subject which has been studied extensively by many researchers such as Numaguchi and Kikuchi [50], Xu and Froment [22], Hou and Hughes [51], Wang *et al*. [52], the group of Lasa [53], Tonkovich *et al*. [54], the group of Lin [55], Saito *et al*. [56], the group of Yang [36] and the group of Vlachos [57]. Much of the work done in the past was at atmospheric pressure, and the main objective of the present work is to carry out a limited study of the kinetics at a moderate pressure of 400 kPa.

Since steam methane reforming (SMR) is an endothermic reaction, higher temperature results in higher equilibrium conversion and industrially, SMR is operated at 973-1173 K, which results in high energy consumption [58]. In practice, SMR is also operated at high pressures of 0.13-2.0 MPa [59], and although high pressure is not favorable for reactions with a net increase in moles like the SMR the higher pressure results in higher hydrogen production rates [60].

There are usually four reactions considered when discussing the SMR.

Steam methane reforming to CO,

$CH_4 + H_2O \rightarrow CO + 3H_2$ $\Delta H = 206.3$ kJ/mol (Eq. 3.1)

Complete methane reforming to CO_2,

$CH_4 + 2H_2O \rightarrow CO_2 + 4H_2$ $\Delta H = 164.9$ kJ/mol (Eq. 3.2)

Dry reforming

$CH_4 + CO_2 \rightarrow 2CO + 2H_2$ $\Delta H = 247.3$ kJ/mol (Eq. 3.3)

Water-gas shift,

$CO + H_2O \rightarrow CO_2 + H_2$ $\Delta H = -41.1$ kJ/mol (Eq. 3.4)

Past work on the kinetics of SMR is extensive and will be summarized here. An early study by Numaguchi and Kikuchi reported an empirical expression using a power rate law form (Table 3.1, entry 1) that assumed a surface reaction to be the rate determining step [50]. The second term of the expression represents an effective methane pressure that accounts for the reversibility of the SMR reaction.

A subsequent influential study by Xu and Froment [22] considered that the rate of methane consumption was given by the sum of the rates to form CO (Eq. 3.5) and CO_2

(Eq. 3.6), with both reversible, and took into consideration the water-gas shift reaction (Eq. 3.7). Assuming that the surface was occupied by CO, H_2, CH_4, and O (Eq. 3.8), they developed an expression for the overall rate of methane consumption (Table 3.1, entry 2).

$$r_1 = \frac{k_1}{P_{\mathrm{H_2}}^{2.5}}\left(P_{\mathrm{CH_4}}P_{\mathrm{H_2O}} - \frac{P_{\mathrm{H_2}}^3 P_{\mathrm{CO}}}{K_1}\right)\frac{1}{(\mathrm{DEN})^2} \qquad \text{(Eq. 3.5)}$$

$$r_2 = \frac{k_2}{P_{\mathrm{H_2}}^{3.5}}\left(P_{\mathrm{CH_4}}P_{\mathrm{H_2O}}^2 - \frac{P_{\mathrm{H_2}}^4 P_{\mathrm{CO_2}}}{K_2}\right)\frac{1}{(\mathrm{DEN})^2} \qquad \text{(Eq. 3.6)}$$

$$r_3 = \frac{k_3}{P_{\mathrm{H_2}}}\left(P_{\mathrm{CO}}P_{\mathrm{H_2O}} - \frac{P_{\mathrm{H_2}} P_{\mathrm{CO}}}{K_3}\right)\frac{1}{(\mathrm{DEN})^2} \qquad \text{(Eq. 3.7)}$$

$$\begin{aligned}\mathrm{DEN} = 1 &+ K_{\mathrm{CO}}P_{\mathrm{CO}} + K_{\mathrm{H_2}}P_{\mathrm{H_2}} + K_{\mathrm{CH_4}}P_{\mathrm{CH_4}} \\ &+ K_{\mathrm{H_2O}}\frac{P_{\mathrm{H_2O}}}{P_{\mathrm{H_2}}}\end{aligned} \qquad \text{(Eq. 3.8)}$$

These expressions by Xu and Froment explained the behavior of the reactant and product species in a simple manner and have been widely used. Hou and Hughes revised the model of Xu and Froment, again assuming that the reforming to CO (Eq. 3.1) and the reforming to CO_2 (Eq. 3.2) were both reversible and occurred in parallel, but used different rate expressions for the forward reactions. They also assumed that CH_4 was not adsorbed [51]. A recent study by Wang *et al*. presented two models assuming a pair of reactions for each [52]. One was a simple model that considered that the reactions of steam reforming to CO (Eq. 3.1) and to CO_2 (Eq. 3.2) occurred in parallel, and the other considered the reaction of reforming to CO_2 (Eq. 3.2) and the dry reforming reaction (Eq. 3.4). The group of Lasa developed six models for SMR and concluded that a model that assumed that methane adsorption was the rate-determining step explained their results most accurately [53]. A study using a microchannel reactor by Tonkovich *et al*. employed a rather simplified model with less parameters to carry out an SMR reactor design [54].

Several studies employed simple power rate laws, in a phenomenological manner without considering the reaction steps. The group of Lin reported a power rate law model with activation energy [55]. Saito *et al.* considered the saturation of the catalyst surface occurred at certain conditions, which limited the reaction rate [56]. However, their expression were not more than empirical models for limited application.

Apart from power rate laws or the Xu and Froment model, other approaches have been studied such as a study by the group of Yang, which assumed a single total reaction and calculated the methane consumption rate based on a comparison between methane conversion and equilibrium conversion [36]. In a study by the group of Vlachos, they assumed that one of the reaction step on the catalyst surface was the rate determining step for both steam reforming and dry reforming, so that their rate expressions would be similar [57].

The kinetic expressions are summarized in Table 3.1. In their original publications, the authors assigned each variable arbitrary names, but here in this chapter, the expressions had been unified as shown in Table 3.2.

Table 3.1. Reaction rate expressions in methane steam reforming

CH_4 consumption rate expression (- r_{CH4})	Temperature K	Pressure MPa	Ref.
$\frac{k_{\mathrm{SMR}}\left(P_{\mathrm{CH_4}} - \frac{P_{\mathrm{CO}}P_{\mathrm{H_2}}^{3}}{P_{\mathrm{H_2O}}K_{\mathrm{SMR}}}\right)}{P_{\mathrm{CH_4}}^{n_1}P_{\mathrm{H_2O}}^{n_2}}$	674-1160	0.12-2.55	50
$\frac{\frac{k_{\mathrm{SMR}}}{P_{\mathrm{H_2}}^{2.5}}\left(P_{\mathrm{CH_4}}P_{\mathrm{H_2O}} - \frac{P_{\mathrm{H_2}}^{3}P_{\mathrm{CO}}}{K_{\mathrm{SMR}}}\right) + \frac{k_{\mathrm{CMR}}}{P_{\mathrm{H_2}}^{3.5}}\left(P_{\mathrm{CH_4}}P_{\mathrm{H_2O}}^{2} - \frac{P_{\mathrm{H_2}}^{4}P_{\mathrm{CO_2}}}{K_{\mathrm{CMR}}}\right)}{\left(1 + K_{\mathrm{CO}}P_{\mathrm{CO}} + K_{\mathrm{H_2}}P_{\mathrm{H_2}} + K_{\mathrm{CH_4}}P_{\mathrm{CH_4}} + K_{\mathrm{H_2O}}\frac{P_{\mathrm{H_2O}}}{P_{\mathrm{H_2}}}\right)^{2}}$	573-848	0.3-1.5	22
$\frac{\frac{k_{\mathrm{SMR}}P_{\mathrm{CH_4}}P_{\mathrm{H_2O}}^{0.5}}{P_{\mathrm{H_2}}^{1.25}}\left(1 - \frac{P_{\mathrm{H_2}}^{3}P_{\mathrm{CO}}}{K_{\mathrm{SMR}}P_{\mathrm{CH_4}}P_{\mathrm{H_2O}}}\right) + \frac{k_{\mathrm{CMR}}P_{\mathrm{CH_4}}P_{\mathrm{H_2O}}}{P_{\mathrm{H_2}}^{1.75}}\left(1 - \frac{P_{\mathrm{H_2}}^{4}P_{\mathrm{CO_2}}}{K_{\mathrm{CMR}}P_{\mathrm{CH_4}}P_{\mathrm{H_2O}}^{2}}\right)}{\left(1 + K_{\mathrm{CO}}P_{\mathrm{CO}} + K_{\mathrm{H}}P_{\mathrm{H}}^{0.5} + K_{\mathrm{H_2O}}\frac{P_{\mathrm{H_2O}}}{P_{\mathrm{H_2}}}\right)^{2}}$	748-823	0.12-0.60	51
$k_{\mathrm{SMR}}P_{\mathrm{CH_4}}^{n_1}P_{\mathrm{H_2O}}^{n_2}\left(1 - \frac{P_{\mathrm{CO}}P_{\mathrm{H_2}}^{3}}{K_{\mathrm{SMR}}P_{\mathrm{CH_4}}P_{\mathrm{H_2O}}}\right) + k_{\mathrm{CMR}}P_{\mathrm{CH_4}}^{n_3}P_{\mathrm{H_2O}}^{n_4}\left(1 - \frac{P_{\mathrm{CO}}P_{\mathrm{H_2}}^{4}}{K_{\mathrm{CMR}}P_{\mathrm{CH_4}}P_{\mathrm{H_2O}}^{2}}\right)$	750-1020	0.1	52
$k_{\mathrm{CMR}}P_{\mathrm{CH_4}}^{n_1}P_{\mathrm{H_2O}}^{n_2}\left(1 - \frac{P_{\mathrm{CO_2}}P_{\mathrm{H_2}}^{4}}{K_{\mathrm{CMR}}P_{\mathrm{CH_4}}P_{\mathrm{H_2O}}^{2}}\right) + 0.5k_{\mathrm{DMR}}P_{\mathrm{CH_4}}^{n_3}P_{\mathrm{CO_2}}^{n_4}\left(1 - \frac{P_{\mathrm{CO}}^{2}P_{\mathrm{H_2}}^{2}}{K_{\mathrm{WGS}}^{-1}P_{\mathrm{CH_4}}P_{\mathrm{CO_2}}}\right)$	750-1020	0.1	52

$\frac{P_{\mathrm{CH_4}}}{k_1 + k_2 P_{\mathrm{CH_4}}}\left(1 - \frac{P_{\mathrm{CO}} {P_{\mathrm{H_2}}}^3}{P_{\mathrm{CH_4}} P_{\mathrm{H_2O}} K_{\mathrm{SMR}}}\right)$	1003-1073	0.35-2.41	53
$k_{\mathrm{SMR}}\left(P_{\mathrm{CH_4}} P_{\mathrm{H_2O}} - \frac{P_{\mathrm{CO}} {P_{\mathrm{H_2}}}^3}{K_{\mathrm{SMR}}}\right)$	811, 837	1.30	54
$k_{\mathrm{SMR}} \cdot {P_{CH_4}}^{n_1} \cdot {P_{\mathrm{H_2O}}}^{n_2} \cdot \exp\left(-\frac{E_{a,\mathrm{SMR}}}{RT}\right)$	873-1073	0.1	55
$\min\begin{cases} k_{\mathrm{SMR}} \cdot {P_{CH_4}}^{n_1} \cdot {P_{\mathrm{H_2O}}}^{n_2} \\ r_c (= const.) \end{cases}$	783-823	0.1	56
$\frac{k_{\mathrm{TOT}} P_{\mathrm{T}} F_{\mathrm{CH_4}} (X_{\mathrm{e}} - X)}{\left(F_{\mathrm{T}} + 2F_{\mathrm{CH_4}} X\right) X_{\mathrm{e}}}$	911-940	0.1	36
$\frac{f_1\left(c_{\mathrm{H_2}}, c_{\mathrm{CO}}\right) c_{\mathrm{CH_4}}}{\left[1 + f_2\left(c_{\mathrm{H_2}}, c_{\mathrm{CO}}\right)\sqrt{c_{H_2}}\right]\left[1 + f_3\left(c_{\mathrm{H_2}}, c_{\mathrm{CO}}\right)\sqrt{c_{H_2}} + f_4\left(c_{\mathrm{H_2}}, c_{\mathrm{CO}}\right) c_{\mathrm{CO}}\right]^2} \times \left[1 - \frac{P_{\mathrm{CO}} {P_{\mathrm{H_2}}}^3}{P_{\mathrm{CH_4}} P_{\mathrm{H_2O}} K_{\mathrm{SMR}}} + 1 - \frac{{P_{\mathrm{CO}}}^3 {P_{\mathrm{H_2}}}^3}{P_{\mathrm{CH_4}} P_{\mathrm{CO_2}} K_{\mathrm{DMR}}}\right]$	573-1123	0.1	57

Table 3.2. List of names of variables and abbreviations

name	Explanation	Other information
SMR	Steam methane reforming	$CH_4 + H_2O \rightarrow CO + 3H_2$
WGS	Water-gas shift reaction	$CO + H_2 \rightarrow CO_2 + H_2$
RWGS	Reverse water-gas shift	$CO_2 + H_2 \rightarrow CO + H_2$
CMR	Complete methane reforming	$CH_4 + H_2O \rightarrow CO_2 + 4H_2$
DMR	Dry methane reforming	$CH_4 + CO_2 \rightarrow 2CO + 2H_2$
TOT	Total reaction	
T	reaction temperature	
F_{T}	Total flow rate	
F_{i}	Flow rate of i	i: component
P_{i}	Partial pressure of i	i: component
P_{T}	Total pressure	
X	Methane conversion	
X_{e}	Equilibrium methane conversion	
R	Gas constant	
k_{X}	reaction rate constant for reaction X	X: reaction
k_{j}	j th constant used in an equation	j:number
r_{c}	reaction rate at constant value	
K_{i}	Adsorption equilibrium constant of i	i: component
K_{X}	Equilibrium constant of reaction X	X: reaction
n_{i}	Order of reaction	j: number
f_{j}(a,b)	j th function of a and b*	j: number a,b: parameters
c_{i}	Concentration of component i	i: component

*for detail of the functions, see reference [57]

3.2 Experimental

In this work the catalytic steam methane reforming was studied using a Ni/MgO-SiO_2 catalyst supplied by JGC Catalysts and Chemicals Ltd. According to the supplier information, the composition of the NiO/MgO-SiO_2 catalyst was 53.0-58.0wt% NiO, 8.1-11.1wt% MgO, 24.2-28.2wt% SiO_2. The BET area was measured to be 100 m^2 g^{-1} by N_2 adsorption at 77 K using a volumetric apparatus (BELSORP-mini, Microtrac BEL Corp.). The H_2 chemisorption uptake at 313 K over the same catalyst after 12 h reduction at 923 K in 5% H_2/Ar was 90 μmol g^{-1} with a pulse measurement apparatus (CHEMBET-3000, Quantachrome Instruments).

The total pressure of the reactor was kept at 400 kPa but the partial pressure of each reactant varied as follows; 20-140 kPa for CH_4, 80-280 kPa for H_2O, with N_2 gas as the balance. The catalyst amount used was 0.10 g and was diluted 40 fold with quartz sand (SiO_2, Wako Pure Chemical Industries Ltd.) to form a 3.0 cm^3 catalyst bed, which was held in the middle of a vertical tubular reactor with quartz sand (Fig. 3.1). The catalyst particles were sieved to 400-630 μm diameter, and the quartz sand to 600-850 μm. The bed was located in the annular region between an inner dense alumina tube and an outer quartz sleeve, both of which were enclosed in a stainless shell. The geometry was chosen for future membrane reactors studies in which the solid alumina tube would be replaced by a tubular ceramic membrane of the same dimensions. The temperature was fixed at 923 K (650^{o}C) and the catalyst was reduced in H_2 at the same temperature for 12 h before use. The flows of reactant CH_4 and dilution gas N_2 were fed to a vaporizer held at 473 K where water vapor was added and then the mixture was introduced to the reactor from the top. The outlet gas from the lower side of the reactor was kept heated in order to avoid condensation of water vapor and was passed through a water separator consisting of an eight-way valve and a combination of three columns, Shincarbon, Porapak-Q and Molecular sieve 5A. This water elimination was necessary to prevent tailing of the gas chromatographic peaks. The gases were then analyzed by a gas chromatograph (GC-8A, Shimadzu Co.) with a thermal conductivity detector (TCD). The amount of water was not measured directly but obtained as the average of the two calculated values based on separate mass balances of hydrogen and oxygen.

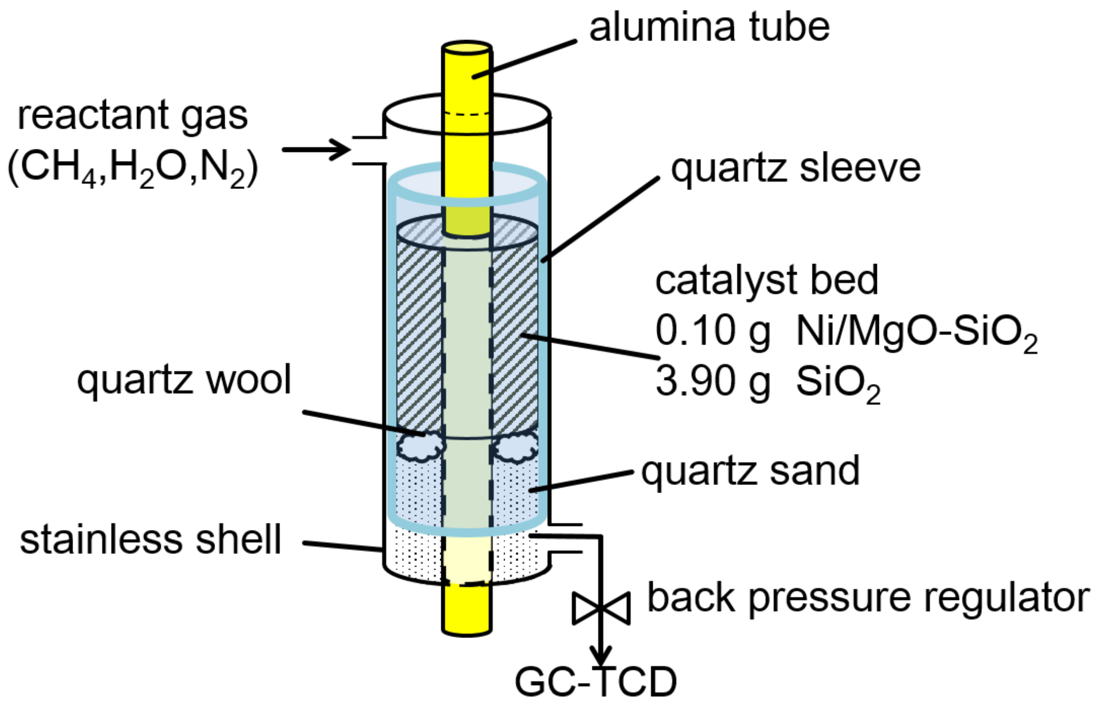

Fig. 3.1. Diagram of the reactor used for steam methane reforming

The gases used in the experiment were CH_4 (99% Toatsu Yamazaki Co., Ltd.), H_2 (99.99% Showa Denko Gas Products Co., Ltd.), N_2 (99.99% Toatsu Yamazaki Co., Ltd.).

The models used in this study are shown in Table 3.3. The variables were defined following the nomenclature in Table 3.2.

Table 3.3. Kinetic models applied in this chapter

	Equation for SMR rate (r_{SMR}) Equation for WGS reaction rate (r_{WGS})	adsorption
Numaguchi model	$r_{SMR} = \frac{k_{\mathrm{SMR}}\left(P_{\mathrm{CH_4}}P_{\mathrm{H_2O}} - \frac{P_{\mathrm{CO}}{P_{\mathrm{H_2}}}^3}{K_{\mathrm{SMR}}}\right)}{{P_{\mathrm{CH_4}}}^{n_{SMR,1}}{P_{\mathrm{H_2O}}}^{n_{SMR,2}}}$ $r_{WGS} = \frac{k_{\mathrm{WGS}}\left(P_{\mathrm{CO}}P_{\mathrm{H_2O}} - \frac{P_{\mathrm{CO_2}}P_{\mathrm{H_2}}}{K_{\mathrm{WGS}}}\right)}{{P_{\mathrm{CH_4}}}^{n_{WGS1}}{P_{\mathrm{H_2O}}}^{n_{WGS2}}}$	none
Model with reactant adsorption	$r_{SMR} = \frac{k_{SMR}K_{CH_4}K_{H_2O}\left(p_{CH_4}p_{H_2O} - \frac{p_{CO}{p_{H_2}}^3}{K_{SMR}{p_0}^2}\right)}{\left(1 + K_{CH_4}p_{CH_4} + K_{H_2O}p_{H_2O}\right)^2}$ $r_{WGS} = \frac{k_{WGS}K_{H_2O}\left(p_{CO}p_{H_2O} - \frac{p_{CO_2}p_{H_2}}{K_{WGS}}\right)}{1 + K_{CH_4}p_{CH_4} + K_{H_2O}p_{H_2O}}$	CH_4, H_2O
LHHW model	$r_{SMR} = \frac{k_{SMR}K_{CH_4}K_{H_2O}\left(p_{CH_4}p_{H_2O} - \frac{p_{CO}{p_{H_2}}^3}{K_{SMR}{p_0}^2}\right)}{\left(1 + K_{CH_4}p_{CH_4} + K_{H_2O}p_{H_2O} + K_{CO}p_{CO} + K_{CO_2}p_{CO_2} + K_{H_2}p_{H_2}\right)^2}$ $r_{WGS} = \frac{k_{WGS}K_{H_2O}K_{CO}\left(p_{CO}p_{H_2O} - \frac{p_{CO_2}p_{H_2}}{K_{WGS}}\right)}{\left(1 + K_{CH_4}p_{CH_4} + K_{H_2O}p_{H_2O} + K_{CO}p_{CO} + K_{CO_2}p_{CO_2} + K_{H_2}p_{H_2}\right)^2}$	CH_4, H_2O, CO, CO_2, H_2

LHHW: Langmuir-Hinshelwood-Hougen-Watson,

Power-rate law models are the simplest and have been used extensively because of the simplicity of their functional form and because they can be developed with a limited number of variables. They provide simple information about the contribution of each reactant, but lack mechanistic information. Numaguchi and Kikuchi [50] developed an empirical model based on this power-rate law (simply referred as Numaguchi model in Table 3.3 and the rest of this chapter). As an advanced modeling approach, a model with reactant adsorption was applied to the experimental result. Langmuir-Hinshelwood-Hougen-Watson model (referred as LHHW model in Table 3.3 and the rest of this chapter) is adopted as another variant of this approach. The assumption of these models that the reaction takes place between two or more adsorbates on a catalyst surface, and are widely used in expressions for catalytic reaction. In the model with reactant adsorption, only CH_4 and H_2O is assumed to be adsorbed to the catalyst surface as the reactant of SMR then the products desorbed just after its production, and following WGS takes place between H_2O on catalyst surface and CO in the gas phase (Eley-Rideal mechanism). On the other hand, in the LHHW model, all the products and reactants except inert N_2 may be adsorbed to the catalyst surface.

3.3 Results and Discussion

Each model was regressed and statistically analyzed through the microKinetic Engine (μKE), a kinetic modeling and regression software developed at Ghent University [32]. The reactor is taken as typical plug flow reactor in steady-state. The molar flow of each component is calculated with the following differential equation, where F_i is the molar flow rate, F_i^o is the initial flow rate, r_i is the reaction rate of component i, and W is the catalyst weight. $\mathrm{d}F_i = -R_i dW \quad F_i(W=0) = F_i^0$

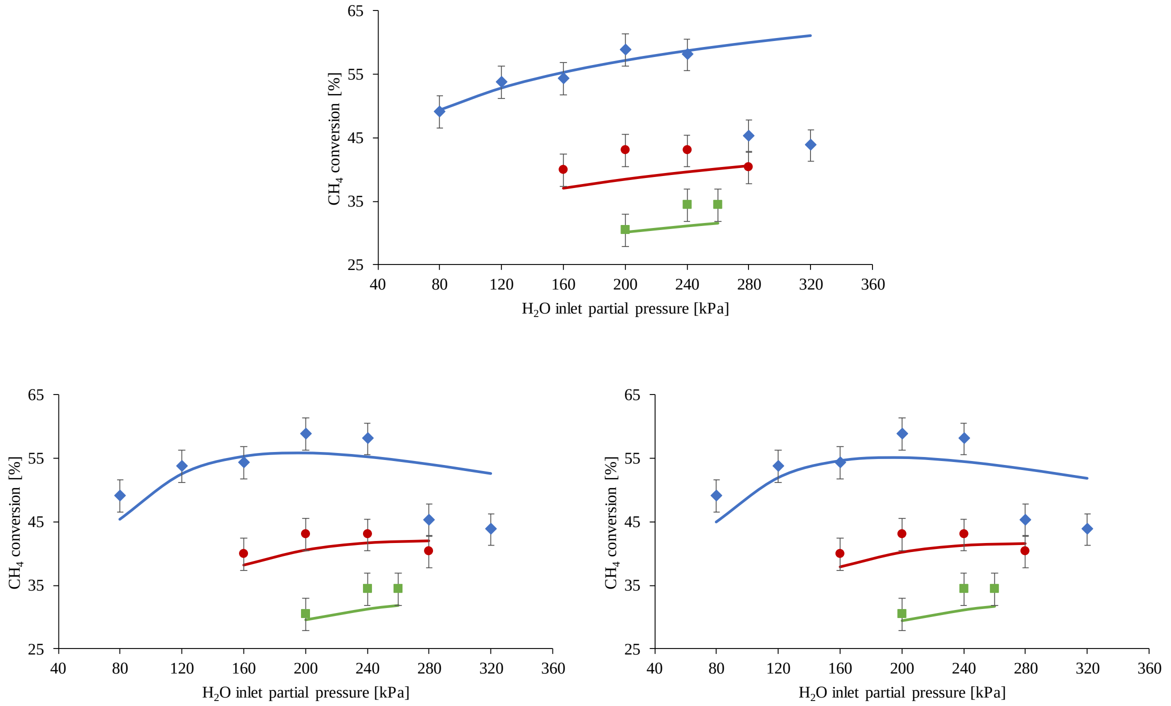

Fig. 3.2 Conversion of CH_4 versus inlet partial pressure of H_2O at a total pressure of 0.4 MPa and a temperature of 923 K. Symbols: observed experimental values. Lines: calculated by solving the plug flow model with the reaction rates given by the Numaguchi model, the model with reactant adsorption and the LHHW model. The rate and equilibrium coefficients and the partial reaction orders are obtained by a weighted regression and are shown in Table 3.5 and Table 3.6 ♦ – 40 kPa inlet partial pressure of methane ($p_{\mathrm{CH4,in}}$) and a space time of 3.36 $\mathrm{kg_{cat}\ s\ mol_{CH4}^{-1}}$, ● – 80 kPa $p_{\mathrm{CH4,in}}$ and a space time of 1.68 $\mathrm{kg_{cat}\ s\ mol_{CH4}^{-1}}$, ■ – 120 kPa $p_{\mathrm{CH4,in}}$ and a space time of 1.12 $\mathrm{kg_{cat}\ s\ mol_{CH4}^{-1}}$. Top: Numaguchi model; down left: model with reactant adsorption; down right: LHHW model.

Table 3.4. Residual figure of the outlet molar flow rate of CH_4, H_2O and CO_2 as a function of the methane inlet partial pressure for the regression at a total pressure of 0.4 MPa and a temperature of 923 K, of the Numaguchi model, the model with reactant adsorption and the LHHW model. The rate and equilibrium coefficients and the partial reaction orders are obtained by a weighted regression and are shown in Table 3.5 and Table 3.6.

	Numaguchi model	Model with reactant adsorption	LHHW model
CH_4	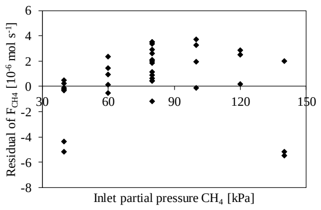	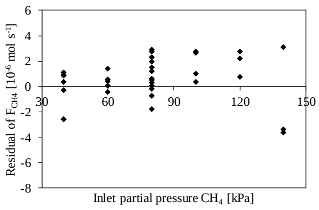	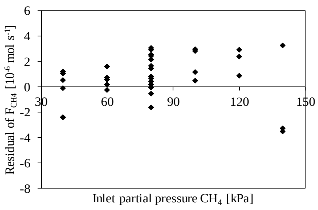
H_2O	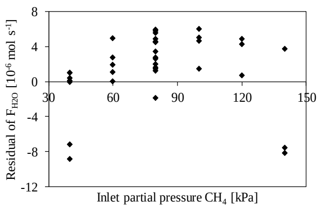	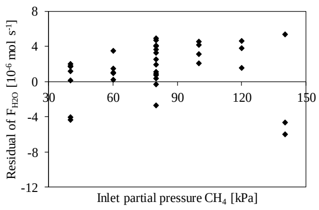	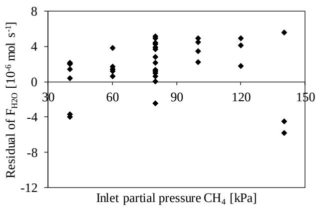
CO_2	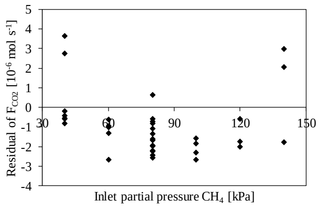	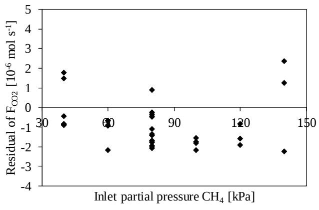	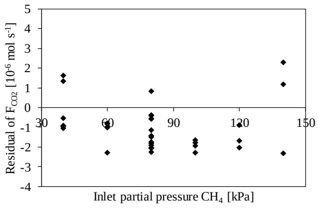

The data in the top of Fig. 3.2 indicates the Numaguchi model cannot describe the trends of CH_4 conversion, especially the decrease with excess H_2O at the inlet when the partial pressure of CH_4 is small (blue line). The regressed parameters and 95% confidence intervals of the Numaguchi model are shown in Table 3.5. The regression showed a global significance with calculated F_s value of 7.83×10^3 ($F_{s,tab} = 2.66$) but seemed to be inadequate with a calculated F_a value of $2.89 > F_{a,tab} = 1.49$. This model is based on a simple power-rate law with consideration of the kinetic equilibrium and it allows tuning of partial reactions orders with the constants of $n_{SMR,1}$, $n_{SMR,2}$, $n_{WGS,1}$, and $n_{WGS,2}$. However, the regression assessed $n_{WGS,1}$ and $n_{WGS,2}$ as redundant to the model and they were fixed at a value of zero, just as seen in Numaguchi and Kikuchi's report [50]. The partial reaction order of CH_4 ($1- n_{SMR,1}$) was regressed as 0.37, which is far from nominal value of one. It implies that this model misses some feature of the reaction, such as competitive adsorption on the catalyst surface. The partial reaction order of H_2O ($1- n_{SMR,2}$) was regressed as 0.13. This also indicates some missing features, in addition, it is seen that the partial pressure of H_2O has a limited impact in the reforming step.

Table 3.5. Parameter estimates and the corresponding 95 % confidence intervals for the Numaguchi model. * = parameter kept fixed during regression.

	95 % confidence interval	units
k_{SMR}	1.09 ± 0.37	10^5 mol $s^{-1}kg^{-1}MPa^{n1SMR+n2SMR-2}$
k_{WGS}	2.53^*	10^{12} mol $s^{-1}kg^{-1}MPa^{n1WGS+n2WGS-2}$
$n_{1,SMR}$	0.633 ± 0.050	-
$n_{2,SMR}$	0.873 ± 0.069	-
$n_{1,WGS}$	0^*	-
$n_{2,WGS}$	0^*	-

For the calculated CH_4 conversion of the model with reactant adsorption and LHHW model, the results in the lower left and right of Fig.3.2 show similar findings, with better fits to the experimental data. The difference between the Numaguchi model and the observed data indicates that the contribution of competitive adsorption is needed for improvement of the model. In this research, the adsorption and desorption of reactants and products are in quasi-equilibrium and they are absorbed molecularly in order to limit the complexity of the model. Generally, CH_4 is taken to dissociate on the catalyst surface with formation of carbon, CH_{i*} (i=1,2,3), O*, OH* and H_2 [22,49]. Therefore, the surface of the catalyst is considered to be covered by those intermediates and it means the assumption of those models is incorrect, however, it still explains the competition among the adsorbents. The regression result of these models is listed in Table 3.6. The regression of the model with reactant adsorption was calculated to be globally significant, $F_{s,calc} = 1.06x10^4 >> F_{s,tab} = 2.42$ but statistically inadequate, $F_{a,calc} = 1.62 > F_{a,tab} =1.49$. On the other hand, the regression of LHHW was also showed a global significance with $5.33x10^3$ $F_{s,calc}$ and 2.06 $F_{s,tab}$ but remained still inadequate with 1.61 $F_{a,calc}$ against 1.49 $F_{a,tab}$.

Table 3.6. Parameter estimates and the corresponding 95% confidence intervals for the model with reactant adsoption and the LHHW model. #=non-significant parameter

	95 % confidence intervals		units
	model with reactant adsorption[a]	LHHW model[b]	
K_{CH4}	27.1 ± 4.5	26.6 ± 4.0	MPa^{-1}

K_{H2O}	11.9 ± 2.2	11.9 ± 2.0	MPa^{-1}
k_{SMR}	11.9 ± 2.2	1.66 ± 0.12	mol s^{-1} kg$_{cat}^{-1}$
k_{WGS}	2.81 ± 0.97	1.84 ± 0.12	[a] 10^{9} mol s^{-1}kg$_{cat}^{-1}$ MPa^{-1} [b] 10^{11} mol s^{-1}kg$_{cat}^{-1}$ MPa^{-1}
K_{CO}	/	0.240[#]	MPa^{-1}
K_{CO2}	/	0.00313[#]	MPa^{-1}
K_{H2}	/	0.00627[#]	MPa^{-1}

All the parameters in the model with reactant adsorption are not correlated and significantly different from zero. As the result of the regression of LHHW model, the adsorption of the product was found to be redundant by global insignificance of them. In addition, the regressed adsorption equilibrium constant of LHHW model were very close to those of the model with reactant adsorption thus these two models showed the same trend as Fig. 3.2 and Table 3.4. despite the difference in the reaction rate expressions. This is possibly explained by quick desorption of the products or the difficulty of the estimation of surface coverage because of high CH_4 conversion (20-60%) and the high reaction rate of WGS.

In both models, the k_{WGS}, the reaction rate constant of WGS has a much greater value compared to k_{SMR}. This allows WGS to reach and keep the equilibrium state at the very beginning of the catalyst bed. In the experimental result, WGS were generally close to the equilibrium state. Considering the model simplicity, the model with reactant adsorption has the optimum balance between the reliability and the simplicity of the model.

3.4 Conclusions

A regression model of the kinetics of the steam methane reforming reaction was carried out with a set of experimental result on Ni/MgO-SiO_2 catalyst with a constant temperature, flow rate and total pressure varying the composition of the inlet gas. As the first model, Numaguchi model was investigated. It is an empirical model based on power law model adding a kinetic driving force and found to be globally significant. This model could explain the rough outline of the reaction, but lacks a flexibility especially at the overfeeding state of the methane. As the second and third model, the model with reactant adsorption and the Langmuir-Hinshelwood-Hougen-Watson model were discussed. They are designed in the same basic concept of competitive adsorption on the catalyst surface. The second model considers the reactant adsorption on the catalyst just like its name and the third model deals the both adsorption of the reactant and the product. They showed the better fittings than the Numaguchi model and explained the trends of experimental data. These two models showed almost the same performance therefore in this research, the model with the reactant adsorption is the most proper for the present data set among the discussed three models.

Chapter 4. Synthesis and characterization of a silica-alumina composite membrane and its application in a membrane reactor

Hydrothermally stable silica-alumina composite membranes were synthesized through chemical vapor deposition (CVD) of tetraethylorthosilicate (TEOS) and aluminium tri-sec-butoxide precursor at 923 K on porous alumina supports. The membranes showed high hydrogen permselectivity (order of 10^{-7} mol $m^{-2}s^{-1}Pa^{-1}$) comparable to that of a pure silica membrane but with superior hydrothermal stability, and were used in a membrane reactor. The permeation of small gas species (H_2, He, Ne) was well explained by a solid-state diffusion mechanism, involving jumps of the permeating species between solubility sites. The permeation mechanism of large gas molecules (CH_4, CO_2, N_2) was explained by the gas translation mechanism involving large pore defects. Steam methane reforming (SMR) on a Ni/MgO-SiO_2 catalyst was carried out at 923 K in the membrane reactor and in a conventional packed-bed reactor. The membrane contributed to an increase in the hydrogen production rate by the selective extraction of hydrogen from the reaction zone.

4.1 Introduction

Hydrogen plays an important role in today's chemical industry, especially in the refining of petroleum and the synthesis of chemical products. Recently, hydrogen has received considerable attention as an energy source for fuel cells because of their high energy conversion efficiency [61]. For the usage of hydrogen in ammonia synthesis [61,62] and in fuel cells slight amounts of impurities can poison the catalysts [63] and hydrogen purification is required. Currently, the majority of hydrogen is produced by steam reforming of fossil fuels such as methane in natural gas [64]. Steam reforming is a strongly endothermic reaction, so requires considerable amounts of heat to sustain the reaction. It is expected that hydrogen production with high efficiency will decrease operating temperatures and will improve process economics.

The present paper describes the use of a membrane reactor to simultaneously produce and purify hydrogen so as to improve efficiency. The reaction studied is the steam methane reforming (SMR).

$$CH_4 + H_2O \leftrightarrows CO + 3H_2 \qquad \varDelta H^{o}_{298} = 206\ \mathrm{kJ\ mol^{-1}}$$

$$CO + H_2O \leftrightarrows CO_2 + H_2 \qquad \varDelta H^{o}_{298} = -41\mathrm{kJ/mol^{-1}}$$

The SMR reaction produces a net increase in moles, so that methane conversion in a traditional reactor decreases with pressure increase. However, in a membrane reactor the conversion can increase because hydrogen permeance is enhanced by the pressure increase [65].

Membrane separation has advantages such as low operating costs and simplicity compared to other processes [66]. In addition, membrane reactors are an attractive emerging application which have considerable potential in chemical and fuels processing. For example, in membrane reactors for hydrogen generation reactions such as steam reforming, hydrogen permselective membranes extract hydrogen from the reaction zone preferentially and this extraction causes the reaction equilibrium to shift to the product side, thus increasing reactant conversion and hydrogen yield. In this case, the membrane works not only as a purifier, but as a reaction accelerator and makes hydrogen generation more effective. The subject has been studied extensively [67,68,69]. Shirasaki et al. described a practically scaled membrane reactor which generates 40 Nm^3 of hydrogen per hour. This reactor was used for the steam reforming of natural gas (composition: 88.5% CH_4, 4.6% C_2H_6, 5.4% C_3H_8, 1.5% C_4H_{10}) with a Ni/Al_2O_3 catalyst. It showed high energy efficiency of 70-76% [70]. By introducing hollow fiber membranes, with large surface area to volume ratio, Gil et al. increased the membrane separation efficiency [71].

Metallic membranes such as palladium have the best performance in hydrogen separation and have been applied commercially. A palladium membrane showed high hydrogen permeance and the permeance of N_2 was undetectably small so as to make the H_2/N_2 selectivity infinite [72]. However, palladium membranes suffer from a number of drawbacks [73]. First, they are susceptible to poisoning by sulfur compounds usually present in real feeds and also by carbon monoxide generated in the reaction [74]. Second, the metal is embrittled by the dissolution of hydrogen at certain conditions, and can undergo a phase transition which changes its volume and causes defect formation [75]. Third, the presence of grain boundaries can lead to defect formation [76]. Fourth, the metal is expensive, especially in the scale of use needed for industrial applications.

Amorphous silica membranes are also known for their high hydrogen permselectivity [77,78,73]. They operate at higher temperatures than palladium membranes and so are more appropriate for applications like SMR, and will be the subject of this research. They are mainly synthesized by chemical vapor deposition (CVD) or sol-gel methods from silica sources such as tetraethylorthosilicate (TEOS) [79,80], one of the most typical silica precursors. The sol-gel method usually consists of forming silica polymeric or particulate suspensions derived from alkoxide precursors, followed by dip-coating a mesoporous substrate and then controlled drying and firing at high temperatures. This resulting membranes have relatively high gas permeation rates, mainly due to the very thin top layers, of the order of 50-100 nm [81,82,83]. However, the resulting selectivity is limited because the pore structure of the material is formed by particle packing. The CVD method is used to modify the surface of support membranes by depositing thin films on a substrate by the reaction of one or several gas phase precursors. Although the gas permeances are generally lower than those of the sol-gel counterparts, the selectivities are higher. The CVD methods are superior to the sol-gel methods because the CVD is more reproducible and easier to implement. Various starting materials are used as silica sources for CVD and sol-gel methods.

TEOS is used for both methods [84, 85], while tetramethylorthosilicate (TMOS) [86], triphenylmethoxysilane (TPMS) [87] and dimethoxydiphenylsilane (DMDPS) [88] are used for CVD. When relatively large-sized silica species such as DMDPS are used, large pores may be formed. Methacryloxypropyltrimethoxysilane (MOTMS) [89] and SiH_4 [78] have been used in sol-gel methods.

An advantage of amorphous silica is its stability against chlorine, carbon monoxide, or hydrogen sulfide which cause harm to metallic membranes. However, silica membranes lose their hydrogen permselectivity when exposed to humid atmospheres at high temperature. Wu et al. reported that their silica membrane lost 62% of its permeability for helium after only 2 h exposure to 20 mol% steam at 673 K [90]. Sea et al. reported that their membrane lost 90% of H_2 permeance (from 3.5×10^{-6} mol m^{-2} s^{-1} Pa^{-1} to 4.0×10^{-7} mol m^{-2} s^{-1} Pa^{-1}) after 95 h exposure to 50 mol% H_2O at 400 ^{o}C [91]. They indicated that silica membranes seemed to experience densification and this caused reduction in hydrogen permeation. According to a report by Duke et al. [92], a siloxane bond on the surface of silica membrane reacts with an H_2O molecule and forms two silanol groups.

$$\equiv \mathrm{Si} - \mathrm{O} - \mathrm{Si} \equiv + \mathrm{H_2O} \rightarrow 2 \equiv \mathrm{Si} - \mathrm{OH}$$

These silanol groups can then condense again in different configurations that lead to a denser structure and the formation of voids. Duke et al. reported that silanol groups are likely to localize at narrower pores where higher attraction forces exist above 180 °C, and siloxane bond generation takes place across these narrow pores [92]. This thickening of solid silica by the forming of siloxane bonds decreases the permeation of smaller molecules such as H_2 and He but the formation of large pore defects allows larger molecules such as N_2, CH_4 to pass through. The introduction of additional elements in the amorphous silica network such as cobalt oxide [93], titanium oxide [94], niobium oxide [95] and zirconium oxide [13] reduce this densification.

This research focuses on the characterization of silica-alumina composite membranes and their application in a membrane reactor for steam methane reforming. Gu et al. reported that the hydrothermal stability of their membranes was improved by adding alumina or titania to the silica membranes [96]. In this research, hydrothermally stable silica-alumina composite membranes were synthesized and the permeance of the small gases He, H_2 and Ne as well as the larger gases CH_4, CO_2, N_2 and SF_6 were studied in detail, an aspect that was not covered in earlier studies. The use of the membrane in a membrane reactor for steam methane reforming at 0.4 MPa was demonstrated.

4.2. Experimental

4.2.1. Membrane preparation

Mesoporous alumina materials with cylindrical geometry of 3.0 cm length and pores of 5 nm diameter in the inner surface (6 mm ID, 10 mm OD, Pall Corp.) were used as supports for the permselective layers. The ends of the support were connected to two dense-alumina tubes of length 20 cm with glass seals formed by the melting at 1000 ^{o}C for 10 minutes of a glass paste precursor (Nippon Electric Glass Co., Ltd). The commercial alumina support had macro-pores on its outer surface and nano-pores on the inner surface. In order to remove large-pore defects and to smooth the surface, an intermediate layer was placed on the inner surface by the deposition of boehmite sols (dip coating). Following this, the membrane underwent chemical vapor deposition (CVD) also on the inner surface. Permeances of seven gas species; H_2, He, Ne, CH_4, CO_2, N_2, Ne, SF_6 were measured at 6 temperatures, every 100 K from 423 K to 923 K. Hydrothermal treatment was carried out at 923 K with 16 mol% H_2O/Ar gas to measure hydrothermal stability. Scanning electron microscopy (SEM) images were taken to determine the uniformity and thickness of each layer.

For the dip-coating process the outside of the membrane support was wrapped with Teflon tape and the tube was immersed into a boehmite sol suspension for 10 s and then dried 6 h or more in ambient air. The boehmite sol preparation is described later. Following the dip-coating the membrane was heated at a rate of 1.5 K/min to 923 K and was maintained at this temperature for 3 h to form a γ-alumina layer. This process could be repeated to deposit multiple γ-alumina layers.

After dip-coating and calcination, the membrane was kept at 923 K and CVD was carried out by passing argon gas saturated with tetraethylorthosilicate (TEOS, 96%, Tokyo Chemical Industry Co., Ltd.). A bubbler with a mantle heater kept at 298 K was used for delivering TEOS which has vapor pressure of 250 Pa at that temperature. Another stream of argon saturated with aluminum tri-sec-butoxide (ATSB, 97%, Wako Pure Chemical Industries, Ltd.) was introduced to the inside of the membrane after 15-20 minutes CVD with only TEOS. The bubbler containing ATSB was kept at 371 K, at which temperature ATSB has a vapor pressure of 10.4 Pa. These streams and an argon dilution gas were mixed and introduced to the inside of the membrane. Another argon stream was introduced to the outside of the membrane as a balance gas to equalize pressure and minimize the TEOS-containing gas from permeating through the membrane. Fig. 4.1 shows the apparatus used for the membrane synthesis. The flow rate of the balance gas was set a little faster than the flow rate of the stream inside of the membrane. TEOS and ATSB underwent thermal decomposition at 923 K and the amorphous silica-alumina composite layer was deposited on the surface of the intermediate layer.

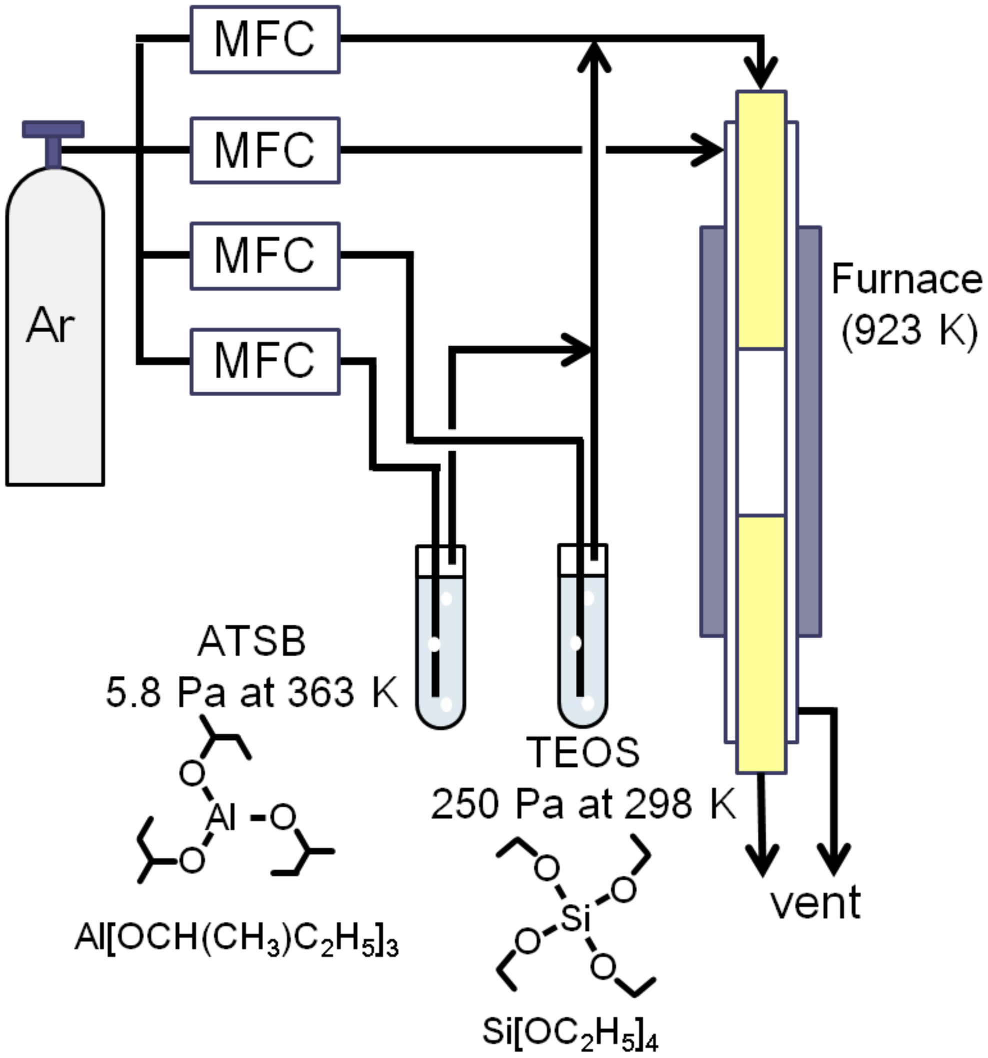

Fig. 4.1. Apparatus for membrane synthesis by chemical vapor deposition

The permeance of various gases through the membranes was measured with the same apparatus as used for their synthesis (Fig. 4.1). The gas permeance $\bar{P}_i$ [mol m^{-2} s^{-1} Pa^{-1}] was calculated from the surface area of the inside of the membrane A [m^2], the pressure difference between the inside and outside of the membrane Δp_i [Pa] and the molar flow of the gas which passed through the membrane $F_{p,i}$ [mol s^{-1}].

$$\bar{P}_{\mathrm{i}}\left[\mathrm{mol\ m^{-2}\ s^{-1}\ Pa^{-1}}\right]=\frac{F_{\mathrm{p,i}}\left[\mathrm{mol\ s^{-1}}\right]}{A\left[\mathrm{m^{2}}\right]\Delta P_{\mathrm{i}}[\mathrm{Pa}]} \qquad \text{(Eqn. 4.1)}$$

The performance of the membrane was evaluated by permeance and ideal H_2/N_2 selectivity ($S_{H2/N2}$) measurements. The latter was defined as the ratio of the pure gas permeances by the following equation (Eqn. 4.2)

$$S_{\mathrm{H_2/N_2}} = \frac{\overline{P_{\mathrm{H_2}}}}{\overline{P_{\mathrm{N_2}}}} \qquad \text{(Eqn. 4.2)}$$

The flow rates were measured with a bubble flow meter or when the flow rate was too low by concentration determinations at known carrier gas flow rates using a gas chromatograph (GC) equipped with a thermal conductivity detector (TCD). Helium gas was introduced to the permeate (outer) side of the membrane at a set flow rate and the concentration in helium flow was detected, to calculate the molar flow rate of the permeant.

The permeances of seven gases (H_2, He, Ne, CH_4, CO_2, N_2, Ne, SF_6) were measured at six temperatures (423, 523, 623, 723, 823, and 923 K). Hydrothermal treatment was carried out at 923 K with 16 mol% H_2O/Ar gas for 100 h to measure hydrothermal stability. For hydrothermal treatment an argon stream was introduced with a water bubbler heated to 56 ^{o}C, where the H_2O vapor pressure is 0.016 MPa to carry 16 mol% H_2O/Ar gas into the membrane.

4.2.2. Membrane Reactor

The silica-alumina membrane described earlier was installed in a reactor as shown in Fig. 4.2. The catalyst was a commercial Ni/MgO-SiO_2 catalyst (N-185, JGC Catalysts and Chemicals Ltd.). A quantity of 100 mg of catalyst was diluted 40 times by quartz sand to form a catalytic bed of 3.0 cm^2 volume which just covered the outside surface of the membrane. Both sides of the catalytic bed were held by quartz wool and quartz sand. The reactants for the steam methane reforming (SMR) were methane (10%) and steam (30-60%) with nitrogen as a balance and an internal standard and were introduced from the top of the reactor. Water was fed by a liquid pump and introduced to the vaporizer which was heated to 463 K. The lines from the vaporizer to the GC were heated by a ribbon heater to prevent water condensation.

A back pressure regulator at the exit of the shell side controlled the pressure in the reactor. A nitrogen stream flowed in the inside of the membrane as a sweep stream to carry hydrogen out of the reactor. The exhaust gas composition was measured by a gas chromatograph equipped with a TCD detector. The streams outside and inside of the membrane were analyzed individually. The concentrations of H_2, CH_4, CO, and CO_2 in the exhaust gases were measured by the ratio of peak areas against the peak area of N_2, which is inert in the reactions. The reactor was kept at 923 K and the temperature was controlled by a proportional-integral-derivative (PID) temperature controller with a thermocouple held at the bottom of the catalyst bed (Fig. 4.2)

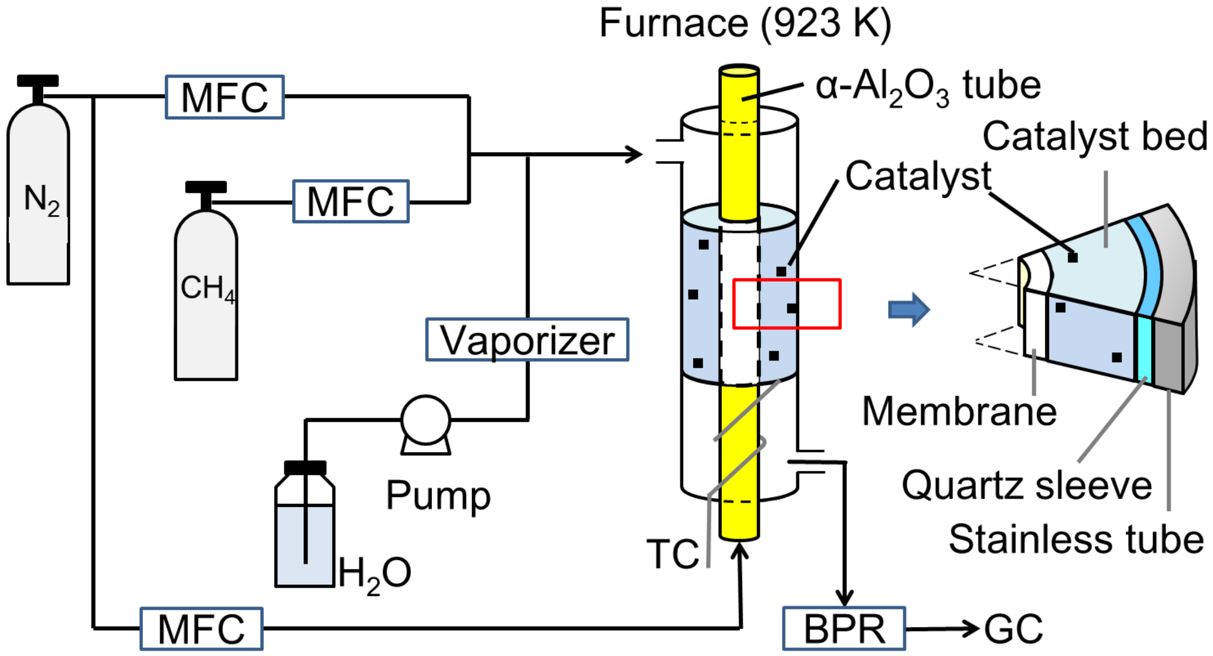

Fig. 4.2. Membrane reactor operation apparatus (MFC: Mass Flow Controller, TC: Thermocouple, BPR: Back Pressure Regulator, GC: Gas Chromatograph)

The result of the steam methane reforming in the membrane reactor operation was compared to packed-bed reactor operation. In the packed-bed reactor operation, the sweep nitrogen flow was stopped and both ends of the tube side of the membrane were closed. Separate experiments confirmed that the H_2 permeance was zero when the sweep gas was turned off. The reaction was maintained for 30 minutes for stabilization. The experimental results were compared to calculations obtained by a 1-D model.

4.3. Results and discussions

4.3.1 Membrane Synthesis

The membranes used in this study were prepared on commercial mesoporous alumina supports of cylindrical geometry (1 cm OD). Two intermediate γ-alumina layers were placed on the supports by dip coating of boehmite sols followed by drying and calcination. The diameters of the boehmite sols were controlled by the time of hydrolysis and the nitric acid /alkoxide ratio in the solution. The first γ-alumina layer was formed by a boehmite sol with 120 nm median diameter (Fig. 4.3a) and the second layer was formed by a boehmite sol with 30 nm median diameter (Fig. 4.3b). In the preparation of the sol for the first layer, the hydrolysis time was 50 h and the acid/alkoxide ratio was 0.08. In the preparation of the sol for the second layer, the hydrolysis time was 13 h and the acid/alkoxide ratio was 0.05. After placement of the second dip-coating layer the membrane was heated at 1.5 K/min rate to 923 K and kept at this temperature for 3 h to calcine the boehmite sol and form γ-alumina.

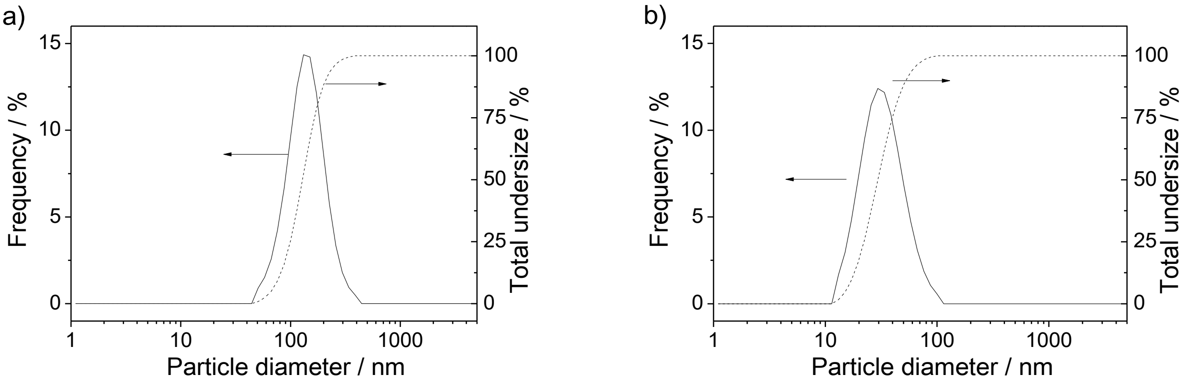

Fig. 4.3. Particle size distributions of the sols of a) 120 nm and b) 30 nm median diameter

Scanning electron microscopy (SEM) images of the porous support are shown in Fig. 4. Several layers are seen in the support, with larger particles of α-alumina at the bottom and smaller particles of γ-alumina at the top (Fig. 4.4a). These comprise parts of the support structure. The intermediate layer is 4-5 μm thick and is composed of γ-alumina (Fig. 4.4b). Separate layers are not clearly seen in the intermediate layer at this magnification.

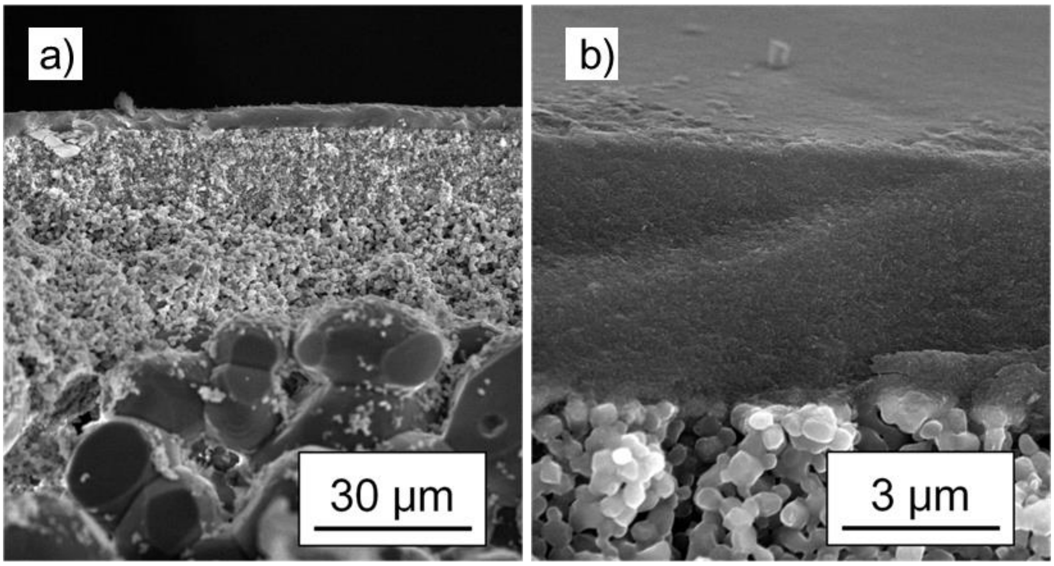

Fig. 4.4. SEM images of the cross section of the support

a) Low magnification showing overall structure (from bottom: large particles, small particles, intermediate layer) b) High magnification showing intermediate layer

For the actual membrane used in this study, a silica-alumina composite layer was placed on the intermediate layer by chemical vapor deposition at 923 K. Fig. 4.5 shows the permeance changes as a function of time for the silica-alumina composite membrane (Al/Si = 0.03). The data were obtained by periodically interrupting the synthesis, switching to Ar gas, and making permeance measurements without changing the temperature.

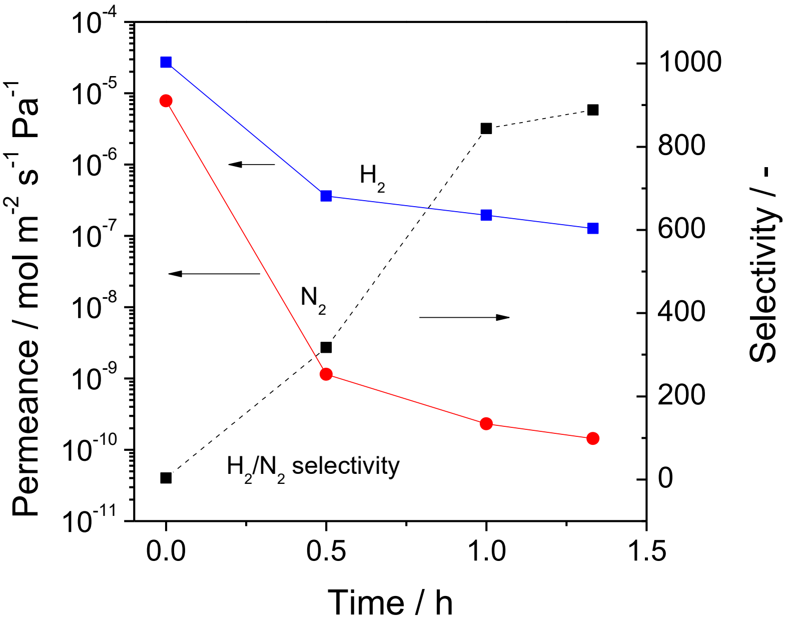

Fig. 4.5 Permeance and selectivity changes during the CVD process at 923 K for a silica-alumina composite membrane

The initial permeances were 2.7×10^{-5} mol m^{-2} s^{-1} Pa^{-1} for hydrogen and 7.8×10^{-6} mol m^{-2} s^{-1} Pa^{-1} for nitrogen, giving an initial H_2/N_2 selectivity of 3.5. This is close to the Knudsen ratio $\sqrt{\frac{M_{N_2}}{M_{H_2}}} = \sqrt{\frac{28}{2}} = 3.7$, and is consistent with the large size of the pores in the support. As the CVD process was carried out, the permeances of both gas species started to decrease and showed a steep drop in the first 0.5 h, especially for nitrogen. After 1.3 h (80 min) of CVD, the permeances were 1.3×10^{-7} mol m^{-2} s^{-1} Pa^{-1} for hydrogen and 1.4×10^{-10} mol m^{-2} s^{-1} Pa^{-1} for nitrogen, giving a H_2/N_2 selectivity of 890.

The SEM images of the silica-alumina composite membrane are shown in Fig. 4.6 at low magnification (Fig 4.6a), and high magnification (Fig 4.6b). In Fig. 4.6a, a number of layers can be seen. At the bottom there is a coarse layer made of sintered α-alumina particles. This layer is covered by a 3 μm thick layer of small particles that constitutes the γ-alumina portion of the support which gives rise to the nominal 5 nm diameter pores. On top of them two more layers can be discerned which are due to the two γ-alumina layers derived from successive placement of the boehmite sols. The CVD layer cannot be seen at lower magnification (Fig 4.6a), but with higher resolution (Fig 4.6b), a smooth dense layer of 30 nm thickness can be seen which is the silica-alumina layer.

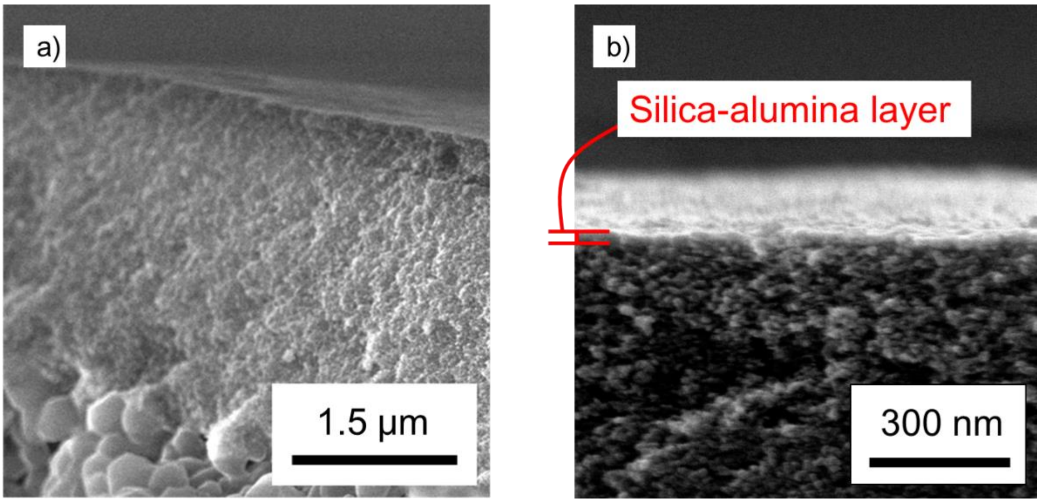

Fig. 4.6. SEM images of the cross section of silica-alumina composite membrane

4.3.2 Discussion of Theoretical Permeation Mechanisms

Before presenting the permeance properties of the CVD membranes it is worth to briefly review the mechanisms of permeance in porous and non-porous silica-based membranes, which are relevant to the present work. When CVD is carried out with precursors having organic substituents with direct Si-C bonds, these groups can be retained in the silica to disrupt the structure and form pores [97], which contribute to the permeance. When pores are present, gas transport takes place through several established processes, like the Knudsen and gas-translational mechanisms, that have a definite dependence on the pore size, kinetic diameter and molecular weight of the permeant gases [18]. However, when CVD is carried out with siloxane precursors with easily hydrolyzed Si-O-C alkoxide linkages, amorphous structures with a continuous network of Si-O-Si bonds form zeolite-like cages (solubility sites) that are randomly linked by siloxane windows, without continuous pores. The permeance of small gas species (He, H_2, Ne) can still be very high, with transport occurring by jumps through the windows between the sites by solid-state diffusion. It should be clarified that the term solid-state diffusion is used here to indicate passage of gaseous species through a solid by a transport process driven by concentration differences. Such transport includes, for example, methane permeation through carbon nanotubes [98] and carbon dioxide through polymeric membranes [99], and does not require chemical bonding between the permeating species and the solid. Thus, He and Ne, do not form chemical links with the silica matrix, but still undergo solid-state diffusion by random collisions with each other and the surfaces.

For the case in which pores are present, the transport mechanism depends on the width of the pores. When the width is smaller than the mean free path of the gas molecules but wide enough to be free from the potential field of the pore wall, the transport occurs by the Knudsen mechanism [100,101] and is given by the following equation (Eqn. 4.3).

$$\bar{P} = \frac{\varepsilon d_{\mathrm{p}}}{\tau L}\left(\frac{8}{9\pi MRT}\right)^{\frac{1}{2}} \qquad \text{(Eqn. 4.3)}$$

In this equation $\bar{P}$[mol m^{-2}s^{-1}Pa^{-1}] is the permeance, ε is the porosity (~ 0.5), τ [-] is the tortuosity (~ 10), L [m] is the thickness of the membrane, M [kg mol^{-1}] is the molecular weight, R [8.314 m^{3}Pa mol^{-1} K^{-1}] is the gas constant, and T [K] is the absolute temperature. To obtain the SI units of the permeance use was made of the definition Pa = kg m^{-1} s^{-2} and the identity Pa m s^2 kg^{-1} (=1) as shown below.

$$\left(\frac{1}{MRT}\right)^{0.5} = \left\{\left(\frac{mol}{kg}\right)\cdot\left(\frac{mol\,K}{m^3\,Pa}\right)\cdot\left(\frac{1}{K}\right)\cdot\left(\frac{kg}{Pa\,m\,s^2}\right)\right\}^{0.5} = mol\,m^{-2}\,s^{-2}\,Pa^{-1}$$

When the width of the pores is smaller, so that the molecules interact with the potential field of the surface of the pores, encountering an additional resistance, the permeance is described by the empirical gas-translation model [102]. This equation is obtained by adding an activation energy term and an pre-exponential factor q_g [dimensionless] to the Knudsen diffusion model (Eqn. 4.4)

$$\bar{P} = \frac{\varepsilon d_{\mathrm{p}} q_g}{\tau L}\left(\frac{8}{\pi M R T}\right)^{1/2} e^{-\frac{\Delta E}{RT}} \qquad \text{(Eqn. 4.4)}$$

In this equation the symbols are the same as in the previous equation, with ΔE being an activation barrier. When continuous pores are not present, such as in silica membranes obtained from components with easily hydrolysable bonds (e.g Si-O-C in tetraethylorthosilicate), the movement of molecules occurs by solid-state diffusion. A model involving jumps of molecules between solubility sites [103,104] explains the behavior of small gas molecules in such materials by Eqn. 4.5. Hydrogen permselective membranes have solubility sites which have slightly larger size than hydrogen molecules and these solubility sites work as sieves which separate hydrogen from larger molecules [105].

$$\bar{P} = \frac{d^2 h^2}{6L}\left(\frac{1}{2\pi k m T}\right)^{3/2}\left(\frac{\sigma h^2}{8\pi^2 I k T}\right)^{\alpha} \times \frac{N_{\mathrm{S}}}{N_{\mathrm{A}}}\frac{1}{\left(e^{h\nu^*/2kT} - e^{-h\nu^*/2kT}\right)^2} e^{-\frac{\Delta E}{RT}} \qquad \text{(Eqn. 4.5)}$$

4.3.3 Permeance Mechanisms through the Membranes

In order to ascertain the contribution of the topmost silica-alumina layer to the total permeance, the properties of the support were measured separately. The permeances through this component for different gases at various temperatures is shown in Fig. 4.7. The permeances were very high, of the order of 10^{-5} mol $m^{-2}s^{-1}Pa^{-1}$, and the permeance of each gas showed a linear dependence on the inverse square root of temperature. In addition, the slope of each line also showed a linear dependence on the inverse square root of the molecular weight of each gas species. These results give unequivocal evidence that the permeances through the intermediate layer are due to Knudsen diffusion (Eqn. 4.3)[18].

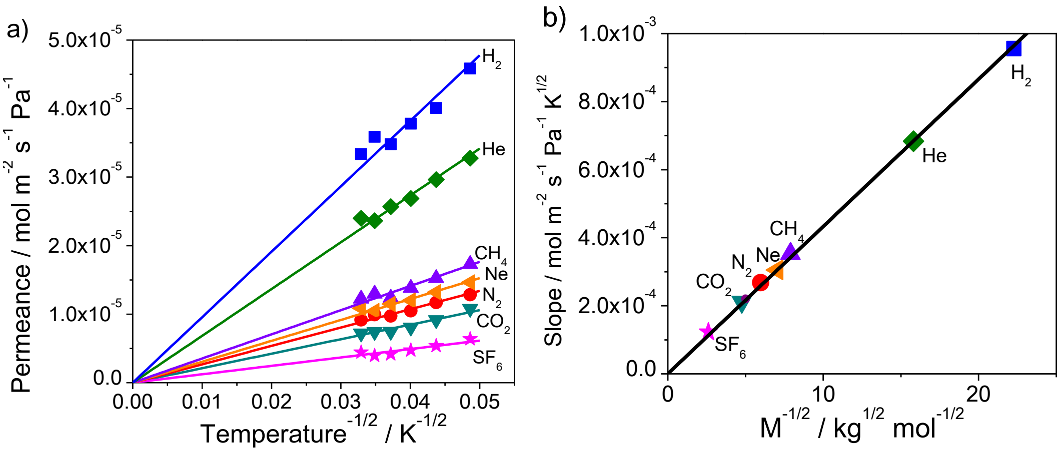

Fig. 4.7 a) Thermal dependency of the permeance of various gas species through the intermediate layer plotted versus inverse square root of temperature b) The slope of each approximation lines in a) versus inverse square root of molecular weight

The above results described the permeances through the support. Fig. 4.8 shows the permeance of seven gases between 423 and 923 K through the membrane consisting of the silica-alumina CVD layer (Al/Si = 0.03) deposited on the support. The permeances of the smaller gas species (He, Ne, H_2) are substantially higher than those of the larger gas molecules (CO_2, N_2, CH_4, SF_6). The silica-alumina composite membrane showed similar behavior as pure silica membranes [18] and silica-zirconia membranes [13]. The permeance generally dropped with the size of the permeating species (Fig. 4.8), but He, H_2 and Ne deviated markedly from this trend. The order in permeances of the smaller gases; He > H_2 > Ne did not follow either size or weight. The resistance of the support was small and the observed permeance can be attributed to the topmost silica alumina composite layer. For He, H_2 and Ne, the results were fitted with the solid-state diffusion model (Eqn. 4.5) and for CH_4, N_2, CO_2 and SF_6, the results were fitted by the gas translation model (Eqn. 4.4). The fitting curves for each model were obtained by the Lavenberg-Marquardt algorithm in Polymath and are drawn in Fig. 4.9 as dotted lines. The experimental results show excellent agreement for these models as shown by the regression coefficients (R^2).

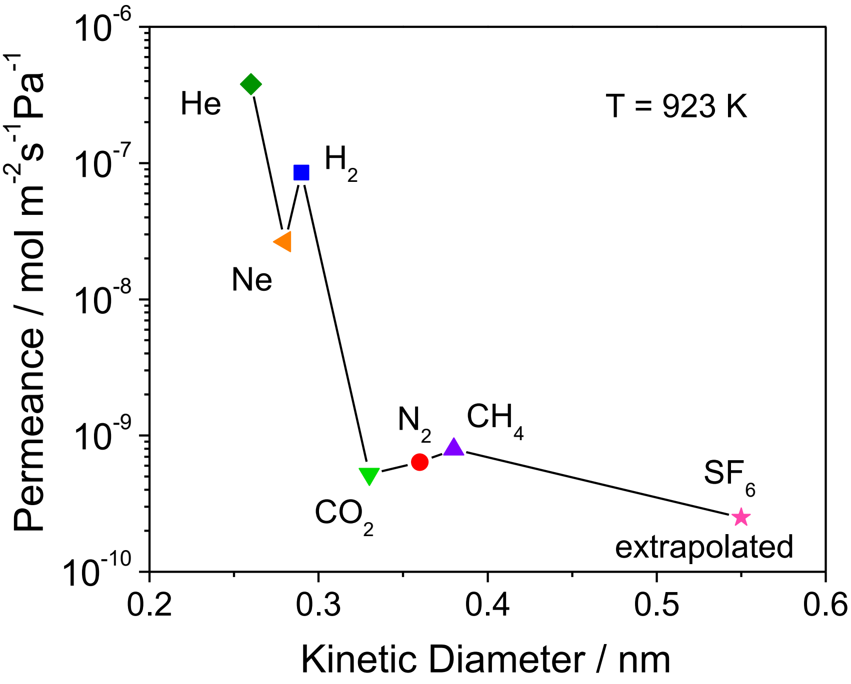

Fig. 4.8. Relationship between permeance and kinetic diameter in the silica-alumina composite membrane (Al/Si=0.03) at 923 K.

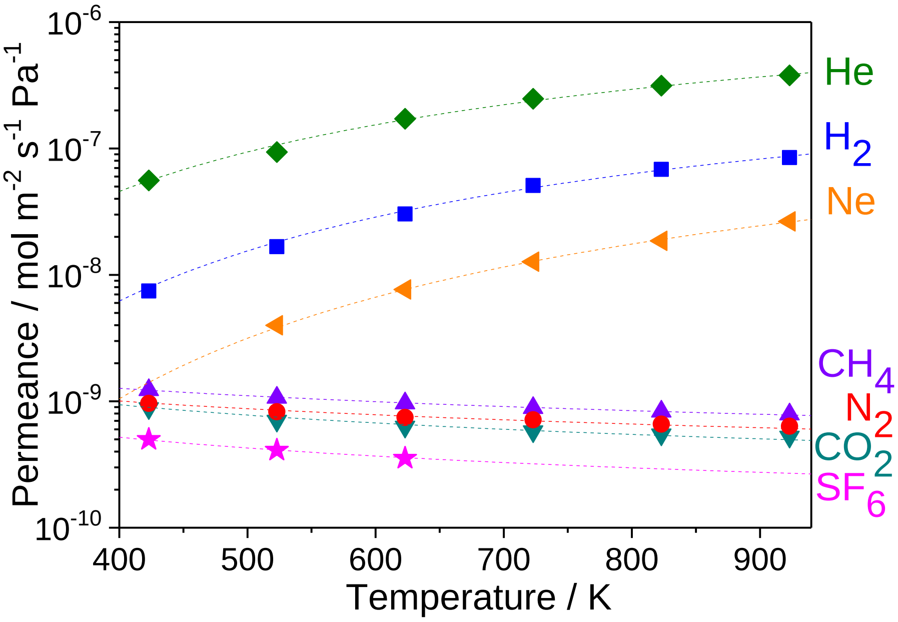

Fig. 4.9 Temperature dependency of permeances of various gas species through silica-alumina composite membranes

For the smaller gas molecules, He, H_2, and Ne, the curves connecting the points in Fig. 4.9 were obtained by the solubility site model (Eqn. 4.5). The calculated curves agree with the data very well, reproducing the details of the curvature for all three gases over the entire temperature range. The calculated parameters are shown in Table 4.1.

Table 4.1. Calculated parameters for the fitting by solid state diffusion

Species*	He (0.26 nm)	Ne (0.28 nm)	H_2 (0.29 nm)
N_s [m^{-3}]	2.18×10^{26}	1.97×10^{26}	6.82×10^{25}
v^* [s^{-1}]	3.46×10^{12}	3.19×10^{12}	4.50×10^{12}
ΔE [J mol^{-1}]	9990	12900	13900
R^2	0.999	0.998	0.996

*Kinetic diameter of species are indicated in parenthesis.

The solubility site model can explain the distinctive order of permeance among hydrogen, helium and neon (Ne < H_2 < He) which did not follow molecular size (He < Ne < H_2) nor weight (H_2 < He < Ne). The number of solubility sites (N_s) that accept each gas species decreased with increasing species size. This is reasonable since on average there will be less solubility sites that can accommodate the larger species. The order of magnitude of the site density of 10^{26} m^{-3} is physically realistic, as the inverse cube root of the order of nm, which corresponds to a reasonable average distance between sites. The activation energy (ΔE) also increased with species size. This is also reasonable, as the larger species will encounter a greater barrier in passing through the windows between the solubility sites. The activation energies are relatively small, but are physically realistic since they are larger than those reported for passage of He [106,107], Ne [108,109], and H_2 [110,111] through vitreous glasses and quartz, which are denser forms of silica. The vibrational frequency in jumping between sorption sites (ν*) was inversely proportional to molecular weight, being largest for the lightest species, H_2, and smallest for the heaviest species, Ne. This is also physically realistic since heavier molecules naturally have a lower vibrational frequency, as seen for example for the vibrational frequency, ν, of a harmonic oscillator, $\nu = \frac{1}{2\pi}\sqrt{\frac{k}{M}}$, which is inversely proportional to the square root of the mass, M. Thus, the observed order of permeance for the smaller gas species (Ne < H_2 < He) can be explained as a result of the contributions of factors depending on the size and weight of the species as given by the solubility site model (Eqn. 4.5).

According to Barrer et al., the structure of silica is made up of 5-, 6-, 7-, and 8- membered rings made of Si-O linkages [112], and these form the solubility sites. The size of the average solubility sites is close to 0.3 nm and so readily accommodate He (kinetic diameter 0.26 nm), Ne (0.28 nm), and H_2 (0.29 nm) while species like CO_2 (kinetic diameter 0.33 nm), N_2 (0.36 nm), CO (0.38 nm), CH_4 (0.38 nm), and SF_6 (0.55 nm) do not fit and are excluded [104]. This explains the low permeance of the larger gases through silica membranes.

The permeances of the larger gases showed a negative dependence on temperature as was observed in the permeance through the intermediate layer. To verify whether the permeance occurred through the Knudsen mechanism, the permeance of each large molecule through the silica-alumina composite membrane was plotted versus the inverse square root of temperature (Fig. 4.10). In contrast to Fig. 4.7a, the permeances did not show a linear relation extrapolating to zero at 0 K and this gave strong evidence that the transport of these molecules did not take place by Knudsen diffusion. Further evidence for the lack of Knudsen diffusion is that the permeances do not extrapolate to the origin when plotted versus the inverse square root of the mass, as it should according to Eqn. 4.3.

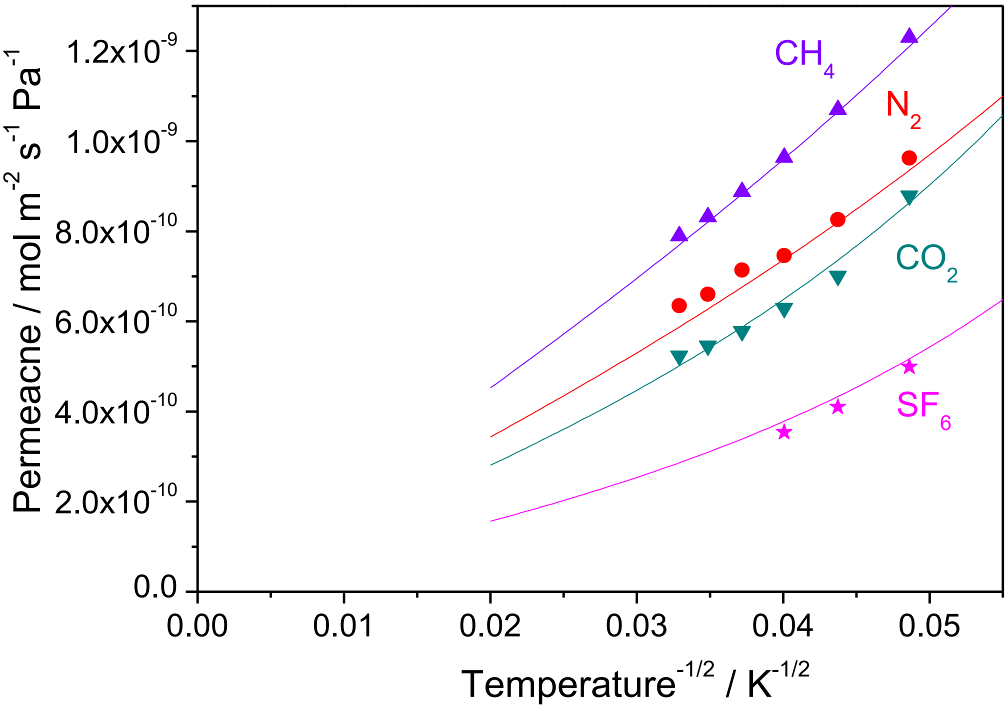

Fig. 4.10 Permeation change of large molecules plotted versus square root inverse of absolute temperature: The curves show fits to the gas translation model (Eqn.4.4)

The permeances of the larger gas species, CH_4, N_2, CO_2, and SF_6, were fit to the gas translation model (Eqn. 4.4) and the obtained fitting parameters are shown in Table 4.2. The equation is shown in abridged form in Eqn. 4.6, with a constant $\mathrm{C} = \frac{\varepsilon d_p q_g}{\tau L}$ [dimensionless].

$$\bar{P} = C\left(\frac{8}{\pi MRT}\right)^{1/2} e^{-\frac{\Delta E}{RT}} \qquad \text{(Eqn. 4.6)}$$

Table 4.2. Calculated parameters for the gas translation model

	CH_4	N_2	CO_2	SF_6
Kinetic diameter [nm]	0.38	0.36	0.33	0.55
Mass [au]	16	28	44	146
C [dimensionless]	5.25×10^{-9}	5.34×10^{-9}	5.13×10^{-9}	4.87×10^{-9}
ΔE [J mol^{-1}]	-288	-367	-965	-1300
R^2 (individual A's)	0.996	0.996	0.996	0.999
R^2 ($\bar{C}$ = 5.15x10^{-9})	0.980	0.978	0.996	0.997

The regression coefficients for the individually fitted C constants are also listed in Table 4.2, and they show values close to 1.000 indicating very good fits. The calculated C constants were similar among the four species, and did not show a dependence on species size or weight (Table 4.2). Because of the similarity of the C values another fit was made taking the average value of $\bar{C}$ = 5.15x10^{-9}, and fitted curves using this value are shown in Fig. 4. 10. Good fits were obtained and the calculated R^2 values with this average value are also close to unity, although they are somewhat less than the individually fitted C values, as might be expected. Taking the permeance to be controlled by defects in the CVD layer, the value of C can be estimated using the measured thickness (L = 30 nm) and order-of-magnitude values for the unknown parameters (ε=0.5, d_p = 5 nm, q_g = 6x10^{-7}, τ=10 [113]) as follows:

$$\mathrm{C} = \frac{\varepsilon d_p q_g}{\tau L} = \frac{(0.50)(5\,nm)(6x10^{-7})}{(10)(30\,nm)} = 5 \times 10^{-9}$$

This is close to the average experimental value of $\bar{C}$ = 5.15x10^{-9}. Previously reported pure silica membranes prepared by CVD [18] and sol-gel methods [114] gave similar values of C as well as negative activation energies. Thus, the permeance of the larger species CH_4, N_2, CO_2, and SF_6 follows the gas translational model, which can be viewed as a combination of Knudsen diffusion and surface diffusion.

The reason the apparent activation energies are small in magnitude and negative is because $\Delta E_j = h_j + u_j$, where h_i is the depth of the well and u_j is the hopping energy [115]. The adsorption process is exothermic and hence h_j is negative, but u_j is positive. In essence, while the species are in the potential of the surface their motion is akin to surface diffusion.

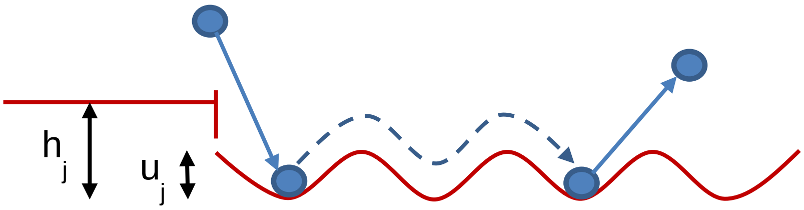

Figure 4.11. Schematic of Gas Translational Model. The heat of adsorption h_j is negative while the the hopping energy u_j is positive, so that $\Delta E_j = h_j - u_j$ is a negative quantity.

4.3.4 Hydrothermal Stability

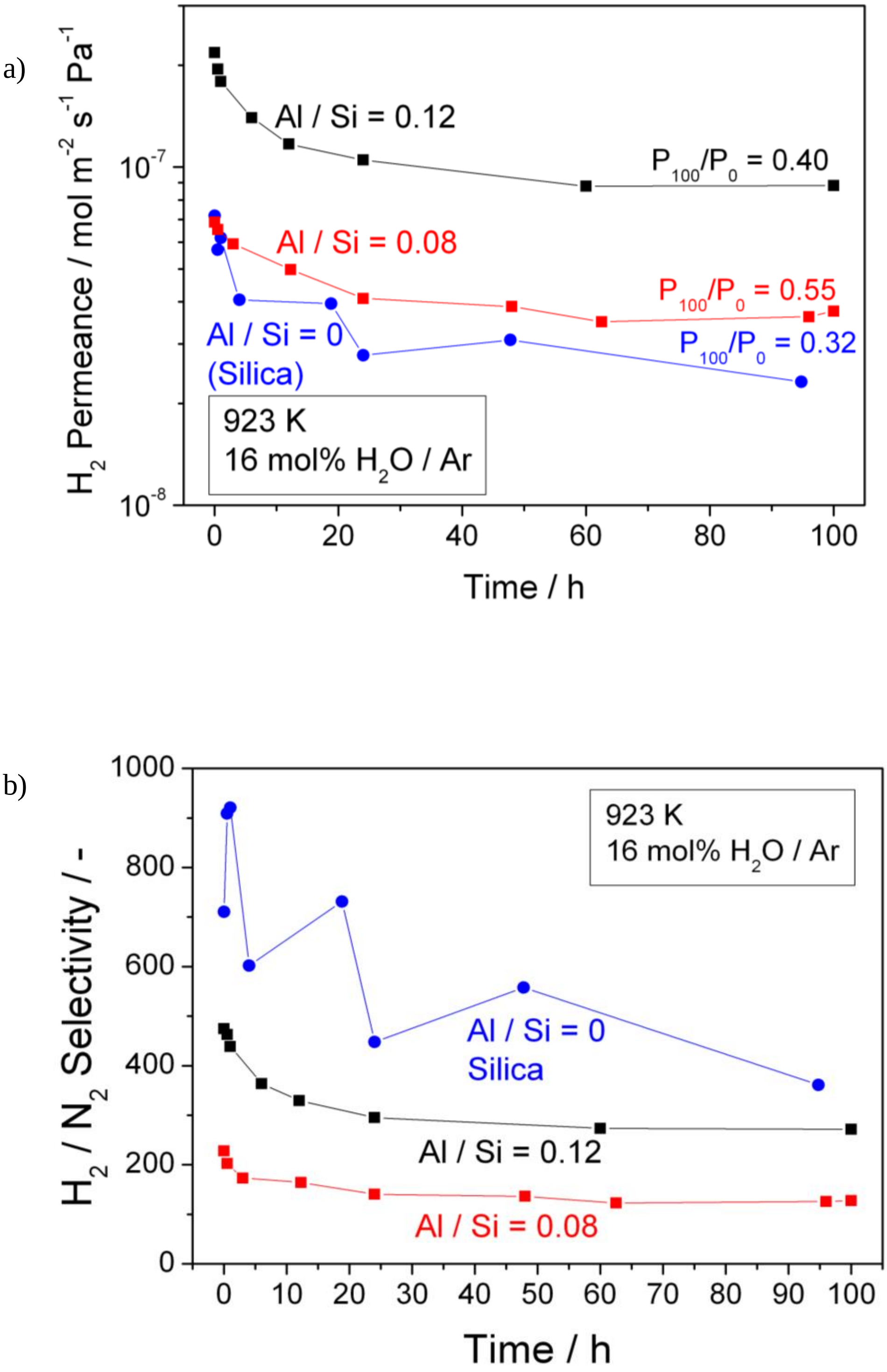

Fig. 4.12 a) H_2 permeance change and b) H_2/N_2 selectivity change under hydrothermal environment

Fig. 4.12 shows the changes in the permeance of hydrogen versus time at hydrothermal conditions for the silica and silica-alumina composite membranes. The silica membrane (Al/Si = 0) shows considerable variability in hydrogen selectivity, while the silica-alumina composite membranes reach stable values with selectivity higher than 100. The silica membrane lost more than 60% of its initial hydrogen permeance, while the silica-alumina membranes lost a smaller proportion of their hydrogen permeance. Compared to hydrogen, the permeance of nitrogen seems to be much less effected by hydrothermal treatment, and therefore the selectivity drop curve looks similar to the permeance drop curve. This indicates that large pore defects through which the nitrogen passes are not affected much by steam. Overall, the silica-alumina composite membrane showed higher hydrothermal stability than the silica membrane.

In membrane reactor operation, hydrogen permeance contributes more to the reaction rate compared to hydrogen selectivity [116] as long as the selectivity is acceptable. The silica-alumina composite membrane with 0.12 Al/Si ratio was deemed to be optimal for usage in membrane reactors operated under hydrothermal conditions because of its high hydrogen permeance and sufficient H_2/N_2 selectivity.

4.3.5. Membrane Reactor

The membrane reactor was operated for the steam methane reforming with the silica-alumina composite membranes (Al/Si = 0.12). After 120 min of CVD, the hydrogen permeance was 4.9×10^{-7} mol m^{-2} s^{-1} Pa^{-1}, the nitrogen permeance was 9.7×10^{-10} mol m^{-2} s^{-1} Pa^{-1} and the H_2/N_2 selectivity was 500. The reactants methane and steam diluted by nitrogen were fed to the catalyst bed placed in the outer shell side of the membrane. The reaction was operated at 923 K and a total pressure of 0.40 MPa. The flow rate of methane was fixed at 3.5 μmol s^{-1} (5.0 cm^3 (NTP) min^{-1}) and the total flow rate was fixed at 35 μmol s^{-1} (50 cm^3 (NTP) min^{-1}). The sweep flow of nitrogen in the tube side was 69 μmol s^{-1} (100 cm^3 (NTP) min^{-1}). The results of steam methane reforming in the membrane reactor and the packed bed reactor are shown in Fig.4.13. The retentate H_2 flow in Fig. 4.13 indicates the hydrogen molar flow in the shell side of the membrane, while the total H_2 flow means the total hydrogen molar flow on both sides of the membrane. Thus the difference between the retentate H_2 flow and the total H_2 flow is the permeate flow of hydrogen. The membrane reactor showed higher methane conversion and hydrogen production compared to the packed bed reactor. The hydrothermal stability of the membrane was monitored during the reactor experiments by measuring the hydrogen partial pressure. The experiments lasted 60 h, and the permeance dropped slightly in the beginning, and then stabilized.

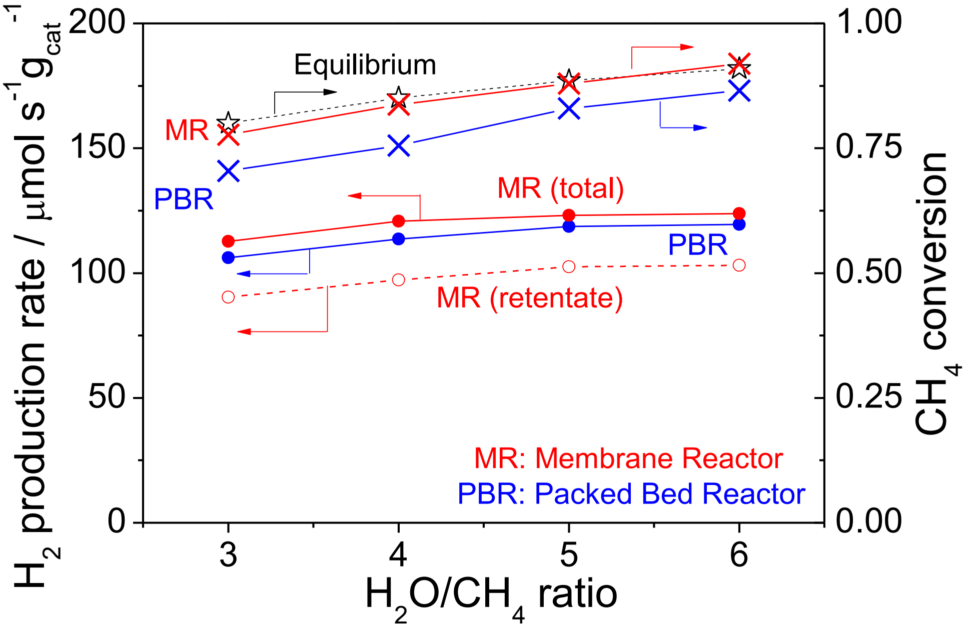

Fig. 4.13. The CH_4 conversion and H_2 production rate in steam methane reforming at 923 K and 0.40 MPa with WHSV of 3000 Ncm^3 g_{cat}^{-1} h^{-1} . red: membrane reactor, blue: packed bed reactor

The results here for the hydrogen permeance are similar to those reported earlier by Hacarlioglu et al. [117], but the conditions were different. The rate and conversion enhancements are moderate compared to those obtained with a PdRu membrane [64], probably because the latter had higher permeance (0.0027 mol $m^{-2}s^{-1}Pa^{-0.5}$) and was operated at a higher pressure. Nevertheless, the membrane is shown to be adequate for hydrogen production.

4.4. Conclusions

Hydrothermally stable silica-alumina composite membranes were successfully synthesized on supports with $\gamma-$alumina intermediate layers using a chemical vapor deposition method with aluminum tri-sec-butoxide and tetraethylorthosilicate. The silica-alumina composite membranes showed higher hydrothermal stability compared to a silica membrane after 100 h of hydrothermal treatment under 16 mol% H_2O at 923 K. After 60 h of hydrothermal treatment, the silica-alumina composite membranes were stable under high temperature and humid conditions.

The permeances of several gas species through the silica-alumina membrane (Al/Si = 0.03) at various temperatures were measured and the results was well explained by a solid-state diffusion mechanism for small gas species (H_2, He, Ne) and by an activated gas translation mechanism for large species (CH_4, CO_2, N_2, SF_6).

The silica-alumina hydrothermally stable membrane (Al/Si = 0.12) was applied to a membrane reactor for steam methane reforming. Comparing the membrane reactor operation with packed bed mode, the membranes were effective in extracting hydrogen selectively from the reaction zone and gave enhanced hydrogen yield and methane conversion.

Chapter 5. Overcoming pressure drop losses in membrane reactors by semi-batch operation

N. Kageyama, P. Hacarlioglu, A. Takagaki, R. Kikuchi, S.T. Oyama, Separation and Purification Technology, 185, 175-185 (2017)

The feasibility of harnessing the increase in moles in certain equilibrium-limited reactions to alleviate the pressure driving force requirement for permeation through membranes is demonstrated. The studies are conducted in a packed-bed membrane reactor operated as a semi-batch membrane reactor (SBMR) to capture the pressure generating potential of the reaction. The actual system investigated is the steam methane reforming carried out at various temperatures (873 K and 923 K) and pressures (0.5- 1.5 MPa) with a $Ni/MgAl_2O_4$ catalyst. A silica-alumina membrane with a hydrogen permeance of 2.2×10^{-7} mol m^{-2} s^{-1} Pa^{-1} at 923 K prepared by chemical vapor deposition was used in the membrane reactor. The hydrogen productivities obtained in the SBMR were compared with the productivities obtained in a membrane reactor operated at the same conditions. At low pressures (0.5, 1.0 MPa) the hydrogen productivities of the SBMR were comparable values to those obtained with the continuous membrane reactor, but at high pressure (1.5 MPa) the SBMR showed superior performance. One-dimensional modeling studies gave good agreement between simulated and experimental results obtained from both reactor types. Based on these calculations,

further estimations on hydrogen productivities were made at high pressures. These results indicated that the SBMR improved the hydrogen production when the steam methane reforming was conducted above 1.5 MPa. The SBMR described here could be utilized in a system where multiple units would be arranged to undertake parallel filling and discharge operations, much akin to the arrangement used in a pressure swing adsorption system.

5.1 Introduction

Catalytic membrane reactors have attracted much attention because of their ability to simultaneously carry out reaction and mass transfer into and out of the reaction zone and they have been discussed in numerous books [118,119,120,121,122], reviews [123,124,73], and journal articles [125,126,127,128]. When mass transfer occurs into the reaction zone the membrane reactor is said to operate as a distributor [128] or contactor [125] and when it occurs out of the reaction zone it is said to operate as a separator [129]. The distributor mode of operation is usually applied in cases where mixing of the reactants is in some way critical, for example when mixing an oxidant and a reductant such as in the partial oxidation of methane to syngas [130,131]. An earlier study of the epoxidation of propylene [132] showed that it was possible to safely operate in the explosive regime. The contactor mode of operation is applied when it is important to ensure that all of a reactant stream enters into contact with the reaction zone, for example, when treating a pollutant flow [133]. The separator mode of operation is utilized when a membrane exists that can selectively remove or separate a product of an equilibrium limited reaction. According to the Le-Chatelier-Brown's law this shifts the equilibrium to the product side and enhances yields. A common application is in the production of hydrogen from dehydrogenation [134, 135], steam methane reforming [136, 137, 138, 139, 140] or dry reforming of methane [141]. In many reactors with separator membranes, inert sweep gas is used in the permeate side to attain a sufficient partial pressure difference [136, 137]. The sweep gas can be steam for easy separation by condensation [142, 143], although the use of pressure can be employed to avoid the use of any sweep gas [144].

A drawback of membranes is that they require a partial pressure gradient to drive the passage of a species and there is a substantial cost in producing this gradient. Although not generally appreciated, compression is one of the most expensive unit operations [145, 146] because of the high energy required to increase the pressure of a gas, as given by the equation

$$W_c = \frac{1}{\eta} RTF \left[\frac{\gamma}{\gamma-1}\right] \left[\left(\frac{P_h}{P_l}\right)^{\frac{\gamma}{\gamma-1}} - 1\right] \qquad \text{(Eq. 5.1)}$$

where η is the efficiency, R is the gas constant, T is the temperature, F is the molar flow, γ is the ratio of heat capacities at constant pressure and volume ($= C_p/C_v$) and P_h and P_l are high and low pressures. For example for methane $\gamma = 1.3$ [147], so $\gamma/(\gamma-1) = 4.3$, a large factor and exponent.

The objective of this study is to explore means of alleviating the requirement of the pressure gradient in membrane reactors for a certain class of chemical reactions. Attention will be focused on the case of the separator mode of operation. In the case of the distributor or contactor modes, reaction consumes reactants decreasing their partial pressure and naturally increases the driving force for mass transfer. The class of reactions that will be considered in the separator mode will be that in which there is a net increase in the number of moles. This is a common situation, as exemplified for technologically important hydrogen-producing reactions (Table 5.1).

Table 5.1 Mole increase seen in hydrogen producing reactions

Type	Reaction	Increase in moles
Dehydrogenation	$C_2H_6 \rightarrow C_2H_4 + H_2$	2
Aromatization	$6CH_4 \rightarrow C_6H_6 + 9H_2$	5/3
Steam reforming	$CH_4 + H_2O \rightarrow CO + 3H_2$	2
Dry reforming	$CH_4 + CO_2 \rightarrow 2CO + 2H_2$	2
Ethanol reforming	$C_2H_5OH + 3H_2O \rightarrow 2\ CO_2 + 6H_2$	2

The increase in moles offers the potential of utilizing the reaction itself to overcome pressure drop losses through the membrane. This can be accomplished by throttling the flow through the reactor so that the pressure losses due to the removal of a species by permeation are partly offset by the increase in moles due to the reaction. In all studies reported so far that we are aware of the reactants and products have been allowed to freely exit the reactor, with the increase in moles simply resulting in an increase in flow rate out of the reactor.

In this study the throttling process, where the flow is restricted, is applied at the limit of zero flow for demonstration of the concept. In this case the membrane reactor is operated as a semi-batch membrane reactor (SBMR). It is shown experimentally and theoretically that higher hydrogen productivities are obtained with a SBMR as compared to a continuous reactor. The reaction considered is the methane steam reforming (MSR) reaction (1), which is accompanied by the water-gas shift (WGS) reaction (2). The methane reforming to CO_2 reaction (3) is also considered for a full description of the kinetics, as will be explained later.

$$CH_4 + H_2O \rightleftarrows CO + 3H_2 \qquad \Delta H^0_{298} = 206 \text{ kJ/mol} \qquad (2)$$

$$CO + H_2O \rightleftarrows CO_2 + H_2 \qquad \Delta H^0_{298} = \text{-}41 \text{ kJ/mol} \qquad (3)$$

$$CH_4 + 2H_2O \rightleftarrows CO_2 + 4H_2 \qquad \Delta H^0_{298} = 165 \text{ kJ/mol} \qquad (4)$$

The reforming reactions are endothermic (1,3) and take place simultaneously with the exothermic water-gas shift (WGS) reaction (2). Commercially, the methane steam reforming is performed in a multi-tube reactor with a nickel based catalyst at a pressure range of 0.8 to 3.5 MPa and a temperature range of 1073-1273 K [148]. A typical industrial process consists of three units, a steam methane reformer, a water-gas shift reactor to enhance CO conversion and a pressure swing adsorption (PSA) system or a cryogenic distillation system as a purification unit. Under these conditions the conversion of methane obtained in an industrial plant is about 80% and is limited by the thermodynamic equilibrium.

The application of membranes in batch systems has been employed in biochemical applications in the liquid phase, especially using bacteria. In most cases, the membrane was used to immobilize the bacteria in a stream of reactants. However, in some studies use was made of the membrane as a separator [149]. Membrane applications in batch systems were also reported in liquid phase reactions utilizing the hydrophobicity or hydrophilicity of the material for enhancing desired hydroxylation [150] in pervaporation for dewatering applications [151] and pervaporation membrane reactors for chemical synthesis [152]. However, those studies focused on changes in the concentrations of reactants or products with pressure held constant. In the present study, pressure is auto-generated by conducting a gas-phase reaction with an increase in moles in a reactor where the exit is throttled to gain pressure. This is important because pressure is the significant driving force in gaseous membrane separations.

5.2 Experimental

5.2.1. Preparation

Ni/$MgAl_2O_4$ Catalyst

A commercial Ni/$MgAl_2O_4$ catalyst (NG-610-6H) provided by Unicat Catalysts was used throughout the study. The original catalyst was crushed and sieved to sizes of 0.1-0.3 mm. The catalyst was reduced in flowing hydrogen at 923 K for 2 h before use.

Characterization of Ni/$MgAl_2O_4$ catalysts

The BET surface area was obtained from nitrogen adsorption measurements carried out in a volumetric adsorption unit (Micromeritics, ASAP 2010). The catalyst sample was degassed at 393 K in vacuum prior to the measurements. The CO uptake of the catalyst was determined after reduction in 75 μmol s^{-1} (110 cm^3 (NTP) min^{-1}) of hydrogen at 823 K for 2 h in a flow system. Pulses of CO were injected into a He carrier stream at room temperature and the intensity of the CO signal (m/e = 28) was monitored with a mass spectrometer (Dycor/ Ametek Model MA100). The injection of CO was continued until saturation of the sample surface was observed.

Hydrogen selective silica-alumina membranes

The ceramic membranes used in this study were prepared by chemical vapor deposition (CVD) of a thin layer of silica-alumina on a porous alumina support at 923 K. The support was a commercial multilayered porous alumina support (Pall Corporation Part No. S700-0011) of tubular geometry (o.d. = 10 mm, i.d. = 7 mm) with a 5 nm inner pore size. An 8.0 cm long section of this support was connected at both ends to solid alumina tubes by gas tight glass seals obtained by thermal treatment of a glass glaze (Duncan, IN, Part No. 1001) at 1153 K. Then the membrane was dip-coated in a 0.05 M dispersion of boehmite sol for 10 s and dried at room temperature for 24 h and calcined first at 973 K for 6 h and then at 923 K for 2 h. The boehmite sol was prepared by hydrolysis and acid treatment of aluminum tri-sec-butoxide as described in detail in previous studies [153,154].

The CVD process was carried out by placing the tube concentrically in a tubular quartz reactor (o.d. = 14 mm) using Swagelok fittings equipped with Teflon ferrules and then installing the reactor vertically in a split tube furnace (Fig. 5.1). Argon flow was introduced on both the shell side and the tube side of the reactor after which it was heated to 923 K with a ramp of 1 K/ min. The hydrogen selective layer was obtained by the simultaneous deposition of tetraethylorthosilicate (TEOS, Aldrich, 98%) and aluminum-tri-sec-butoxide (ATSB, Aldrich, 97%) in the inner side of the membrane at 923 K. The TEOS concentration was set to 1.94×10^{-2} mol m^{-3} by flowing argon gas through a bubbler which was kept at 298 K and the ATSB concentration was set to 5.82×10^{-4} mol m^{-3} in a similar manner except that the bubbler was kept at 363 K in an oil bath. All the carrier and dilute gas flows were adjusted by mass flow controllers (Brooks model 5850 E). The permeance of gases (H_2, CH_4, CO, CO_2) were measured at regular intervals and the ideal selectivity of hydrogen over other gases was calculated from the ratio of the single-gas permeances. The deposition process was continued until the hydrogen permeance through the membrane reached a value of 2.2 $\times 10^{-7}$ mol m^{-2} s^{-1} Pa^{-1} at 923 K.

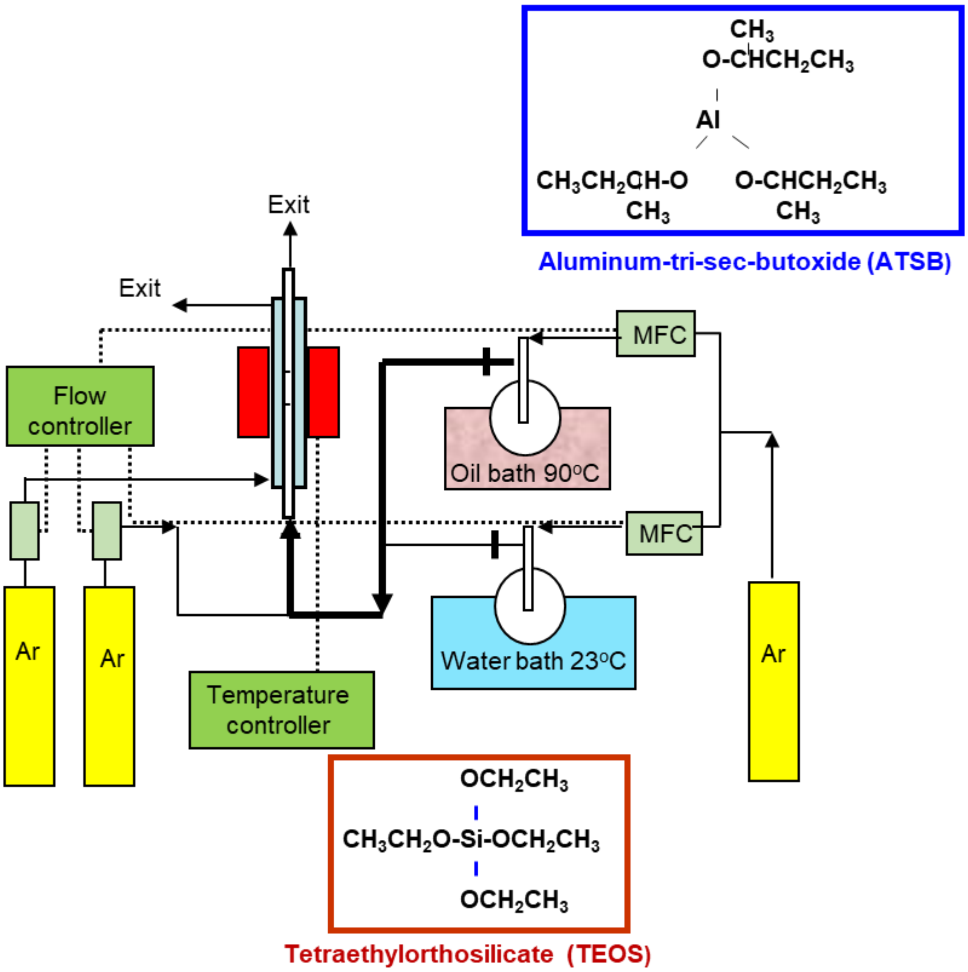

Fig.1. Schematic diagram of the CVD system for membrane synthesis

MFC: Mass Flow Controller

5.2.2. Steam methane reforming in a batch membrane reactor

The packed-bed catalytic membrane reactor consisted of a stainless steel outer shell, a quartz liner and the membrane tube assembled concentrically with O-rings and was specifically designed to withstand high pressures (Fig. 5.2). The overall length of the 1.0 cm OD membrane tube was 43 cm and it had a permeable section of length 8.0 cm in the center. The reactant gases were fed in a down flow direction to the shell side of the reactor where the catalyst bed was placed with the pressure controlled by a back pressure regulator (BPR) at the exit of the shell side. A quantity of 4.0 g of the $Ni/MgAl_2O_4$ catalyst was mixed with 4.0 g of inert quartz chips of the same size to make up a catalyst bed of 8.0 cm length and 6.0 cm^3 volume to match the length of the membrane zone. The catalyst bed was located in the annular section between the membrane and the quartz liner. The liner was used to minimize contact of the reactive flow with the stainless steel walls, which in previous studies was found to promote carbon formation [155]. There was no flow in the very thin outer region between the liner and the stainless steel walls, but the pressure in that region was equalized to the reactor pressure through an opening at the bottom of the liner to avoid stresses on the quartz material. The permeated gases were swept away in up flow mode to gain the benefit of countercurrent flow. A separate back pressure regulator was used to adjust the pressure in the tube side. The catalyst bed consisted of catalyst pellets diluted with quartz chips of the same size and was held in place by quartz wall. It occupied the volume just opposite the membrane section of the inner tube. The whole assembly was installed in an electric furnace. The reactor could also be used as a conventional packed-bed reactor by replacing the inner membrane tube with an impermeable quartz tube. This maintained the annular geometry, and permitted direct comparison between the two reactors.

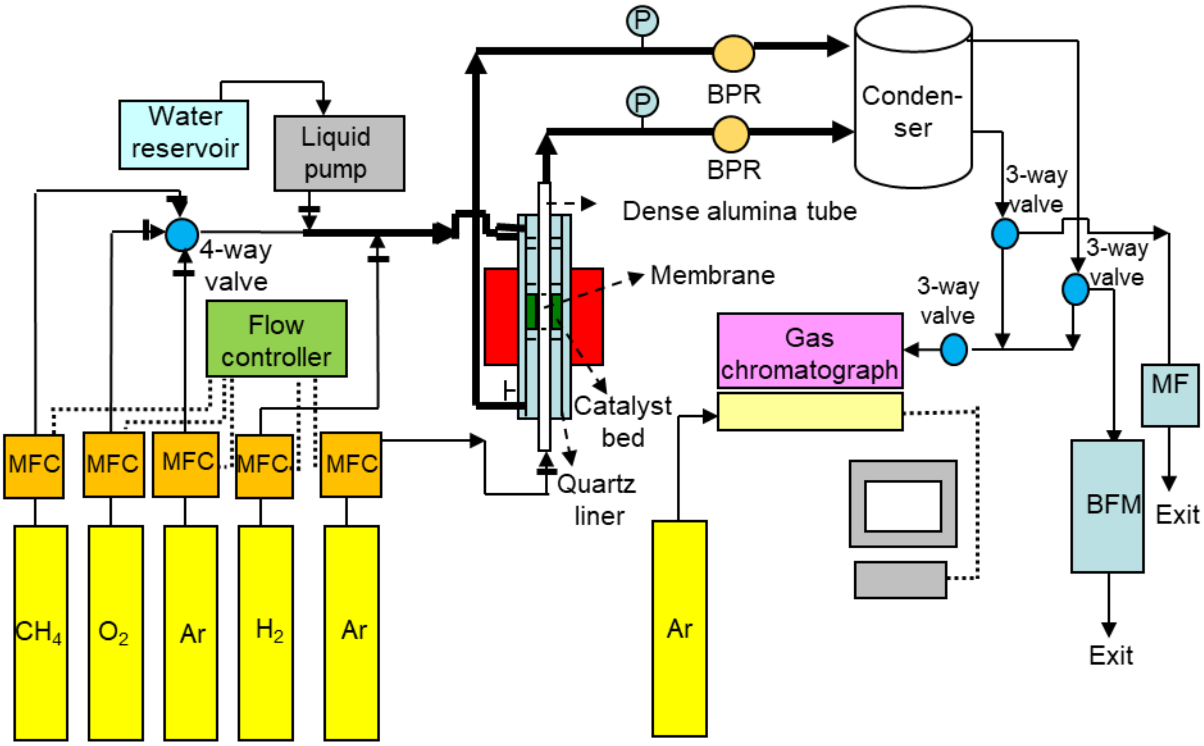

Fig. 5.2. Schematic diagram of the methane steam reforming reactor system MFC: mass flow controller, BFM: bubble flow meter, MF: mass flow meter, BPR: back pressure regulator

The steam methane reforming was carried out at two different temperatures (873, 923 K) and various pressures (0.5-1.5 MPa) with steam and methane in a 3 to 1 ratio. The overall flow rate of the reactants was increased proportionally to the pressure to keep the residence time constant. The reactant flow rates are tabulated in Table 5.2. To activate the catalyst, the temperature was raised to the catalyst reduction temperature (923 K) with a ramping rate of 0.016 K s^{-1} (1 K min^{-1}) in an argon flow of 90 μmol s^{-1} (135 cm^3 (NTP) min^{-1}) through the shell side of the reactor after which the flow was switched to hydrogen at the same flow rate for 2 h. To carry out the reaction, the temperature and pressure were adjusted, and the flow of hydrogen was replaced with a flow of methane and steam. Hydrogen was introduced to the tube side to have pure hydrogen flow. Both of the streams passed through a condenser unit which was cooled by ice to remove water vapor before injection of samples into a carbosphere packed column (o.d.: 3.175 mm, L: 1.900×10^3 mm). An online gas chromatograph (SRI 8610) equipped with a thermal conductivity detector was used to determine the compositions of the streams (H_2, CH_4, CO, CO_2). A bubble flow meter was used to determine the flow rates of the shell side and a mass flow meter to determine the hydrogen flow in the tube side of the reactor.

The semi-batch, packed-bed catalytic membrane reactor configuration was obtained by using the same reactor set-up. The reactant gases were fed to the shell side of the reactor where the catalyst was loaded and the pressure in the reactor was adjusted to a predetermined value by using a back pressure regulator at the exit of the shell side. Another back pressure regulator was placed at the exit of the tube side of the reactor to adjust the pressure in the tube side. The pressure was set to a value of 0.2 MPa in the tube side of the reactor. After adjusting the pressure in both sides of the reactor, the entrance and the exit of the shell side and the entrance of the tube side were closed simultaneously by using on-off valves placed at the entrance and the exit of both shell and tube sides. The hydrogen flow from the tube side of the membrane reactor was recorded by a mass flow meter and the pressure in the shell and tube sides monitored at the same time.

Table 5.2. Inlet flow rates of reactants

Pressure (MPa)	Volumetric flow rate of CH_4 (cm^3 (NTP) min^{-1})	Volumetric flow rate of H_2O (cm^3 (NTP) min^{-1})
0.5	25	75
1.0	50	150
1.5	75	225

5.2.3. Numerical simulation of the semi-batch membrane reactor

In this study the kinetics of the methane steam reforming and water-gas shift reactions determined by Xu and Froment [22] were utilized because they cover a wide range of conditions. The kinetics were developed for the same catalyst composition, $Ni/MgAl_2O_4$, as used in this study. The reactions considered are the three reactions listed in the introduction, the reforming reaction to form

CO (Equation 5.1), the water-gas shift (WGS) reaction (Equation 5.2), and the reforming reaction to form CO_2 (Equation 5.3).

The rate expressions for the reactions of Equations 5.1-3 are given in Table 5.3. In order to apply these equations, hydrogen should be present in the feed stream to make the initial rate of methane conversion finite. Thus an initial value of 10^{-5} for P_{H2} /P_{CH4} was chosen in the present kinetic model. The expressions for the reaction rates and the equilibrium constants at various temperatures (873 K, 923 K) used in these expressions are given in Table 3. The reaction rate constants and the adsorption constants are also tabulated in Table 5.4 and 5.

Table 5.3. Reaction rate expressions and equilibrium constant of the reactions

Reaction rates:

$$r_1 = \frac{\frac{k_1}{P_{H_2}^{2.5}}\left[P_{CO}P_{H_2O} - \frac{P_{H_2}^3 P_{CO}}{K_{eq1}}\right]}{DEN^2}$$

$$r_2 = \frac{\frac{k_2}{P_{H_2}}\left[P_{CO}P_{H_2O} - \frac{P_{H_2} P_{CO_2}}{K_{eq2}}\right]}{DEN^2}$$

$$r_3 = \frac{\frac{k_3}{P_{H_2}^{3.5}}\left[P_{CH_4}P_{H_2O}^2 - \frac{P_{H_2}^4 P_{CO_2}}{K_{eq3}}\right]}{DEN^2}$$

$$DEN = 1 + K_{CO}P_{CO} + K_{H_2}P_{H_2} + K_{CH_4}P_{CH_4} + K_{H_2O}\frac{P_{H_2O}}{P_{H_2}}$$

Equilibrium constants:

Temperature (K)	K_{eq1}	K_{eq2}	K_{eq3}
873	0.498	2.53	1.26
923	2.65	1.93	5.12

Table 5.4. Reaction rate constants

Reaction rate constants:

$$k_i = A_i \cdot exp\left(\frac{-E_i}{RT}\right) \qquad i = 1, 2, 3$$

Reaction	A_i	E_i (kJ mol^{-1})
1	3.70×10^{14} mol Pa$^{0.5}$ g$_{cat}^{-1}$ s^{-1}	240
2	1.72×10^{5} mol Pa^{-1} g$_{cat}^{-1}$ s^{-1}	67.1
3	8.95×10^{13} mol Pa$^{0.5}$ g$_{cat}^{-1}$ s^{-1}	244

Table 5.5. Adsorption constants

Adsorption constants:

$$K_j = B_j \cdot exp\left(\frac{-\Delta H_j}{RT}\right) \qquad j = CO, H_2, CH_4, H_2O$$

Species	B_j	ΔH_j (kJ mol^{-1})
CO	8.23×10^{-10} Pa^{-1}	-70.7
H_2	6.12×10^{-14} Pa^{-1}	-82.9
CH_4	6.65×10^{-9} Pa^{-1}	-38.3
H_2O	1.77	88.7

Steady-state conditions and plug flow were assumed on both the reaction and permeation sides. Negligible pressure drop along the axial direction and an isothermal reaction were also presumed in this model. Fig. 3 shows the schematic reaction model used for the simulation of the continuous membrane reactor.

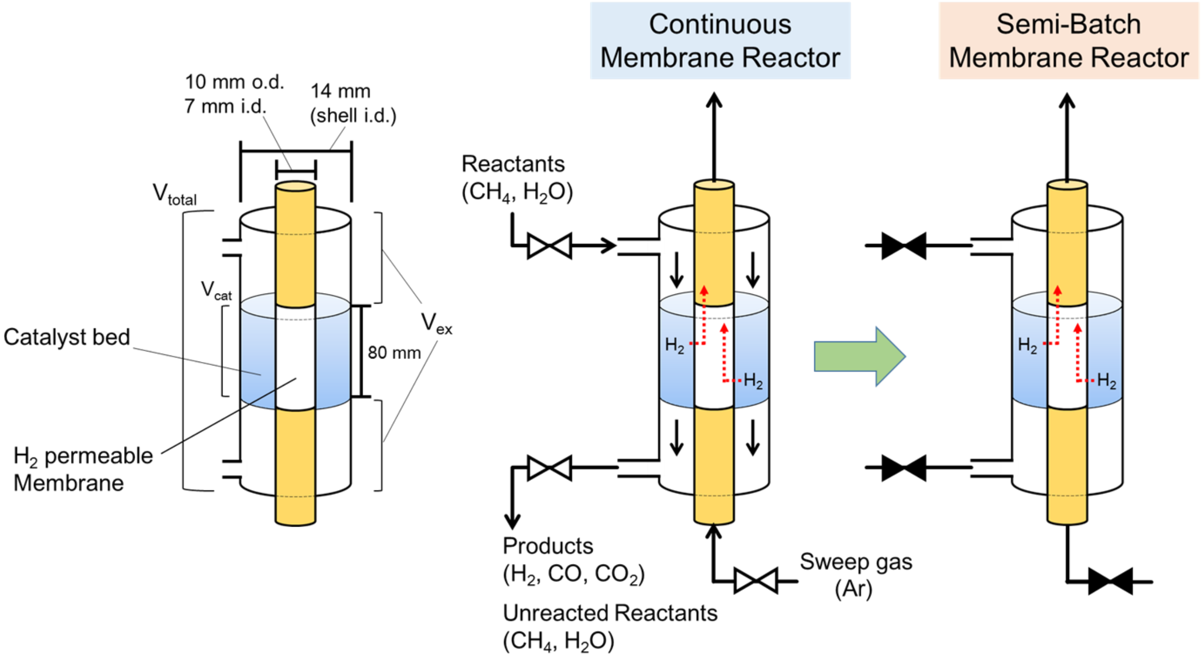

Fig. 5.3. The reactor configuration (left) and schematic diagram of the membrane reactor operated in continuous (middle) and semi-batch (right) modes.

5.2.4. Continuous flow reactor

Molar flow rates of the species in the shell and tube sides are described as follows in a membrane reactor:

Shell side:

$$\frac{\mathrm{d}F_{\mathrm{j}}}{\mathrm{d}w} = \sum_{\mathrm{i}=1,2,3} \alpha_{\mathrm{i,j}} R_{\mathrm{i}} - R_{\mathrm{jp}} \qquad \text{(Eqn. 5.5)}$$

Tube side:

$$\frac{\mathrm{d}F_{\mathrm{j}}}{\mathrm{d}w} = R_{\mathrm{jp}} \qquad \text{(Eqn. 5.6)}$$

where $R_{\mathrm{jp}} = \overline{P_j} \frac{da}{dw} \left(P_{\mathrm{jf}} - P_{\mathrm{jp}}\right)$ (Eqn.5.7)

In these equations 5.5-7 the subscript *i* represents the reaction and the subscript *j* represents each chemical species. F_{j} is the molar flow rate of the species, *w* is the weight of the catalyst, $\alpha_{\mathrm{i,j}}$ is the stoichiometric ratio of *j* in the reaction of i, R_{i} is the reaction rate of reaction i, R_{jp} is the permeation rate of j, $\overline{P_j}$ is the permeation rate of *j*, *a* is the membrane area, P_{jf} and P_{jp} are the partial pressure of the species in the feed and the permeate streams respectively. These are one-dimensional equations that are integrated with respect to the weight of the catalyst, w, which serves as a proxy for the length of the reactor. Their use assumes that there are no radial gradients in partial pressure, an assumption that holds because of the relatively low permeance of the membranes. These one-dimensional equations were solved by using the ordinary differential equation solver in the program Polymath [156] and the flow of the reactants and products were obtained. The productivity in hydrogen formation was estimated by using equation 5.8

$$\text{Productivity (H}_2\text{)} = F_{H_2}\ \tau \qquad \text{(Eqn. 5.8)}$$

In this equation, F_{H2} is the molar flow rate of hydrogen produced and τ is the residence time (= V/ν) in the reactor, where V is the volume of the bed and ν is the volumetric flow rate at the pressure and the temperature of the reactor.

5.2.5. Semi-batch membrane reactor (SBMR)

In the semi-batch operation, there is no flow but the experimental system is non-ideal as it has considerable dead volume consisting of the reactor volume not occupied by the bed and the ancillary volumes of piping and valves, and mass transfer between the volumes needs to be accounted for to simulate its operation. In this study, this extra volume (V_{ex} [m^3]) was considered and together with the volume of the catalyst bed (V_{cat} [m^3]) gave the total system volume (V_{total} [m^3]). To make the calculation, it was assumed that the diffusion of each gas between the catalyst bed and the additional volume took place proportionally to its partial pressure difference and self-diffusion coefficient (Table 5.6). Then a proportion coefficient of k [mol m^{-2} Pa^{-1}] including diffusion area and temperature dependence of diffusion was defined to describe the mass transfer. ($F_{D,j}$: molar flow of j [mol s^{-1}], $D_{self,j}$: self-diffusion coefficient of j [m^2 s^{-1}], ΔP_j:

partial pressure difference of j [Pa] between catalyst bed and the extra volume, exV: dimensionless extra volume [-]).

$$F_{D,j} = kD_{\mathrm{self,j}}\Delta P_{\mathrm{j}} \qquad \text{(Eqn. 5.9)}$$

This k was assumed to be constant among all the gas component and temperature range of 873-923 K for the simplicity.

Table 5.6. Self-diffusion coefficient (923 K, 0.4 MPa) [157]

N_2	0.127
H_2	0.611
H_2O	0.194
CH_4	0.163
CO	0.127
CO_2	0.084

The constant exV was defined as

$$exV = \frac{V_{ex}}{V_{cat}} = \frac{V_{total} - V_{cat}}{V_{cat}} \qquad \text{(Eqn. 5.10)}$$

The mole balance for each component can be described as follows;

Shell side:

$$\frac{dN_{\mathrm{j,cat}}}{dt} = \sum_{\mathrm{i=1,2,3}} \alpha_{\mathrm{i,j}}\, R_{\mathrm{i}}\, w - R_{\mathrm{jp}} - F_{Dj} \qquad \text{(Eqn 5.11)}$$

$$\frac{dN_{\mathrm{j,ex}}}{dt} = F_{\mathrm{D,j}} \qquad \text{(Eqn 5.12)}$$

Equations to relate moles and partial pressures are as follows:

$$\frac{dP_{\mathrm{j,cat}}}{dN_{\mathrm{j,cat}}} = \frac{RT}{V_{\mathrm{cat}}} \qquad \text{(Eqn 5.13)}$$

$$\frac{dP_{\mathrm{j,ex}}}{dN_{\mathrm{j,ex}}} = \frac{RT}{V_{\mathrm{total}} - V_{\mathrm{cat}}} = \frac{V_{\mathrm{cat}}}{V_{\mathrm{total}} - V_{\mathrm{cat}}} \cdot \frac{RT}{V_{\mathrm{cat}}} = \frac{RT}{exV \cdot V_{\mathrm{cat}}} = exV^{-1} \cdot \frac{dP_{\mathrm{j,cat}}}{dN_{\mathrm{j,cat}}} \qquad \text{(Eqn 5.14)}$$

Tube side:

$$\frac{dN_{\mathrm{j}}}{dt} = R_{\mathrm{jp}} - F_{\mathrm{j}} \qquad \text{(Eqn 5.15)}$$

In these equations 5.10-15, N_j is the number of moles of the component *j* and $N_{\mathrm{j,cat}}$ is the number of moles of *j* in the catalyst bed, *R* is the gas constant, and *T* is the temperature of the reactor. The mass transfer between the catalyst bed and the extra volume was assumed to be proportional to the partial pressure difference of each component. The capacity of the extra volume was denoted *exV*.

These one-dimensional equations were also solved by using the ordinary differential equation solver in the program Polymath. The productivity in hydrogen formation in the semi-batch operation was obtained by integrating the hydrogen flow curves.

$$\text{Productivity (H}_2\text{)} = \int_{t=0}^{\infty} F_{H_2} dt \qquad \text{(Eqn. 5.16)}$$

The productivity of the continuous reactor was considered for a time period of one residence time. For comparison, the productivity of the semi-batch reactor is also taken for one residence time.

5.3. Results and Discussion

The main objective of this work was to investigate whether the productivity for hydrogen formation could be improved when a membrane reactor was operated in a semi-batch mode instead of a continuous mode. The semi-batch operation would harness the increase in moles in the hydrogen formation reaction to overcome pressure drop losses through the membrane.

The membrane used in this work consisted of a thin, dense silica-alumina layer deposited over a graded porous alumina support. Extensive work has already been reported on the preparation [158] and use [159] of this membrane, and this will not be elaborated here. The membrane was chosen because past work had shown that the addition of Al to the Si in the chemical vapor deposition synthesis resulted in membranes with enhanced hydrothermal stability. From the synthesis procedure which used a concentration of tetraethylorthosilicate (TEOS) of 1.94×10^{-2} mol m^{-3} and a concentration of aluminum tri-sec butoxide (ATSB) of 5.82 $\times 10^{-4}$ mol m^{-3} the nominal Si/Al ratio is calculated to be 33. The actual value could not be determined by chemical analysis because the permselective silica-alumina layer was very thin (~200 nm) and the underlying course alumina support would give an interference.

Past work [158] had shown that the permeance of the membrane stabilized after exposure to water vapor, and such a treatment was carried out here. The permeance of the membrane was 2.2 $\times 10^{-7}$ mol m^{-2} s^{-1} Pa^{-1} at 923 K and the selectivity of H_2 over CH_4, CO and CO_2 were 710, 500 and 420, respectively. The permeance dropped slightly to 1.6 × 10^{-7} mol m^{-2} s^{-1} Pa^{-1} at 873 K with the selectivity of H_2 over CH_4, CO and CO_2 being 940, 700 and 590, respectively.

The reactor configuration is given in Fig. 5.3. From the difference between the shell i.d. (14 mm) and the tube o.d. (10 mm) the catalyst bed thickness can be calculated (4 mm). In an earlier study of diffusional effects [160] the minimum permeance needed in order not to be transport-limited was calculated to be 2.5 × 10^{-7} mol m^{-2} s^{-1} Pa^{-1} for a pressure drop of 0.1 MPa and a 10 mm o.d membrane tube as used here. Since the permeance of the membranes used here are 2.2 $\times 10^{-7}$ mol m^{-2} s^{-1} Pa^{-1} at 923 K and 1.6 × 10^{-7} mol m^{-2} s^{-1} Pa^{-1} at 873 K with a pressure drop of 0.3 MPa, the requirement is fulfilled.

Fig. 4 presents the effects of pressure on the steam methane reforming in a semi-batch membrane reactor at 873 K and 923 K. The hydrogen flow rates from the tube side of the SBMR at 0.5, 1.0

and 1.5 MPa are plotted at 873 K (Fig. 4a) and at 923 K (Fig. 4b) respectively. When the reforming reaction was conducted at 0.5 MPa, the flow of hydrogen continued for almost 60 s. In a separate experiment where the reaction pressure was increased to 1.0 MPa, the flow of hydrogen started at a higher rate of 23 µmol s^{-1} (873 K) and 34 µmol s^{-1} (923 K) and continued at a declining rate for 150-200 s. As the reaction pressure was increased to 1.5 MPa, the initial flow rate of hydrogen (37 µmol s^{-1}) was higher and lasted for 500-600 s. The driving force for the permeation of hydrogen through the membrane was the difference in the partial pressures of hydrogen on opposite sides of the membrane. Thus, the hydrogen flow from the SBMR lasted at each pressure as long as there was a driving force in the system. As a result of this, the pressure in the shell side decreased throughout the process and the observed values are plotted in Fig. 5.5 at each temperature (873 K / Fig. 5.5a and 923 K / Fig. 5.5b). As the reaction pressure was increased, the drop in pressure in the SBMR was much higher and lasted longer due to the higher amount of hydrogen in the system. When the reaction was conducted at 0.5 MPa, the reactor pressure was dropped to 0.4 MPa for both temperatures (873 K and 923 K) in the first 10-20 seconds and did not show any measurable further decrease. When the reaction was conducted at 1.0 MPa, the reactor pressure kept decreasing and stabilized at a value of 0.9 MPa (873 K) or 0.7 MPa (923 K) in ~200 s. When the reaction was conducted at a higher pressure of 1.5 MPa, the overall reactor pressure also kept decreasing to reach to a value of 1.0 MPa (873 K) or 0.9 MPa (923 K) in ~500 s before the partial pressure of hydrogen in the shell side was equilibrated with the partial pressure of hydrogen in the tube side. It is worth pointing out that at the higher temperature of 923 K, although a larger amount of methane reacted, the terminal pressure in the shell side was lower than that at 873 K because of the greater amount of hydrogen permeation.

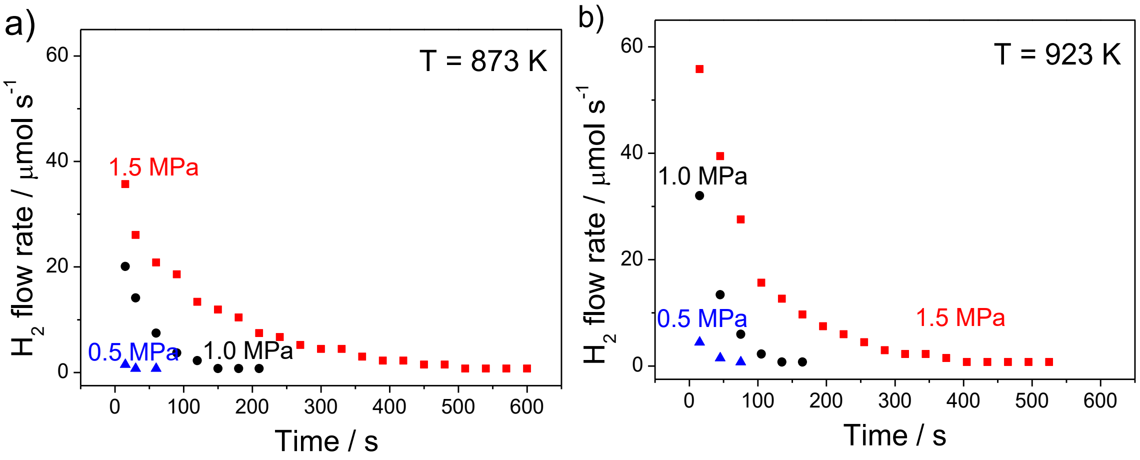

Fig. 5.4 Hydrogen permeate flow of semi-batch membrane reactor at a) 873 K and b) 923 K

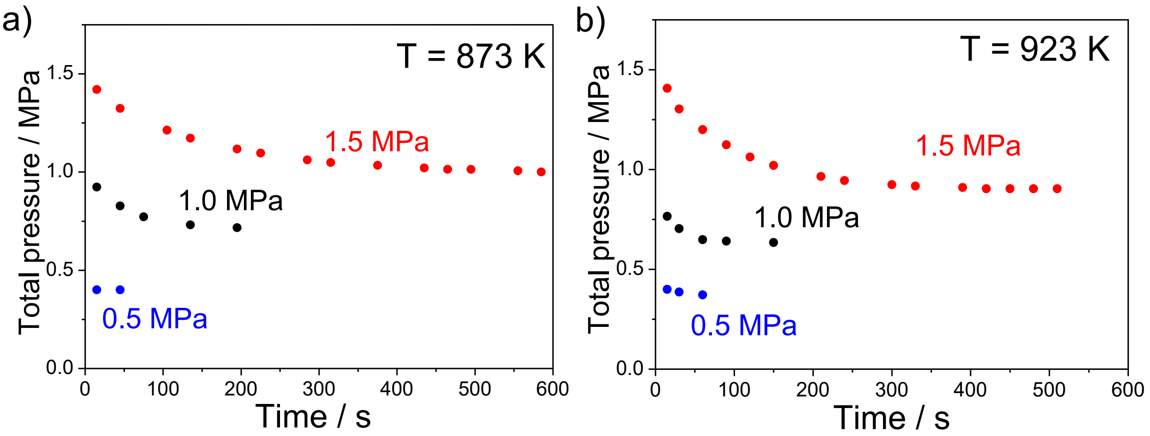

Fig. 5.5 Pressure change in shell side of semi-batch membrane reactor at a) 873 K and b) 923 K

The model to describe the system uses mostly known physical attributes of the membrane, the dimensions of the catalyst bed and reactor, and the kinetics of the reaction. Three fitted parameters are *k*, a mass transfer coefficient, *exV*, the extraneous volume of the system, and S_{H2O}, the membrane water-to-hydrogen selectivity parameter.

To optimize the two constants, *k* and *exV*, calculations based on the reactor model were used. This was carried out in a trial-and-error manner, by inputting values of the parameters and calculating hydrogen permeate flow curves. It was also necessary to obtain the selectivity parameter, and this was derived from the pressure drop curves.

For conditions of 923 K and 1.5 MPa initial pressure, Fig. 5.6 shows the hydrogen permeate flow for a value of *exV* of 5.0 and variable values of *k*. The curves with $k = 10^{-3}$ and $k = 10^{-4}$ are almost the same, so seemed to reach a limit. A value of $k = 10^{-5}$ was chosen for further calculations because the curve did not reach the limit line and was close to the experimental points.

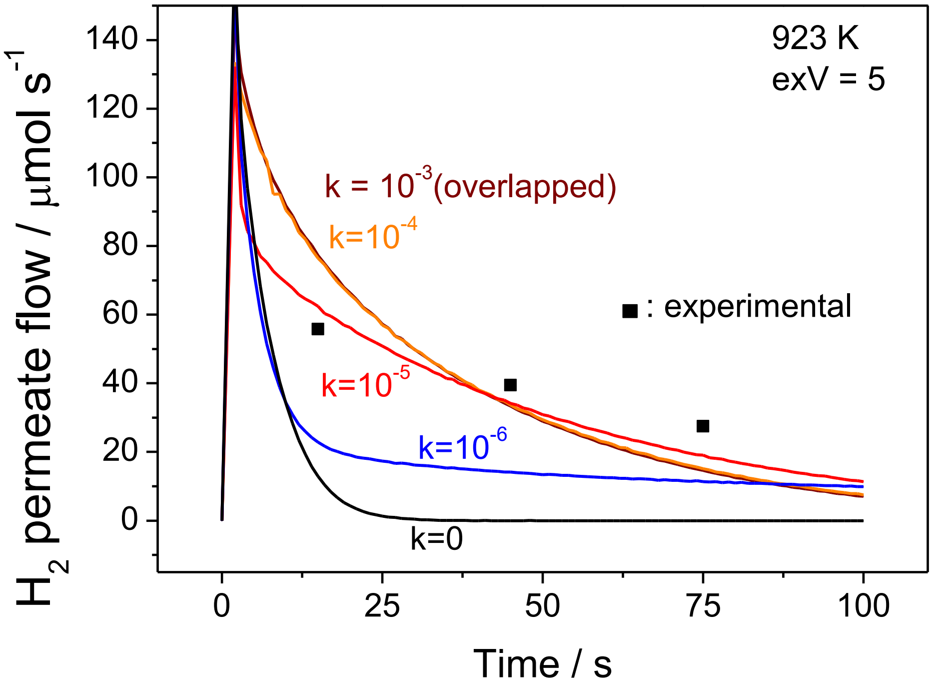

Fig. 5.6. Effect of *k* on the H_2 permeate flow in semi-batch operation at 923 K and 1.5 MPa initial pressure.

A longer time simulation was carried out and the results are shown in Fig. 5.7. In this figure, *k* was fixed at 10^{-5} and *exV* was varied. When *exV* = 7.5, the curve showed an excellent fit to the experimental values.

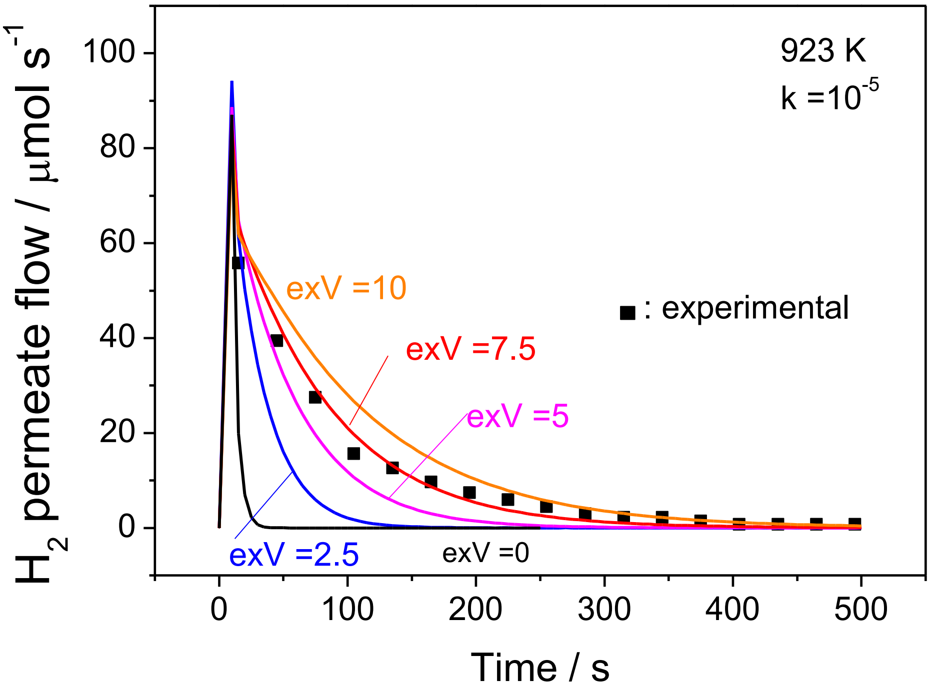

Fig. 5.7. The effect of *exV* in H_2 permeation flow in 500 s simulation

During semi-batch reactor operation, the total pressure in the shell side was measured. The result of total pressure measurement at 923 K and 1.5 MPa initial pressure is shown in Fig. 5.8. Simulations with Polymath were also conducted and the results are also shown in Fig. 5.8. The shapes of the curves for total pressure drop were similar to the experimental results, but the fits could not account for the drop in pressure except at *exV* = 0. This is because the membrane selectivity was assumed to be 100% for H_2 and did not account for the passage of one other gas that was present in the system, namely H_2O. As will be presented below, consideration of the passage of steam, which occurs to a small degree, does not affect the conclusions so far because steam does not affect the hydrogen permeance. However, taking into account the passage of steam does explain the observed decrease in total pressure.

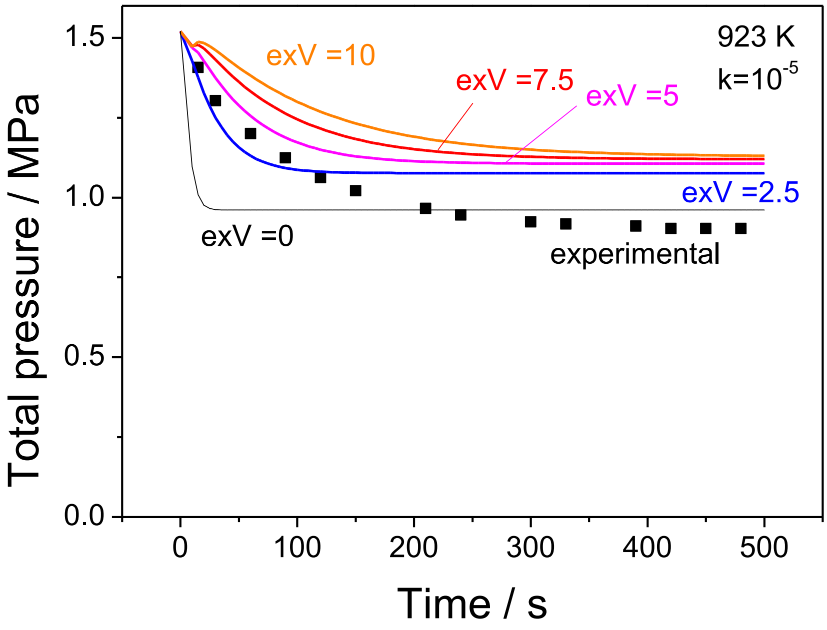

Fig. 5.8 Simulation results for pressure drop in the semi-batch membrane reactor

For further improvement of the simulation model, especially the fitting of the total pressure on the shell side, the permeation of water vapor was considered. The silica membrane used in this study has high selectivity for the other gases (CH_4, CO, CO_2). According to reports in previous studies, in silica membranes the permeance of steam can be estimated to be 4-10% of H_2 permeance [84, 161]. The result of the simulation considering steam permeation is shown in Fig. 5.9. The two variables *k* and *exV* were fixed at 10^{-5} and 7.5, respectively. The ratio of steam permeance over hydrogen permeance was varied from 0-20% and is referred to as $S_{H2O/H2}$ in the figure. Because of the permeation of steam, the total pressure showed a short, steep drop at the beginning but then its decrease became more moderate because of the increase in moles during reaction. When $S_{H2O/H2}$ = 0.04, the calculated total pressure matched the experimental results quite closely. In the following Fig. 5.10, the hydrogen permeance curves were re-calculated (solid curves), but with the increase in steam permeation, the permeate flow of hydrogen was scarcely affected. The calculations indicate that the previously obtained parameters ($k = 10^{-5}$, $exV = 7.5$) need not be changed. The figure also shows the permeate flow of steam (dashed curves) and these demonstrate substantial changes with selectivity, as expected. Meanwhile, the total amount of hydrogen produced decreased because of the loss of the reactant in the catalytic shell side. However, with consideration of the steam permeation ($S_{H2O/H2}$ = 0.04), the total amount of hydrogen was calculated as 4.87×10^{-3} mol, which is quite close to the experimental value (Table 5.8). It was not possible to measure the actual steam permeance because of analytical limitations, but the selectivity of $S_{H2O/H2}$ = 0.04 agrees with past reported measurements [84, 161].

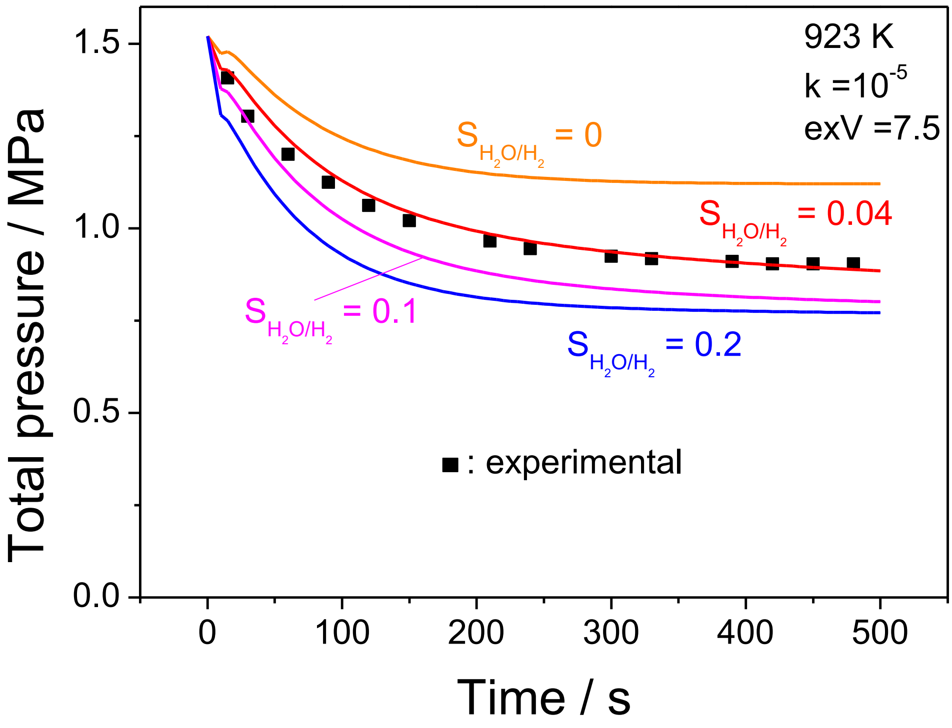

Fig. 5.9. Total pressure drop calculations varying water vapor permeation at 923 K.

$S_{H2O/H2}$: the ratio of steam permeance over hydrogen permeance (membrane selectivity for steam)

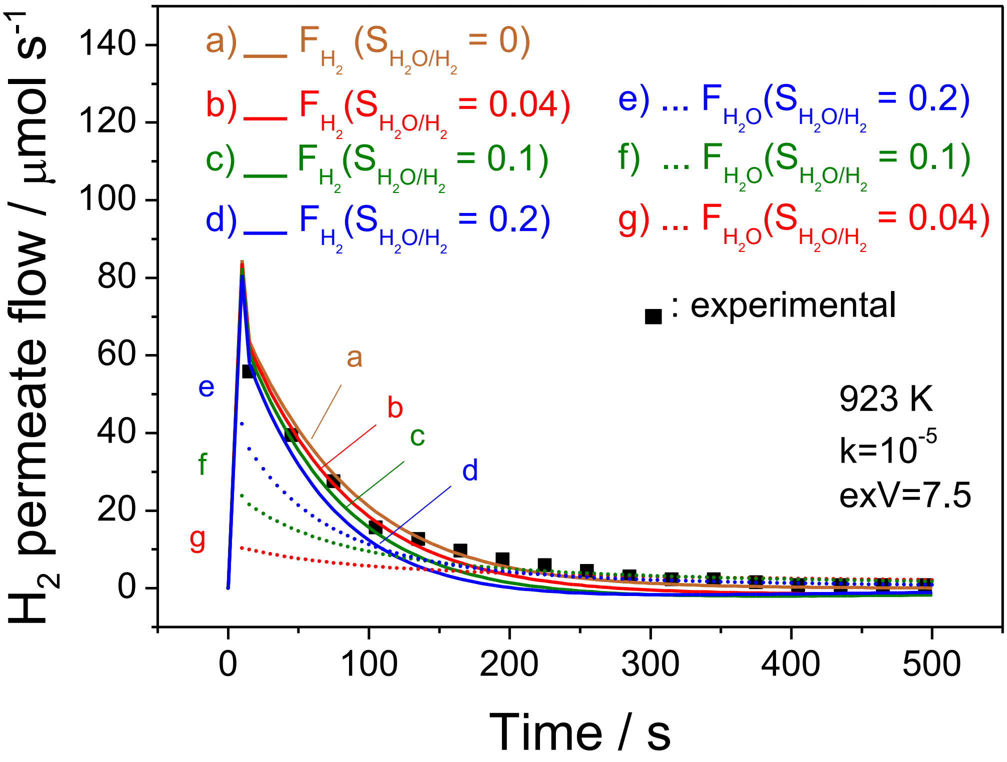

Fig. 5.10. Calculated permeate flows of H_2 and H_2O

Table 5.7 shows the productivities of hydrogen obtained for the SBMR and the continuous membrane reactor at 873 K and various pressures (0.5-3.0 MPa). The third and fourth rows list the experimental and simulated hydrogen productivities obtained in the semi-batch reactor. The one-dimensional model estimations matched the experimental values at a pressure range of 0.5-1.5 MPa. The fifth and sixth rows list the results of the continuous membrane reactor. The hydrogen productivities in the continuous membrane reactor were smaller than in the SBMR, especially at higher pressure.

Table 5.7. Experimental and simulated H_2 productivities obtained from semi-batch and continuous membrane reactors at 873 K

Temperature (K)	873					
Pressure (MPa)	0.50	1.0	1.5	2.0	2.5	3.0
Semi-batch membrane reactor (exp.) (mol)	5.57×10^{-5}	9.81×10^{-4}	4.43×10^{-3}	-	-	-
Semi-batch membrane reactor (sim.) (mol)	6.47×10^{-4}	1.73×10^{-3}	3.40×10^{-3}	5.46×10^{-3}	7.49×10^{-3}	9.62×10^{-3}
Continuous membrane reactor (exp.) (mol)	3.04×10^{-4}	3.52×10^{-4}	6.93×10^{-4}	-	-	-
Continuous membrane reactor (sim.) (mol)	2.18×10^{-4}	3.69×10^{-4}	4.96×10^{-4}	6.11×10^{-4}	7.16×10^{-4}	8.14×10^{-4}

A similar comparison at 923 K is shown in Table 5.8. Compared to Table 5.7, both of the experimental and calculated hydrogen productivity were larger at 923 K for all the conditions, as expected. The calculated hydrogen productivities in the SBMR were much higher than the ones in the continuous membrane reactor when the reforming reaction was conducted at 1.0 MPa or higher. Both the experimental results and the numerical simulations indicate that the application of the semi-batch reactor is beneficial when the reaction takes place at high pressures.

Table 5.8. Experimental and simulation H_2 productivities obtained from semi-batch and membrane reactors at 923 K

Temperature (K)	923					
Pressure (MPa)	0.50	1.0	1.5	2.0	2.5	3.0
Semi-batch membrane reactor (exp.) (mol)	1.34×10^{-4}	1.17×10^{-3}	4.90×10^{-3}	-	-	-
Semi-batch membrane reactor (sim.) (mol)	9.65×10^{-4}	2.90×10^{-3}	4.87×10^{-3}	7.26×10^{-3}	9.76×10^{-3}	1.23×10^{-2}
Membrane reactor (exp.) (mol)	3.82×10^{-4}	6.55×10^{-4}	8.84×10^{-4}	-	-	-
Membrane reactor (sim.) (mol)	2.99×10^{-4}	5.31×10^{-4}	7.31×10^{-4}	9.13×10^{-4}	1.08×10^{-3}	1.24×10^{-3}
Ideal semi-batch membrane reactor (sim.) (mol.)	3.12×10^{-4}	6.56×10^{-4}	1.02×10^{-3}	1.40×10^{-3}	1.78×10^{-3}	2.17×10^{-3}

In the last row of Table 8, shows the simulation results of an ideal semi-batch operation. In an ideal configuration, the catalyst bed and membrane would substantially extend lengthwise and would comprise almost the entire volume of the reactor and the *exV* would be zero. It can be seen that the hydrogen productivities are the highest for this case, as expected because of full utilization of the membrane. It is envisioned that in practice semi-batch membrane reactor systems would be implemented with many units in an arrangement that would allow sequential filling and discharge, much like in a commercial pressure-swing adsorption system.

5.4. Conclusion

This study examines the feasibility of operating a membrane reactor for hydrogen production in a semi-batch mode in order to harness the increase in moles from the stoichiometry of the generating reaction so as to produce autogeneous pressure. Although membrane reactors have been used extensively in the past to enhance yields in gas-phase reactions, particularly to overcome equilibrium limitations by carrying out simultaneous reaction and separation, this is the first time that the generation of pressure has been envisioned. This is important because many hydrogen producing reactions, e.g. reforming, dehydrogenation, aromatization, result in an increase in moles, and pressure is a driving force for membrane separation.

The steam methane reforming ($CH_4 + H_2O \rightarrow CO + 3H_2$), a reaction in which the number of moles doubles, was studied experimentally in a semi-batch membrane reactor and a membrane reactor at various temperatures (873 K, 923 K) and pressures (0.5-1.5 MPa). A hydrothermally stable hydrogen selective silica-alumina membrane was used in the experiments. Additionally, one-dimensional modeling studies of the semi-batch and the membrane reactor were carried out to calculate and compare hydrogen productivities. The laboratory scale experiments necessitated an extra volume outside the catalyst bed that accommodated the valving needed to isolate the reactor, so the modeling considered diffusion from this extra volume. In addition, it was found that consideration of the permeation of water vapor improved the simulation model, especially for the calculation of the total pressure.

The hydrogen productivities obtained from both the continuous and the semi-batch membrane reactor increased with pressure. The hydrogen productivity at 923 K from the continuous reactor was higher than that from the semi-batch reactor at low pressure, but reached similar values at 1.0 MPa, and was greatly surpassed at 1.5 MPa. Similar results were obtained at 873 K. The simulation results showed that increasing pressure can enhance the hydrogen productivities of the semi-batch reactor above those obtained from the continuous membrane reactor. This semi-batch mode of operation can conceivably be applied in a network of reactors undergoing successive filling, reaction, and discharge.

List of symbols

Symbol	Units	Meaning	Value
W_c	J	compression energy	
η	-	efficiency	
R	$J\ mol^{-1}\ K^{-1}$	gas constant	8.31
γ	-	heat capacity ratio	
P_h	Pa	higher pressure	
P_l	Pa	lower pressure	
ΔH^o_{298}	$kJ\ mol^{-1}$	standard enthalpy of formation	
r_i	$mol\ kg_{cat}^{-1}\ s^{-1}$	reaction rate for ith reaction	
k_i		reaction constant for ith reaction	
P_i	Pa	partial pressure of i	
DEN	-	denominator	
K_{eqi}		equilibrium constant for ith reaction	
A_i		pre-exponential factor for k_i	
E_i	$kJ\ mol^{-1}$	activation energy for ith reaction	
K_j		adsorption constant of j	
B_j		pre-exponential factor for K_j	
ΔH_j	$kJ\ mol^{-1}$	heat of adsorption of j	
F_j	$mol\ s^{-1}$	molar flow rate of j	
w	kg	weight of the catalyst	
$\alpha_{i,j}$	-	stoichiometric ratio of j in the ith reaction	
R_i	$mol\ kg_{cat}^{-1}\ s^{-1}$	reaction rate of ith reaction	
R_{jp}	$mol\ kg_{cat}^{-1}\ s^{-1}$	permeation rate of j	
$\overline{P}_J$	$mol\ m^{-2}\ s^{-1}\ Pa^{-1}$	gas permeance of j	
a	m^2	membrane area	1.76×10^{-3}
P_{jf}	Pa	partial pressure of i in feed flow	
P_{jp}	Pa	partial pressure of i in permeate flow	
τ	s	residence time in the reactor	
V_{ex}	m^3	extra volume in SBMR operation	
V_{cat}	m^3	catalyst bed volume	6.03×10^{-6}
V_{total}	m^3	total system volume	
k	$mol\ m^{-2}\ Pa^{-1}$	mass transfer coefficient	

$F_{D,j}$	mol s^{-1}	molar flow of j	
$D_{self,j}$	m^2 s^{-1}	self-diffusion coefficient of j	
ΔP_j	Pa	partial pressure difference of j	
exV		dimensionless extra volume	
$N_{j,cat}$	mol	mole of j in catalyst bed	
$N_{j,ex}$	mol	mole of j in extra volume	

Chapter 6. Overall Conclusion and Future Visions

For the application of hydrogen-permselective membranes to steam methane reforming in a membrane reactor, first the kinetics of the reaction on a Ni/MgO-SiO_2 catalyst were studied. Second, the synthesis and properties of silica-alumina membranes were also investigated. The steam methane reforming was described by a simple kinetic model. The membrane showed excellent H_2 permeance as high as $2x10^{-7}$ mol $m^{-2}s^{-1}Pa^{-1}$ and H_2/N_2 selectivity of 500 with enough hydrothermal stability for use as the membrane reactor. The membrane did improve the methane conversion by extracting produced hydrogen to the other side of reaction zone.

As an advanced application, semi-batch operation of the silica-alumina membrane was studied. In semi-batch operation, the reactant gas flow of a membrane reactor was intentionally stopped then the reaction and permeation continued. Its behavior was well-described by a mass transfer model by allowing diffusion of the reactant from the upstream and downstream sides.

This thesis showed the possibility of using silica-alumina membranes as a part of a membrane reactor or a semi-batch reactor for hydrogen production process. When a well-designed membrane with proper permselectivity and durability is obtained, it can be applied for membrane reactors with variety of reactions, conditions, and type of membranes.

However, there is still room for improvement. Silica-based membrane have advantages over palladium-based membrane in raw material costs, however, besides the price of the material itself, the time needed for the synthesis of the membrane is also significant. From this standpoint, the silica-alumina membrane used in this thesis needs almost one week to prepare, therefore improvements for fast preparation would be needed for practical applications.

The membrane reactor discussed in this thesis had a simple geometry, only one tubular membrane in one catalyst bed in one straight concentric tubular reactor. Thanks to this simplicity, its behavior was able to be described by 1-D calculations. However, for the optimization of the process cost in total, the volume of the catalyst bed, numbers of membranes and its coordination including reactor scale and feed flow is needed for considering the cost of each component. In order to help this optimization, the kinetic analysis which explains how hydrogen producing reactions proceeds plays a very important role. The analysis itself requires a certain cost, a model to use must be carefully selected based on the reliability and simplicity. This thesis only focused on SMR and WGS, but this knowledge can be expanded to another reaction processes.

Hopefully a novel hydrogen production process will be developed based on this research.

References

[1] G. Marbán, T.V. Solís, Towards the hydrogen economy?, Int. J. Hydrogen Energy 32 (2007) 1625-1637.

[2] C. Cao, N. Zhang, Y. Cheng, Numerical analysis on steam methane reforming in a plate microchannel reactor: Effect of washcoat properties. Int. J. Hydrogen Energy 41 (2016) 18921.

[3] M. Broda, V. Manovic, Q. Imitiaz, A.M. Kierzkowskaa, E.J. Anthoniy, C.R. Müller, High-purity hydrogen via the sorption-enhanced steam methane reforming reaction over a synthetic CaO-based sorbent and a Ni catalyst, Environ. Sci. Technol. 47 (2013) 6007-6014.

[4] A. Antzara, E. Heracleous, L. Silvester, D.B. Bukur, A.A. Lemonidou, Activity study of NiO-based oxygen carriers in chemical looping steam methane reforming, Catal. Today, 272 (2016) 32-41.

[5] P. Hacarlioglu, Y. Gu, S.T. Oyama, Studies of the methane steam reforming reaction at high pressure in a ceramic membrane reactor, J. Nat. Gas Chem. 15 (2006) 73-81.

[6] V. Kyriakou, I. Garagounis, A. Vourros, E. Vasileiou, A. Manerbino, W.G. Coors, M. Stoukides, Methane steam reforming at low temperatures in a $BaZr_{0.7}Ce_{0.2}Y_{0.1}O_{2.9}$ proton conducting membrane reactor, App. Catal. B 186 (2016) 1-9.

[7] A. Giaconia, M. de Falco, G. Caputo, R. Grena, P. Tarquini, L. Marrelli, Solar steam reforming of natural gas for hydrogen production using molten salt heat carriers, AIChE J. 54 (2008) 1932–1944.

[8] G. Postole, A. Auroux, The poisoning level of Pt/G catalysts used in PEM fuel cells by the hydrogen feed gas impurities: The bonding strength, Int. J. Hydrogen Energy 36 (2011) 6817-6825.

[9] B.Castro-Dominguez, I.P. Mardilovich, R. Ma, N.K. Kazantzis, A.G. Dixon, Y.H. Ma, Performance of a pilot-scale multitube membrane module under coal-derived syngas for hydrogen production and separation, J. Membr. Sci. 523 (2017) 515-523.

[10] M.A. Murmura, S. Cerbelli, M.C. Annesini, Designing the optimal geometry of a membrane reactor for hydrogen production from a pre-reformed gas mixture based on the extent of the reaction boundary layer, Chem. Eng. Process 120 (2017) 148-160.

[11] B. Anzelmo, S. Liguori, I. Mardilovich, A. Iulianelli, Y.-H. Ma, J. Wilcox, A. Basile, Fabrication & performance study of a palladium on alumina supported membrane reactor: Natural gas steam reforming, a case study, Int. J. Hydrogen Energy, In Press.

[12] A. Mundstock, S. Friebe, J. Caro, On comparing permeation through Matrimid-based mixed matrix and multilayer sandwich FAU membranes: H_2/CO_2 separation, support functionalization and ion exchange, Int. J. Hydrogen Energy 42 (2017) 279-288.

[13] S.-J. Ahn, A. Takagaki, T. Sugawara, R. Kikuchi, S.T. Oyama, Permeation properties of silica-zirconia composite membranes supported on porous alumina substrates, J. Membr. Sci. 526 (2017) 409-416.

[14] M.B. Karimi, S. Hassanajili, Short fiber/polyurethane composite membrane for gas separation, J. Membr. Sci. 543 (2017) 40-48.

[15] P. Sang, L. Zhao, J. Xu, Z. Shi, S. Guo, Y. Yu, H. Zhu, Z. Yan, W. Guo, Excellent membranes for hydrogen purification: Dumbbell-shaped porous γ-graphynes, Int. J. Hydrogen Energy 42 (2017) 5168-5176.

[16] J.B. James, Y.S. Lin, Thermal stability of ZIF-8 membranes for gas separations, J. Membr. Sci. 532 (2017) 9-19.

[17] S.T.B. Lundin, T. Yamaguchi, C.A. Solden, S.T. Oyama, J.D. Way, The role (or lack thereof) of nitrogen or ammonia adsorption-induced hydrogen flux inhibition on palladium membrane performance, J. Membr. Sci. 15 (2016) 65-72.

[18] S.T. Oyama, M. Yamada, T. Sugawara, A. Takagaki, R. Kikuchi, Development of inorganic–organic hybrid membranes for carbon dioxide/methane separation, J. Jpn. Pet.

Inst. 54 (2011) 298-309.

[19] S. Suzuki, S.B. Messaoud, A. Takagaki, T. Sugawara, R. Kikuchi, S.T. Oyama, Development of inorganic-organic hybrid membranes for carbon dioxide/methane separation, J. Membr. Sci. 471 (2014) 402-411.

[20] S.B. Messaud, A. Takagaki, T. Sugawara, R. Kikuchi, S.T. Oyama, Alkylamine-silica hybrid membranes for carbon dioxide/methane separation, J. Membr. Sci. 477 (2015) 161-171.

[21] M. Kanezashi, R. Matsugasako, H. Tawarayama, H. Nagasawa, T. Tsuru, Pore size tuning of sol-gel-derived triethoxysilane (TRIES) membranes for gas separation, J. Membr. Sci. 524 (2017) 64-72.

[22] J. Xu, G.F. Froment, Methane steam reforming, methanation and water-gas shift: I. Intrinsic kinetics. AIChE J. 35 (1989) 88-96.

[23] J. Solsvik, H. A. Jakobsen, On the modeling of one-dimensional membrane reactors: Application to hydrogen production in fixed packed bed, Fuel 202 (2017) 595-612.

[24] N. Lu, F. Gallucci, T. Melchiori, D. Xie, M.V.S. Annaland, Modeling of autothermal reforming of methane in a fluidized bed reactor with perovskite membranes, Chem. Eng. Process, In Press.

[25] V. Vaiano, O. Sacco, D. Pisano, D. Sannino, P. Ciambelli, From the design to the development of a continuous fixed bed photoreactor for photocatalytic degradation of organic pollutants in waste water. Chem. Eng. Sci. 137 (2015) 152.

[26] P. Sadooghi, R. Rauch, Experimental and modeling study of hydrogen production from catalytic steam reforming of methane mixture with hydrogen sulfide. Int. J. Hydrogen Energy 40 (2015) 10418.

[27] N. Chatrattanawet, S. Skogestad, A. Arpornwichanop, Control structure design and dynamic modeling fora solid oxide fuel cell with direct internal reforming of methane. Chem. Eng. Res. Des. 98 (2015) 202.

[28] K.-S. Kang, C.-H. Kim, K.-K. Bae, W.-C. Cho, S.-U. Jeong, Y.-J. Lee, C.-S. Park, Reduction and oxidation properties of Fe_2O_3/ZrO_2 oxygen carrier for hydrogen production.

Chem. Eng. Res. Des. 92 (2014) 2584.

［29］ D.W. Flaherty, W.-Y. Yu, Z. D. Pozun, G. Henkelman, C. B. Mullins, Mechanism for the water–gas shift reaction on monofunctional platinum and cause of catalyst deactivation. J. Catal. 282 (2011) 278.

[30] R. Zheng, R. Diver, D. Caldwell, B. Fritz, R. Cameron, P. Humble, W. TeGrotenhuis, R. Dagle, R. Wegeng, Integrated solar thermochemical reaction system for steam methane reforming. Energy Procedia 69, (2015) 1192.

[31] A.Hafizi, M.R. Rahimpour, S. Hassanajili, Calcium promoted Fe/Al_2O_3 oxygen carrier for hydrogen production via cyclic chemical looping steam methane reforming process. Int. J. Hydrogen Energy 40 (2015) 16159.

[32] K. Metaxas, J.W. Thybaut, G. Morra, D. Farrusseng, C. Mirodatos, G.B. Marin, A microkinetic vision on high-throughput catalyst formulation and optimization: development of an appropriate software tool, Top. Catal. 53 (2010) 64-76.

[33] H. Wu, V. La Parola, G. Panteleo, F. Puleo, A.M. Venezia, L.F. Liotta, Ni-based catalysts for low temperature methane steam reforming: recent results on Ni-Au and comparison with other bi-metallic systems. Catalysts 3 (2013) 563.

[34] D. Karimipourfard, S. Kabiri, M.R. Rahimpour,A novel integrated thermally double coupled configuration for methane steam reforming, methane oxidation and dehydrogenation of propane. J. Nat. Gas Sci. Eng. 21 (2014) 134.

[35] P. Xu, Z. Zhou, C. Zhao, Z. Cheng, Catalytic performance of Ni/CaO-$Ca_5Al_6O_{14}$ bifunctional catalyst extrudate in sorption-enhanced steam methane reforming. Catal. Today 259 (2016) 347.

[36] T.W. Kim, J.C. Park, T.-H. Lim, H. Jung, D.H. Chun, H.T. Lee, S. Hong, J.-I. Yang, The kinetics of steam methane reforming over a Ni/γ-Al_2O_3 catalyst for the development of small stationary reformers. Int. J. Hydrogen Energy 40 (2015) 4512.

[37] S.Y. Lee, H. Lim, H.C. Woo, Catalytic activity and characterizations of Ni/$K_2Ti_xO_y$-Al_2O_3 catalyst for steam methane reforming. Int. J. Hydrogen Energy, 39 (2014) 17645.

[38] B. Chu, N. Zhang, X. Zhai, X. Chen, Y. Cheng, Improved catalytic performance of Ni

catalysts for steam methane reforming in a micro-channel reactor. J. Energy Chem. 23 (2014) 593.

[39] Z. Boukha, C. Jiménez-González, B. de Rivas, J.R. González-Valasco, J.I. Gutiérrez-Ortiz, R. López-Fonseca, Synthesis, characterisation and performance evaluation of spinel-derived Ni/Al_2O_3 catalysts for various methane reforming reactions. Appl. Catal., B 158-159 (2014), 190.

[40] Kho, E. T.; Scott, J.; Amal, R. Ni/TiO_2 for low temperature steam reforming of methane. *Chem. Eng. Sci.* **2016**, 140, 161.

[41] Y. Zhang, W. Wang, Z. Wang, X. Zhou, Z. Wang, C.-J. Liu, Steam reforming of methane over Ni/SiO_2 catalyst with enhanced coke resistance at low steam to methane ratio. Catal. Today 256 (2015) 130.

[42] H.-S. Roh, I.-H. Eum, D.-W. Jeong, Low temperature steam reforming of methane over Ni-$Ce_{(1-x)}Zr_{(x)}O_2$ catalysts under severe conditions. Renew. Energy 42 (2012) 212.

[43] X. Wu, C. Wu, S. Wu, Dual-enhanced steam methane reforming by membrane separation of H_2 and reactive sorption of CO_2. Chem. Eng. Res. Des. 96 (2015) 150.

[44] A.G. Gil, Z. Wu, D. Chadwick, K. Li, Ni/SBA-15 catalysts for combined steam methane reforming and water gas shift—Prepared for use in catalytic membrane reactors. Appl. Catal., A 506 (2015) 188.

[45] A.B. Hungria, M. Fernández-Garcia, J.A. Anderson, A. Martínez-Arias, The effect of Ni in Pd–Ni/(Ce,Zr)O_x/Al_2O_3 catalysts used for stoichiometric CO and NO elimination. Part 2: Catalytic activity and in situ spectroscopic studies. J. Catal. 235 (2005) 262.

[46] S.T. Oyama, X. Zhang, J. Lu, Y. Gu, T. Fujitani, Epoxidation of propylene with H_2 and O_2 in the explosive regime in a packed-bed catalytic membrane reactor. J. Catal. 257 (2008) 1.

[47] G.B. Marin, G.S. Yablonsky, *Kinetics of Chemical Reactions*; John Wiley & Sons, Inc.: New York, 2011.

[48] G.F. Froment, K.B. Bischoff, J. De Wilde, *Chemical Reactor Analysis and Design*, 3rd ed.; John Wiley & Sons, Inc.: New York, 2010.

[49] C. Sprung, P.N. Kechagiopoulos, J.W. Thybaut, B. Arsted, U. Olsbye, G.B. Marin, Microkinetic evaluation of normal and inverse kinetic isotope effects during methane steam reforming to synthesis gas over a Ni/NiAl_2O_4 model catalyst. Appl. Catal., A 492 (2015) 231.

[50] T. Numaguchi, K. Kikuchi, Intrinsic kinetics and design simulation in a complex reaction network: steam-methane reforming. Chem. Eng. Sci. 43 (1988) 2295.

[51] K. Hou, R. Hughes, The kinetics of methane steam reforming over a Ni/α-Al_2O_3 catalyst. Chem. Eng. J. 82 (2001) 311.

[52] Wang, F.; Qi, B.; Wang, G.; Li, L. Methane steam reforming: kinetics and modeling over coating catalyst in micro-channel reactor. Int. J. Hydrogen Energy 38 (2013) 5693.

[53] K. Jarosch, T. El Solh, H.I. de Lasa, Modelling the catalytic steam reforming of methane: discrimination between kinetic expressions using sequentially designed experiments. Chem. Eng. Sci. 57 (2002) 3439.

[54] A.L.Y. Tonkovich, B. Yang, S.T. Perry, S.P. Fitzgerald, Y. Wang, From seconds to milliseconds through tailored microchannel reactor design of a steam methane reformer. Catal. Today 120 (2007) 21.

[55] B. Wang, J. Zhu, Z. Lin, A theoretical framework for multiphysics modeling of methane fueled solid oxide fuel cell and analysis of low steam methane reforming kinetics. Appl. Energy 176 (2016) 1.

[56] M. Saito, J. Kojima, H. Iwai, H. Yoshida, H. The limiting process in steam methane reforming with gas diffusion into a porous catalytic wall in a flow reactor. Int. J. Hydrogen Energy 40 (2015) 8844.

[57] M. Maestri, D.G. Vlachos, A. Baretta, G. Groppi, E. Tronconi,Steam and dry reforming of methane on Rh: Microkinetic analysis and hierarchy of kinetic models. J. Catal. 259 (2008) 211.

[58] S.D. Angeli, G. Monteleone, A. Giaconia, A.A. Lemonidou, State-of-the-art catalysts for CH_4 steam reforming at low temperature. J. Hydrogen Energy 39 (2014) 1979.

[59] R. Chaubey, S. Sahu, O.O. James, S. Maity, A review on development of industrial

processes and emerging techniques for production of hydrogen from renewable and sustainable sources. Renew. Sust. Energ. Rev. 23 (2013) 443.

[60] N. Kageyama, B. Devocht, A. Takagaki, K. Toch, J. Thybaut, G. Marin, S.T. Oyama, The interplay of kinetics and thermodynamics in the catalytic steam methane reforming over Ni/MgO-SiO_2, Ind. Eng. Chem. Res. 56 (2017) 1148-1158.

[61] A. Golmakani, S. Fatemi, J. Tamnanloo, Investigating PSA, VSA, and TSA methods in SMR unit of refineries for hydrogen production with fuel cell specification, Sep. Purif. Technol. 176 (2017) 73-91.

[62] A. Jafari, N. Saadatjou, S. Sahebdelfar, Influence of chemical treatments of activated carbon support on the performance and deactivation behavior of promoted Ru catalyst in ammonia synthesis, Int. J. Hydrogen Energy 40 (2015) 3659-3671.

[63] G. Postole, A. Auroux, The poisoning level of Pt/C catalysts used in PEM fuel cells by the hydrogen feed gas impurities: The bonding strength, Int. J. Hydrogen Energy 36 (2011) 6817-6825.

[64] H.W. Abu El Hawa, S.N. Paglieri, C.C. Morris, A. Harale, J.D. Way, Application of a Pd-Ru composite membrane to hydrogen production in a high temperature membrane reactor, Sep. Purif. Technol. 147 (2015) 388-397.

[65] A. Shafiee, M. Arab, Z. Lai, Z. Liu, A. Abbas, Modelling and sequential simulation of multi-tubular metallic membrane and techno-economics of a hydrogen production process employing thin-layer membrane reactor, Int. J. Hydrogen Energy 41 (2016) 19081-19097.

[66] S. Adhikali, S. Fernando, Hydrogen membrane separation techniques, Ind. Eng. Chem. Res. 45 (2006) 875-881.

[67] M. Miyamoto, M. Tokiwa, Y. Oumi, S. Uemiya, Effect of adhesion of metals on deterioration of Pd and Pd alloy membranes, J. Alloys. Compd. 577 (2013) 445-450.

[68] P. Bernardo, G. Barbieri, E. Drioli, Evaluation of membrane reactor with hydrogen-selective membrane in methane steam reforming, Chem. Eng. Sci. 65 (2010) 1159-1166.

[69] T.P. Tiemersma, C.S. Patil, M. Annaland, J.A.M. Kuipers, Modelling of packed bed

membrane reactors for autothermal production of ultrapure hydrogen, Chem. Eng. Sci. 61 (2006) 1602-1616.

[70] Y. Shirasaki, T. Tsuneki, Y. Ota, I. Yasuda, S. Tachibana, H. Nakajima, K. Kobayashi, Development of membrane reformer system for highly efficient hydrogen production from natural gas, Int. J. Hydrogen Energy 34 (2009) 4482-4487.

[71] A.G. Gil, Z. Wu, D. Chadwick, K. Li, A catalytic hollow fibre membrane reactor for combined steam methane reforming and water gas shift reaction, Chem. Eng. Sci. 137 (2005) 364-372.

[72] S.-E. Nam, K.-H. Lee, Hydrogen separation by Pd alloy composite membranes: introduction of diffusion barrier, J. Membr. Sci. 192 (2001) 177-185.

[73] S.J. Khatib, S.T. Oyama, Silica membranes for hydrogen separation prepared by chemical vapor deposition (CVD), Sep. Purif. Technol. 111 (2013) 20-42.

[74] M. Patrascu, M. Sheintuch, On-site pure hydrogen production by methane steam reforming in high flux membrane reactor: Experimental validation, model predictions and membrane inhibition, Chem. Eng. J. 262 (2015) 862-874.

[75] M.L.H. Wise, J.P.G. Farr, I.R. Harris, X-ray studies of the α/β miscibility gaps of some palladium solid solution-hydrogen systems, J. Less-Common Metals 41 (1975) 115-127.

[76] S.-T. B. Lundin, J. O. Law, N. S. Patki, C. A. Wolden, J. D. Way, Glass frit sealing method for macroscopic defects in Pd-based composite membranes with application in catalytic membrane reactors, Sep. Purif. Technol. 172 (2017) 68-75.

[77] T. Okubo, H. Inoue, Introduction of specific gas reactivity to porous glass membranes by treatment with tetraethoxysilane, J. Membr. Sci. 42 (1989) 109.

[78] G. R. Gavalas, C.E. Megiris, S. W. Nam, Deposition of H_2-permselective SiO_2 films, Chem. Eng. Sci. 44 (1989) 1829.

[79] S.J. Khatib, K. de Souza, F.B. Noronha, S.T. Oyama, Review of silica membranes for hydrogen separation prepared by chemical vapor deposition (CVD) in Inorganic, Polymeric, and Composite Membranes: Structure Function and Other Correlations, S. Ted Oyama, Susan Michelle Stagg Williams, Eds. Elsevier, Amsterdam, 2011, pp. 25-60,

Membr. Sci. Technol. 14 (2011) 25-60.

[80] S.B. Desu, Decomposition chemistry of tetraethoxysilane, J. Am. Chem. Soc. 72 (1989) 1615-1621.

[81] R.J.R. Ulhorn, K. Keizer, A. J. Burggraaf, Gas transport and separation with ceramic membranes. Part II: Synthesis and separation properties of microporous membranes, J. Membr. Sci. 66 (2/3) (1992) 415.

[82] R. S. A. de Lange, K-N. P. Kumar, J. H. A. Hekkink, G. M. H. Van de Velde, K. Keizer, A. J. Burggraaf, W. H. Dokter, H.F. van Garderen, T. P. M. Beelen, Microporous SiO2 and SiO2/MOx (M=T, Zr, Al) for ceramic membrane applications; A microstructural study of the sol-stage and the consolidated state, J. Sol-Gel Sci. Technol., 2 (1994) 489.

[83] B. N. Nair, T. Yamaguchi, T. Okubo, H. Suematsu, K. Keizer, S. I. Nakao, Sol-gel synthesis of molecular sieving silica membranes, J. Membr. Sci. 135 (1997) 237.

[84] M. Kanezashi, M. Asaeda, Hydrogen permeation characteristics and stability of Ni-doped silica membranes in steam at high temperature, J. Membr. Sci. 271 (2006) 86-93.

[85] Y. Gu, S.T. Oyama, Ultrathin, hydrogen-selective silica membranes deposited on alumina-graded structures prepared from size-controlled boehmite sols, J. Membr. Sci. 306 (2007) 216-227.

[86] M. Nomura, K. Ono, S. Gopalakrishnan, T. Sugawara, S.-I. Nakao, Preparation of a stable silica membrane by a counter diffusion chemical vapor deposition method, J. Membr. Sci. 251 (2005) 151-158.

[87] X.-L. Zhang, H. Yamada, T. Saito, T. Kai, K. Murakami, M. Nakashima, J. Ohshita, K. Akamatasu, S.-I. Nakao, Development of hydrogen-selective triphenylmethoxysilane-derived silica membranes with tailored pore size by chemical vapor deposition, J. Membr. Sci. 499 (2016) 28-35.

[88] Y. Ohta, K. Akamatsu, T. Sugawara, A. Nakao, A. Miyoshi, S.-I. Nakao, Development of pore size-controlled silica membranes for gas separation by chemical vapor deposition, J. Membr. Sci. 315 (2008) 93-99.

[89] Y.-S. Kim, K. Kusakabe, S. Morooka, S-M. Yang, Deposition of H_2- permselective SiO_2

films, Korean J. Chem. Eng. 18 (2001) 106-112.

[90] J.C.S. Wu, H. Sabol, G.W. Smith, D.L. Flowers, P.K.T. Liu, Characterization of hydrogen-permselective microporous ceramic membranes, J. Membr. Sci. 96 (1994) 275-287.

[91] B.-K. Sea, E. Soewito, M. Watanabe, K. Kusakabe, S. Morooka, S.S. Kim, Hydrogen recovery from a H_2− H_2O− HBr mixture utilizing silica-based membranes at elevated temperatures. 1. Preparation of H_2O-and H_2-selective membranes, Ind. Eng. Chem. Res. 37 (1998) 2502-2508.

[92] M.C. Duke, J.C. Diniz da Costa, D.D. Do, P.G. Gray, G.Q. Lu, Hydrothermally robust molecular sieve silica for wet gas separation, Adv. Funct. Mater. 16 (2006) 1215-1220.

[93] S. Battersby, S. Smart, B. Ladewig, S. Liu, M.C. Duke, V. Rudolph, J.C. Diniz da Costa, Hydrothermal stability of cobalt silica membranes at high temperatures, J. Am. Ceram. Soc. 91 (2008) 2975-2981.

[94] Y. Gu, S.T. Oyama, Permeation properties and hydrothermal stability of silica-titania membranes supported on porous alumina substrates, J. Membr. Sci. 345 (2009) 267-275.

[95] V. Boffa, D.H.A. Blank, J.E. Elshof, Hydrothermal stability of microporous silica and niobia-silica membranes, J. Membr. Sci. 319 (2008) 256-263.

[96] Y. Gu, P. Hacarlioglu, S.T. Oyama, Hydrothermally stable silica–alumina composite membranes for hydrogen separation, J. Membr. Sci. 310 (2008) 28-37.

[97] E. Matsuyama, A. Ikeda, M. Komatsuzaki, M. Sasaki, M. Nomura, High-temperature propylene/propane separation through silica hybrid membranes, Sep. Purif. Technol. 128 (2014) 25-30]

[98] M.A. Aroon, A.F. Ismail, T. Matsuura, Beta-cyclodextrin functionalized M WCNT: A potential nano-membrane material for mixed matrix gas separation membranes development, Sep. Purif. Technol. 115 (2013) 39-50.

[99] S. Feng, J. Ren, K. Hua, H. Li, X. Ren, M. Deng, Poly(amide-12-bethyleneoxide)/polyethylene glycol blend membranes for carbon dioxide separation, Sep. Purif. Technol. 116 (2013) 25–34.

[100] Knudsen, M., Ann. Phys. 28, 75 (1909).

[101] B. V. Deriagin, S. P. Bakanov, Theory of flow of a gas in a porous material in the near-Knudsen region. Tech. Phys. 2 (1957) 1904-1911.

[102] T. Yoshioka, E. Nakanishi, T. Tsuru, M. Asaeda, Experimental studies of gas permeation through microporous silica membranes, AIChE J. 47 (2001) 2052-2063.

[103] Y. Gu, S.T. Oyama, High molecular permeance in a poreless ceramic membrane, Adv. Mater. 19 (2007) 1636-1640.

[104] S.T. Oyama, D. Lee, P. Hacarlioglu, R.F. Saraf, Theory of hydrogen permeability in nonporous silica membranes, J. Membr. Sci. 244 (2004) 45-53.

[105] E. Kikuchi, Palladium/ceramic membranes for selective hydrogen permeation and their application to membrane reactor, Catal. Today 25 (1995) 333-337.

[106] J.E. Shelby, Helium migration in natural and synthetic vitreous silica, J. Am. Ceram. Soc. 55 (1972) 61-68.

[107] J.E. Shelby, Temperature dependence of He diffusion in Vitreous SiO_2, J. Am. Ceram. Soc. 54 (1972) 125-132.

[108] W.G. Perkins, D.R. Begeal, Diffusion and permeation of He, Ne, Ar, Kr, and D_2 through silicon oxide thin films, J. Chem. Phys. 54 (1971) 1683-1693.

[109] R.M. Barrer, D.E.W. Vaughan, Solution and Diffusion of Helium and Neon in Tridymite and Cristobalite, Trans. Faraday Soc. 63 (1967) 2275-2285.

[110] R.W. Lee, R.C. Frank, D.E. Swets, Diffusion of hydrogen and deuterium in fused quartz, J. Chem. Phys. 36 (1962) 1062-1072.

[111] R.W. Lee, Diffusion of hydrogen in natural and synthetic fused quartz, J. Chem. Phys. 38 (1963) 448-458.

[112] R.M. Barrer, D.E.W. Vaughan, Solution and diffusion of helium and neon in tridymite and cristobalite, Trans. Faraday Soc. 63 (1967) 2275-2290.

[113] T. Okubo, H. Inoue, Analysis of surface diffusion of adsorptive gases

through porous glass by a square-pulse nethod, Int. Chem. Eng. 25 (1989) 539-546.

[114] M. Kanezashi, T. Sasaki, H. Tawarayama, H. Nagasawa, T. Yoshioka, K. Ito, T. Tsuru, Experimental and theoretical study on small gas permeation properties through amorphous silica membranes fabricated at different temperatures, J. Phys. Chem. 118 (2014) 20323-20331.

[115] H. Verweij, Y.S. Lin, J. Dong, Microporous silica and zeolite membranes for hydrogen separation, MRS Bull. 31 (2006) 756-764.

[116] M. Amanipour, E.G. Babakhani, J. Towfighi, A. Zamaniyan, Evaluation of a tubular nano-composite ceramic membrane for hydrogen separation in membrane steam reforming reaction, RSC Adv. 6 (2016) 84276-84283.

[117] P. Hacarlioglu, Y. Gu, S.T. Oyama, Studies of the methane steam reforming reaction at high pressure in a ceramic membrane reactor, J. Nat. Gas Chem. 15 (2006) 73-81.

[118] R. W. Baker, Membrane Technology and Applications, 3rd Ed., Wiley, New York, **2012**.

[119] A. Basile, Handbook of Membrane Reactors, 1st Ed., Woodhead Publishing, Elsevier, Amsterdam, **2013**.

[120] A. Basile, F. Gallucci, Membranes for membrane reactors: preparation, optimization and selection, Wiley, New York, **2011**.

[121] S. T. Oyama, Susan M. Stagg-Williams, Eds., Inorganic, Polymeric, and Composite Membranes: Structure-Function and Other Correlations, Elsevier, Amsterdam, **2011**.

[122] J. A. Dalmon, Catalytic membrane reactors, in Handbook of Heterogeneous Catalysis, G. Ertl, H. Knözinger, J. Weitkamp (Eds.), VCH Publishers, Weinheim, 1997, Chapter 9.3

[123] F. Gallucci, E. Fernandez, P. Corengia, M. van Sint Annaland, Recent advances on membranes and membrane reactors for hydrogen production, Chem Eng. Sci. 92 (2013) 40–66.

[124] L. Meng, T. Tsuru, Hydrogen production from energy carriers by silica-based catalytic membrane reactors, Catal.Today 268 (2016) 3–11.

[125] T. T. Tsotsis, A. M. Champagnie, R. G. Minet, P. K. T. Liu, Catalytic Membrane Reactors, pp. 471-551, in Chp. 12 of Computer Aided Design of Catalysts (Becker and Pereira, Eds.), Dekker, New York, **1993**.

[126] H. W. A. El Hawa, S. N. Paglien, C. C. Morris, A. Harale, J. D. Way, Application of a Pd-Ru composite membrane to hydrogen production in a high temperature membrane reactor, Sep. Purif. Technol. 147 (2015) 388-397.

[127] M. D. Dolan, S. S. Hla, L.D. Morpeth, Design and operational considerations for a catalytic membrane reactor incorporating a vanadium-based membrane, Sep. Purif. Technol. 147 (2015) 398-405.

[128] D. Liuzzi, F. J. Pérez-Alonso, J. L. G. Fierro, S. Rojas, F. L. van Wijk, I. Roghair, M. van Sint Annaland, E. Fernandez, J. L. Viviente, D.A.P. Tanaka, Catalytic membrane reactor for the production of biofuels, Catal. Today 268 (2016) 37-45.

[129] P. Kolsch, M. Noack, R. Schafer, G. Georgi, R. Omorjan, J. Caro, Development of a membrane reactor for the partial oxidation of hydrocarbons: Direct oxidation of propane to acrolein, J. Membr. Sci. 198 (2002) 119-128.

[130] B. Meng, H. Zhang, J. Qin, X. Tan, R. Ran S. Liu, The catalytic effects of $La_{0.3}Sr_{0.7}Fe_{0.7}Cu_{0.2}Mo_{0.1}O_3$ perovskite and its hollow fibre membrane for air separation and methane conversion reactions, Sep. Purif. Technol. 147 (2015) 406-413.

[131] E. Shelepova, A. Vedyagin, V. Sadykov, N. Mezentseva, Y. Federova, O. Smorygo, O. Klenov, I. Mishakov, Theoretical and experimental study of methane partial oxidation to syngas in catalytic membrane reactor with asymmetric oxygen-permeable membrane, Catal. Today 268 (2016) 103-110.

[132] S.T. Oyama, X. Zhang, J. Lu, Y. Gu, T. Fujitani, Epoxidation of propylene with H_2 and O_2 in the explosive regime in a packed-bed catalytic membrane reactor, J. Catal. 257 (2008) 1-4.

[133] E. E. Iojoiu, S. Miachon, J-A. Dalmon, Progress in performance and stability of a contactor-type catalytic membrane reactor for wet air oxidation, Top. Catal. 33 (2005) 135-139.

[134] J. C. S. Wu, P. K. T. Liu, Mathematical analysis on catalytic dehydrogenation of

ethylbenzene using ceramic membranes, Ind. Eng. Chem. Res. 31 (1992) 322-327.

[135] E. Gobina, K. Hou, R. Hughes, Mathematical analysis of ethylbenzene dehydrogenation: Comparison of microporous and dense membrane systems, J. Membr. Sci. 105 (1995) 163-176.

[136] J. Shu, B. P. A. Grandjean, S. Kaliaguine, Methane steam reforming in asymmetric Pd and Pd/Ag porous SS membrane reactors, Appl. Catal. A, 119 (1994) 305-325.

[137] J. Tong, Y. Matsumura, H. Suda, K. Haraya, Experimental study of steam reforming of methane in a thin (6µm) Pd-based membrane reactor, Ind. Eng. Chem. Res. 44 (2005) 1454-1465.

[138] F. Gallucci, L. Paturzo, A. Fama, A. Basile, Experimental study of the methane steam reforming reaction in a dense Pd/Ag membrane reactor, Ind. Eng. Chem. Res. 43 (2004) 928-933.

[139] T. Tsuru, K. Yamaguchi, T. Yoshioka, M. Asaeda. Methane steam reforming by microporous catalytic membrane reactors, AIChE J. 50 (2004) 2794-2805.

[140] T. Tsuru, T. Tsuge, S. Kubota, K. Yoshida, T. Yoshioka, M. Asaeda, Catalytic membrane reaction for methane steam refoming using porous silica membranes, Sep. Sci. Technol. 36 (2001) 3721-3736.

[141] S. Sumrunronnasak, S. Tantayanon, S. Kiatgamolchai, T. Sukonket, Improved hydrogen production from dry reforming reaction using a catalytic packed-bed membrane reactor with Ni-based catalyst and dense PdAgCu alloy membrane, Int. J. Hydr. Energy, 41 (2016) 2621-2630.

[142] J.S. Oklany, K. Hou, R. Hughes, A simulative comparison of dense and microporous membrane reactors for the steam reforming of methane, Appl. Catal. A 170 (1998) 13-22.

[143] M. Abdollahi, J. Yu, P. K. T. Liu, R. Ciora, M. Sahimi, T. T. Tsotsis, Ultra-pure hydrogen production from reformate mixtures using a palladium memebrane reactor system, J. Membr. Sci. 390-391 (2012) 32-42.

[144] K. Akamatsu, Y. Ohta, T. Sugawara, N. Kanno, K. Tonokura, T. Hattori, S. Nakao, Stable high-purity hydrogen production by dehydrogenation of cyclohexane using a membrane

reactor with neither carrier gas nor sweep gas, J. Membr. Sci. 330 (2009) 1-4.

[145] J. N. Armor, Applications of catalytic inorganic membrane reactors to refinery products, J. Membr. Sci. 147 (1998) 217-233.

[146] G. Cacciola, Y. I. Aristov, G. Restuccia, V. N. Parmon, Influence of hydrogen-permeable membrane upon the efficiency of the high temperature chemical heat pumps based on cyclohexane dehydrogenation-benzene hydrogenation reactions, Int. J. Hydrogen Energy, 18 (1993) 673-680.

[147] Lange's Handbook of Chemistry, 10th ed., McGraw Hill, New York, 1967, p. 1524.

[148] H. F. Rase, Handbook of commercial catalysts: heterogeneous catalyst, New York: CRC Press, 2000, p. 405.

[149] M. Mihal, R. Vereš, J. Markoš, Investigation of 2-phenlyethanol production in fed-batch hybrid bioreactor: Membrane extraction and microfiltration. Sep. Purif. Technol. 95 (2012) 126-135.

[150] H.A. Al-Megren, T. Poerio, A. Brunetti, G. Barbieri, E. Drioli, B.S.A. Al-Hedaib, A.S.N. Al-Hamdan, M.C. Al-Kinany, Liquid phase benzene hydroxylation to phenol using semi-batch and continuous membrane reactors, Sep. Purif. Technol. 107 (2013) 195-203.

[151] J.K.Kujawski, W.M. Kujawski, H. Sondej, K. Jarzynka, A. Kujawska, M.Bryjak, E. Rynkowska, K. Knozowska, J. Kujawa, Dewatering of 2,2,3,3-tetrafluoropropan-1-ol by hydrophilic pervaporation with poly(vinyl alcohol) based Pervap(TM) membranes, Sep. Purif. Technol. 174 (2017) 520-528.

[152] C.S.M. Perreira, V.M.T.M. Silva, S.P. Pinho, A.E. Rodrigues, Batch and continuous studies for ethyl lactate synthesis in a pervaporation membrane reactor, J. Membr. Sci. 361 (2010) 43-55.

[153] D. Lee, L. Zhang, S. T. Oyama, S. Niu, R. F. Saraf, Synthesis, characterization and gas permeation properties of a hydrogen permeable silica membrane supported on porous alumina, J. Membr. Sci. 231 (2004) 117-126.

[154] Y. Gu, S.T. Oyama, Ultrathin hydrogen-selective silica membranes deposited on alumina-graded structures prepared from size-controlled boehmite sols, J. Membr. Sci. 306

(2007) 216-227.

[155] D. Lee, P. Hacarlioglu, S.T. Oyama, The effect of pressure in membrane reactors: trade-off in permeability and equilibrium conversion in the catalytic reforming of CH_4 with CO_2 at high pressure, Top. Catal. 29 (2004) 45-57.

[156] G.K. Nitin, S. D. Dawande, RTD Studies in Plug Flow Reactor and its Simulation with Comparing Non Ideal Reactors, Res. J. Recent Sci. 1 (2012) 42-48.

[157] H. Liu, C.M. Silva, E.A. Macedo, Unified approach to the self-diffusion coefficients of dense fluids over wide ranges of temperature and pressure—hard-sphere, square-well, Lennard–Jones and real substances, Chem. Eng. Sci. 53 (1998) 2403-2422.

[158] Y. Gu, P. Hacarlioglu, S. T. Oyama, Hydrothermally stable silica-alumina composite membranes for hydrogen separation, J. Membr. Sci. 310 (2008) 28-37.

[159] S. T. Oyama, P. Hacarlioglu, The boundary between simple and complex descriptions of membrane reactors: The transition between 1-D and 2-D analysis, J. Membr. Sci. 337 (2009) 188-199.

[160] H. Lim, Y.F. Gu, S.T. Oyama, Studies of the effect of pressure and hydrogen permeance on the ethanol steam reforming reaction with palladium- and silica-based membranes, J. Membr. Sci. 396 (2012) 119-127.

[161] M. Kanezashi, T. Sasaki, H. Tawarayama, T. Yoshioka, T. Tsuru, Hydrogen permeation properties and hydrothermal stability of sol-gel-derived amorphous silica membranes fabricated at high temperatures, J. Am. Ceram. Soc. 96 (2013) 2950-2957.